Corrosion Behaviour of Materials in High-Temperature Geothermal Environments

Andri Ísak Þórhallsson

Faculty of Industrial Engineering, Mechanical Engineering and Computer Science
University of Iceland
2022

Corrosion Behaviour of Materials in High-Temperature Geothermal Environments

Andri Ísak Þórhallsson

Dissertation submitted in partial fulfilment of a
Philosophiae Doctor degree in Mechanical Engineering

PhD Committee
Dr. Sigrún Nanna Karlsdóttir
Dr. Andri Stefánsson
Dr. Christiaan Petrus Richter

Opponents
Dr. Richard Barker, Associate Professor, University of Leeds
Dr. Marc Singer, Associate Professor, University of Ohio

Faculty of Industrial Engineering, Mechanical Engineering and Computer Science
School of Engineering and Natural Sciences
University of Iceland
Reykjavik, May 2022

Corrosion Behaviour of Materials in High-Temperature Geothermal Environments
Dissertation submitted in partial fulfilment of a *Philosophiae Doctor* degree in Mechanical Engineering

Faculty of Industrial Engineering, Mechanical Engineering and Computer Science
School of Engineering and Natural Sciences
University of Iceland
Tæknigarður – Dunhagi 5
107 Reykjavik
Iceland

Telephone: +354 525 4700

Bibliographic information:
Andri Ísak Þórhallsson, 2022, *Corrosion Behaviour of Materials in Simulated High-Temperature Geothermal Environments*, PhD dissertation, Faculty of Industrial Engineering, Mechanical Engineering and Computer Science, University of Iceland.

Author ORCID: https://orcid.org/0000-0003-1632-6737

Printing: Háskólaprent
Reykjavik, Iceland, May 2022

Abstract

High enthalpy geothermal fluid utilization has a potential for growth for green and sustainable energy production. Geothermal energy production is often limited by the corrosive nature of the geofluids utilized. For successful, safe and economic operation, several technological challenges have to be overcome including the appropriate selection of material(s) for casing, pipelines and other equipment. This dissertation reports the results of a corrosion behaviour study for carbon steel and several corrosion-resistant alloys tested in contact with synthetic geothermal fluids at high temperatures. Corrosion tests were carried out using superheated steam (T = 350 °C and P = 10 barG) containing H_2S, CO_2 and HCl and the materials tested were carbon steel, stainless steel, nickel-based alloys, titanium alloys, high-entropy alloys. Some of the materials were further tested after silica (SiO_2) had been deposited on the surfaces, and under boiling and condensing conditions at lower temperatures. In superheated fluid, carbon steel and Cu added high entropy alloys (HEAs) were prone to corrosion damage but negligible damages were observed in other corrosion-resistant alloys. The carbon steel was prone to more severe corrosion damage in the boiling and condensing conditions in comparison with the superheated test fluid, hence, the corrosion behaviour of carbon steel can be associated with the physical condition and temperature of the corrosive fluid. The extent of corrosion damage of Cu added high-entropy alloys (HEAs) in the superheated fluid is associated with increased Cu content and Cu-rich intermetallics. The corrosion rates of various materials were assessed by the mass loss method (MLM) and were less than 0.1 mm/year in all cases. Microstructural analysis was done via scanning electron microscope (SEM), X-ray energy dispersive spectroscopy (XEDS) and solid and powder X-ray diffraction (XRD) analysis. From the results, it can be concluded that the corrosion-resistant alloys are immune to corrosion damage in high-enthalpy superheated geothermal fluid containing H_2S, CO_2 and HCl and should be selected in preference to carbon steels and Cu added HEAs in such environments.

Útdráttur

Jarðhitaorkunýtni vökva með háa entalpíu (vermi) er ein af mörgum aðferðum sem hægt er að nota til að stuðla að umhverfisvænni og sjálfbærri orkunotkun í framtíðinni. Til að gera þessa tegund orkunýtni arðbæra þarf hins vegar að yfirvinna nokkrar tæknilegar hindranir þ.m.t. rétt val á hráefnum sem hefur gott tæringarþol í jarðhitafóðringar og búnaði fyrir jarðhitaorkuver. Þessi doktorsritgerð fjallar um rannsókn á tæringahegðun svarts stáls og annarra tæringarþolna melma í hermdum jarðhitavökva við há hitastig. Tæringarprófanir á málm- og melmissýnum (svart stál, ryðfrí stál, nikkel melmi og títanium melmi) voru framkvæmdar í yfirhitaðri gufu með H_2S, CO_2 og HCl við 350 °C og 10 börG. Nokkur sýnanna voru einnig prófuð eftir að kísiloxíð (SiO_2) hafði verið útfellt á sýnin. Einnig voru sýni prófuð við suðu og þéttingu á hermdum jarðhitavökva við 10 börG og við lægri hitastig en 350 °C. Svart stál og háentrópíumelmi með kopar (Cu) tærðust greinilega en aðrir tæringarþolnir málmar tærðust ekki. Ennfremur varð tæringarskaði í svörtu stáli meiri við suðu og þéttingu á jarðhitavökvanum en í yfirhituðum vökva sem sýnir að tæringarhegðun stálsins er háð ástandi og hitastigi tæringarvökvans. Tæringarskemmdir á háentrópíumelmum sem innihéldu kopar jókst með meira koparinnihaldi melmisins í tæringarprófunum í yfirhituðum vökva. Auknar tæringarskemmdir er hægt að útskýra með auknum styrk á koparríkum fösum í háentrópiumelminu. Tæringarhraði var metinn með vigtartapi og var lægri en 0,1 mm/ár fyrir öll sýnin sem voru prófuð í yfirhituðum vökva. Uppbygging og myndgreining efnis og tæringarleifa var greind í rafeindasmásjá (SEM) og efnasamsetning þeirra var greind með efnagreiningu í XEDS greini og kristalbygging með röngtgengeislagreiningu (XRD). Niðurstöðurnar sýna að tæringarþolin melmi verða ekki fyrir tæringu í yfirhituðum hermdum jarðhitavökvanum. Þessi melmi ættu því að velja frekar en svart stál eða háentrópíumelmi sem innihalda kopar í jarðhitaumhverfi með yfirhituðum vökva.

Dedication

I dedicate this work to my wife, Ragnheidur Guðmundsdóttir, for the support and time she has given me for this study

Table of Contents

List of Figures

List of Tables

Abbreviations

HEA	High Entropy Alloy
HT	High-Temperature
HTD	High-Temperature Deep
IDDP	Iceland Deep Drilling Project
JA1	Journal Article 1
JA2	Journal Article 2
JA3	Journal Article 3
JA4	Journal Article 4
MLM	Mass Loss Method
RQ	Research Question
RT	Room Temperature
SEM	Scanning Electron Microscope (or Scanning Electron Microscopy)
SSC	Sulphide Stress Cracking
SH	Superhot
XEDS	X-ray Energy Dispersive Spectroscopy (or X-ray Energy Dispersive Microanalysis)
XRD	X-Ray Diffractometer (or X-Ray Diffraction)

Acknowledgements

I want to thank my wife and children, for the patience, time and support you have given me during these years of my PhD study. I hope I can return most of the time somehow with you in future.

I want to give my gratitude to my instructor, Sigrun N. Karlsdottir, for giving me the opportunity to do this study, for the contribution and good support, nice cooperation and patience during this work.

I want to thank the other two members of the PhD committee, Andri Stefansson and Christiaan Petrus Richter for their advice, review and work they have consumed for my work.

Thanks to the funders of this project; the Icelandic Research Fund (RANNÍS) grants No. 163108-051, 163108-052 and 163108-053, Geothermal Research Group (GEORG) and Energy Research Fund (Landsvirkjun) for funding this project.

1 Introduction

The exploitation of geothermal energy from geothermal well fluid discharges for heat and power production is one of the renewable energy alternatives [1,2] that can replace energy production via fossil fuel burning and hence reduce the amount of greenhouse gas (GHG) emission.

Corrosion of geothermal process equipment materials and utilities such as casings, pipes, turbines, valves and other equipment are normally associated with the exploitation of geothermal energy, which can affect the efficiency and cost of geothermal energy production [3,4]. Understanding the corrosion behaviour of materials under variable physical conditions and the chemical composition of the geothermal fluid is, therefore, vital for optimum material selection and to increase the economics and sustainability of the system providing geothermal energy.

Geothermal boreholes in high-temperature geothermal systems are typically drilled to depths of ~2-3 km, discharge fluids with temperatures of ~200-350°C [5]. Drilling into deeper parts of the geothermal system and/or close to the magmatic heat source has been suggested to be able to increase the power production of a single borehole up to 30-50 times. Such high-temperature deep (HTD) geothermal wells would be operated at temperatures >350°C with enthalpy of 2800-3500 kJ/kg [6–8] and discharging superheated or supercritical fluids. In addition, to prevent potential scaling upon depressurization, the boreholes may need to be operated at higher pressures (>100 bar) than conventionally done (typically 5-50 bar). Until today, very few studies of corrosion behaviour of materials have been conducted at such temperatures relevant for HTD geothermal environments, such knowledge is critical for the appropriate selection of material(s) for casing, pipelines and other equipment[6,8,9].

In this dissertation, the corrosion behaviour of carbon steel and corrosion-resistant alloys was studied in contact with synthetic geothermal fluids relevant to the HTD geothermal conditions. The main focus was on the corrosion behaviour in single-phase superheated geothermal fluid environment, but some additional tests were also conducted in contact with two-phase (liquid and vapour) fluids for comparison. In most cases, the set temperature of the corrosion tests was 350°C and the set pressure was 10 barG set for vapour phase conditions. These conditions are comparable to previous work related to in-situ tests conducted in the Iceland Deep Drilling Project well number 1 (IDDP-1) by Karlsdottir et al. [10]. In addition, corrosion tests were conducted at lower temperatures down to 180°C mimicking boiling and condensation of HTD geothermal fluid associated with temperature changes.

The study consists of four journal articles (**JAs**) published in international scientific journals and four conference articles from three international conferences. Each journal article reports the investigation of the corrosion behaviour of carbon steel and corrosion-resistant alloys in contact with synthetic, high-temperature geothermal fluids. The distinction between the topic of the articles involves testing of different materials, testing

samples additionally at two-phase (liquid and vapour) conditions of the simulated geothermal fluid and testing after solid silica deposition on the surfaces of the samples.

The contribution of the dissertation is to provide an understanding of the corrosion behaviour of carbon steel and corrosion-resistant alloys under various conditions expected in superheated and supercritical geothermal systems where H_2S, CO_2 and HCl are among the potential corrosive fluid species. Furthermore, this study will also provide a new approach and design criteria details for superheated and multiphase testing facilities for future corrosion studies in connection with a geothermal environment.

1.1 Related Work

The aim of the Iceland Deep Drilling Project (IDDP) is to extract energy and fluids from hydrothermal systems at supercritical conditions. In Iceland, such boreholes were planned to be drilled to ~3.5 – 5 km depths in three different geothermal fields to reach supercritical fluid with temperatures of ~400-600 °C [6]. Two deep geothermal wells have been drilled [8,9] at the present date in Iceland.

The first deep geothermal well (IDDP-1) drilled in Krafla, Iceland, was terminated at only 2100 m depth [11,12] after drilling into magma [12]. Despite the relatively shallow depth, the well discharged superheated geothermal fluid eventually with wellhead temperatures of ~440°C. The geothermal fluid contained corrosive species such as H_2S, CO_2, HCl, HF and H_2. In addition to the corrosive substances, the superheated geothermal fluid contained dissolved silica [13] which generally is considered to have a protective role when it precipitates from liquid geothermal fluid and scales on material surfaces [14].

In-situ corrosion tests connected to the wellhead of the IDDP-1 well in Krafla were performed, at 360 °C and 12 bars. The test results showed that all samples tested, including the carbon steels; S235JR, K02100, K55, TN95, austenitic stainless steels; S30403, S31603, S31254, Ni-based alloys; N06255 and N06625 and titanium alloys; R50400 and R52400 had very low corrosion rates (< 0.01 mm/year) but all the samples were prone to localized corrosion damages, i.e. cracking, pitting or both [10]. Furthermore, all samples tested had silica scaling covering the surfaces, which might have affected the corrosion behaviour of the samples tested. It was concluded that silica scaling on the test sample surface had likely provided a protective effect resulting in a low corrosion rate but might have also promoted some localized corrosion damage in the test samples due to under deposit corrosion. As a result, questions arose about whether the same corrosion behaviour would result if the carbon steels or the corrosion-resistant alloys would be in a similar dry superheated geothermal fluid but without any silica scaling. Due to several corrosive species present in the geothermal fluid of IDDP-1, it was not evident which chemical species or environmental factors were the sources of the localized corrosion damages observed in all the carbon steel and corrosion-resistant alloys tested. Furthermore, it was not evident from this corrosion test what corrosive species were promoting the localized corrosion damage in all the samples [10]. The well had to be eventually closed due to corrosion damages to the wellhead and the casing and further testing was therefore not done.

In previous work by Jonsson et al. [15], a first attempt to conduct laboratory corrosion tests in synthetic superheated aqueous geothermal fluid containing H_2S, CO_2 and HCl was

performed. A flow-through autoclave setup was used at temperatures of 350 °C and pressures of 10 barG to simulate HTD geothermal conditions and to study the corrosion behaviour of carbon steel, super austenitic stainless steel and two nickel-based alloys in the environment. Cracking was observed in the super austenitic UNS S31254 and the nickel-based alloy UNS N06625 but all the samples were tested without external stresses. The cracking in the UNS N031254 was intergranular indicative of intergranular cracking (IGC) behaviour but the cracking behaviour in the UNS N06625 was not evident. The corrosive environment and residual stresses from machining of the samples were potentially enough for inducing intergranular stress corrosion cracking (IGSCC), similar cracking was found in on-site IDDP-1 heat exchanger corrosion tests for austenitic UNS S31254 pipes that experienced fluctuation in pressure and clogging due to silica in the equipment [16]. From the study by Jonsson [15], it was concluded that mixed-phase (wet and dry) conditions in the test volume could have induced localized corrosion damage behaviour. An extremely high corrosion rate was observed in the carbon steel and the other nickel-based alloy was prone to general corrosion but not localized corrosion damage. These results were not entirely in agreement with the previous in-situ tests in IDDP-1 [10]. The cause may have been the plugging of deposits at the inlet and outlet of the autoclave resulting in pressure increase and fluid condensation. The vertical setup of the reactor might also have contributed to the backflow of condensed fluid into the reactor. Such would have resulted in two-phase fluids (liquid and vapour) associated with the corrosion tests affecting the results of the corrosion tests. The authors suggested improvement of the test design and setup for future tests that included, for example, replacement of back-pressure regulator that could be operated even upon solid deposition, longer autoclave systems with pre-heating section, and alteration of the position of various parts including horizontal setup to prevent condensed fluid backflow.

Recent work by Thorbjornsson et al. [17] of corrosion studies of corrosion-resistant alloys in a geothermal fluid from the geothermal well RN-35 at Reykjanes in Iceland, where the geothermal fluid was heated from 210 °C from the well up to superheated conditions at 450 °C at 20 barG in a flow-through reactor, reported that no corrosion-resistant alloys tested (including UNS N06625, UNS S31254) were prone to localized corrosion damage and all the samples had insignificant corrosion rate (< 0.01 mm/year) except the medium carbon steel tested without cladding (0.11 mm/year). The geothermal fluid from the well RN-35 contained H_2S, CO_2, H_2 and some other corrosive species but did not include HCl or HF. Another study by Thorbjornsson et al. [18] from retrieved casing material at the wellhead showed high-temperature hydrogen attack and cracking behaviour of medium carbon steel due to decarburization and methane formation at the grain boundaries.

Another study by Yanagisawa et al. [19] to model the corrosion rates of materials in the IDDP-1 geothermal fluid at Krafla at 25–500 °C with a maximum pressure of 60 MPa showed that the highest corrosion rates were obtained at subcritical temperatures of 300–350 °C. This conclusion was assessed by the pH dependence on temperature and pressure, Cr equivalent and empirical corrosion rate formulas by Kurata et al. [20] but the numerical corrosion rate values predicted for carbon steel were somewhat higher than the results from the in-situ test in IDDP-1 [10] and simulated laboratory test [15] in this dissertation. The results of Yanagisawa et al. imply that adequate corrosion rate models for the superheated geothermal environment are not present with the current knowledge and more information (CR, corrosion behaviour) is needed on the corrosion behaviour of materials in these superhot conditions.

1.2 Motivation of Study

Based on the outcome of previous corrosion studies, it is clear that much more work is needed to understand and map out the corrosion behaviour of various materials in HTD geothermal environments. For example, the cause of localized corrosion damage observed in previous in-situ studies in HTD geothermal fluid and the effects of silica scaling on the corrosion behaviours are uncertain. Moreover, a limited number of corrosion studies have been conducted related to the corrosion behaviour of carbon steel or corrosion-resistant alloys commonly used within the geothermal industry both in a single-phase superheated or supercritical fluid or associated with two-phase (liquid and vapour) fluids. Such comparison is very important as multiphase geothermal fluid conditions can be expected during different operation phases of the well such as warm-up, shut-in and discharge for example.

The results of this study were intended to increase our knowledge of the corrosion behaviour of carbon steel and CRAs in HTD geothermal environments which are needed for material selection and design of future HTD geothermal wells. Furthermore, experimental data on corrosion rates can aid in the construction of future corrosion rate models for corrosion in a superheated geothermal fluid.

1.3 Research Questions and Structure of Dissertation

In this PhD research project, the corrosion behaviour of carbon steel and corrosion-resistant alloys in simulated, superhot and mixed-phase, geothermal environments is studied. From the above discussions and previous work and background, the following research questions (**RQs**) were defined in the project and answered based on the findings of the PhD research:

Research Question 1 (RQ1):
Does superheated fluid, where the bulk is H_2O that contains H_2S, CO_2 and HCl, promote localized corrosion damage in carbon steel or corrosion-resistant alloys tested in this study?

Research question 2 (RQ2):
Does commonly observed scaling (i.e. amorphous silica) promote localized corrosion damage on material surfaces in superheated steam of geothermal origin/nature?

Research Question 3 (RQ3):
Is there a significant difference in material corrosion behaviour depending on the phase properties of the geothermal fluid, i.e. the fluid is superheated or in a liquid state?

In research question 1 (**RQ1**), all the materials tested i.e. carbon steel and corrosion-resistant alloys were the subject of the investigation as localized corrosion damage was observed in a previous study by Karlsdottir et al. [10]. In research question 2 (**RQ2**) however, only corrosion-resistant alloys (nickel-based alloys) are subject to the investigation because the carbon steel was prone to localized corrosion damage in the simulated HT environment when tested without silica scaling. In research question 3

(**RQ3**), both carbon steel and corrosion resistant alloy (titanium alloy) were the subject of the investigation.

Journal article 1 (**JA1;** *Corrosion testing of materials in the simulated superheated geothermal environment*) covers most of the materials tested in superhot fluid and contributes to **RQ1**. Journal article 2 (**JA2;** *Effect of alloying ratios and Cu-addition on corrosion behaviour of CoCrFeNiMo high-entropy alloys in superheated steam containing CO_2, H_2S and HCl*) is a continuation of the research outlined in JA1 but with fabricated HEAs in a laboratory tested (candidate material) in the superhot fluid. Journal article 3 (**JA3;** *Corrosion Behaviour of Titanium Alloy and Carbon Steel in a High-Temperature, Single and Mixed-Phase, Simulated Geothermal Environment Containing H_2S, CO_2 and HCl*) covers the testing of carbon steel and titanium alloy in superheated and two-phase (boiling and condensed) fluid conditions and contributes to **RQ1** and **RQ3**. Finally, journal article 4 (**JA4;** *Silica scaling and boiling effect on corrosion behaviour of nickel-based alloys associated with superheated hydrothermal fluids containing HCl, H_2S and CO_2*) covers testing of nickel-based alloys covered with a scale from geothermal brine tested in superhot fluid and contributes to **RQ1** and **RQ2.** The RQs and their link to the journal articles (**JA1** to **JA4)** can be seen in Figure 1.

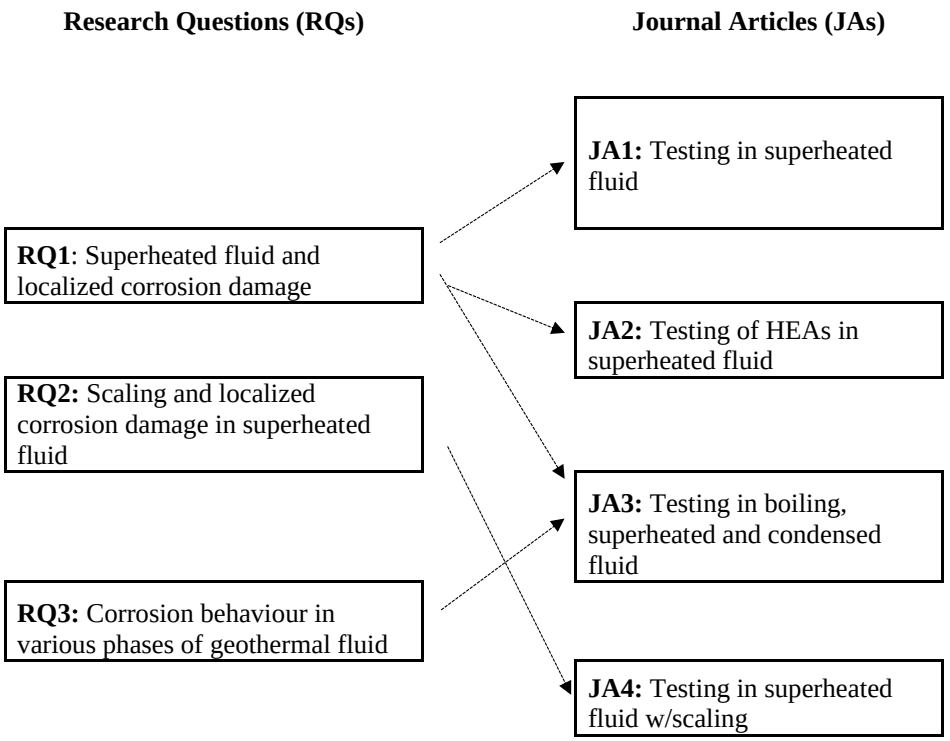

Figure 1 Research questions (RQs) and link to journal articles (JAs)

The dissertation is divided into five chapters. The first chapter is the introduction of the subject, the second chapter is the theoretical background where geothermal and common corrosion phenomenons in the geothermal environment are explained. The third chapter presents the methods for running the tests and analysing the results. The fourth chapter summarized the results of individual articles, both journal and conference articles contributing to this PhD research work. The final chapter, the fifth, represents the conclusion, discussions and recommended future work followed by references and journal articles as published

2 Background

This chapter outlines some of the most common corrosive species and corrosion forms of materials in the geothermal environment experienced by the geothermal industry. In this study, most of the corrosion tests were conducted in a single phase, superheated fluid but some tests were also performed under liquid conditions, thus in this chapter, the difference between "dry" and "wet" corrosion is explained. The distinction in the corrosion behaviour of materials in dry superhot gas and in wet liquid, i.e. the theoretical distinction between wet corrosion (in the liquid fluid) and dry corrosion (gaseous or vapour fluid) and the most common corrosive species and corrosion forms in a geothermal environment is presented and discussed.

2.1 Corrosion in Geothermal Fluid

Corrosive species and corrosion forms in geothermal environments have been summarized by Nogara et al. [21,22]. In this study, many of the corrosion forms explained in this chapter were not experienced, but for theoretical background, the main corrosive species and corrosion forms experienced by materials in geothermal environments are introduced.

Corrosive Species in Geothermal Fluid

A geothermal fluid has H_2O as the bulk phase but commonly gases or corrosive chemical species are H_2S, CO_2, H_2, HCl, chloride and more [3,23].

Hydrogen sulphide (H_2S) can react with the material and form sulphide corrosion products but can also provoke more severe corrosion damage by hydrogen damage such as sulphide stress cracking (SSC) for low alloy steels [24] and martensitic stainless steels with high hardness in sour environments [25]. Materials can also be prone to hydrogen cracking, blistering, hydrogen embrittlement and hydrogen attack (decarburization) due to the effect of hydrogen. Hydrogen sulphide can also play a major role in the effect of CO_2 corrosion when the two species are present in the environment [26].

Corrosion due to CO_2 can be explained by the increased acidity (lower pH) effect of dissolved CO_2 in an aqueous fluid. Increased acidity promotes the attack of H^+ on the corrosive material but also prevents the formation of a passive layer, such as iron hydroxides in acidic fluid [27]. At high temperatures, gaseous CO_2 can react directly with metals and form corrosion and passive layer products [27,28].

Hydrogen chloride is a strong oxidizer where H^+ reacts with the material promoting anodic dissolution in an aqueous medium and the chloride ion in the solution can prevent passivation of the passive layer forming materials, promoting localized corrosion damage in passive materials. Hydrogen chloride can also provide atomic hydrogen in the cathodic reduction of H^+. Limited literature was found on corrosion of materials in a gaseous HCl environment without O_2 but a study by Krumm et al. shows that the effect of gaseous HCl induced corrosion is more profound in absence of O_2 [29].

Corrosion due to hydrogen (H_2) is related to the adsorption of hydrogen molecules at the surface of the material and the migration of atomic hydrogen into the lattice of the material, promoting hydrogen damage as described above.

Uniform Corrosion

Uniform corrosion is where the uniform dissolution of material is experienced due to a uniform attack of the corrosive species for a prolonged time. The measured corrosion rate (CR) of the material tested in mm/year was calculated via the mass loss method (MLM) and according to standard ASTM G1 [30] :

$$CR = \frac{K \cdot W}{A \cdot t \cdot \rho} \quad (1)$$

Where $K = 8.76 \cdot 10^4$, W is the mass loss in grams of the tested material with a ±0.00005 gram precision, A is the exposed surface area in cm^2 of a tested sample, t is the exposure time in hours, and ρ is the material density in g/cm^3.

Sulphide Stress Cracking (SSC)

Hydrogen sulphide is an aggressive hydrogen supplier because it provides hydrogen from its molecule to the surface and can form sulphide "poison" in the material which retards the formation of molecular hydrogen [31], enhancing the effect of atomic hydrogen formed. Dissolved hydrogen sulphide (H_2S) can attack carbon and low alloy steel alloys, forming iron sulphide and releasing hydrogen molecules which can promote the diffusion of atomic hydrogen into the steel lattice and induce hydrogen damage by the reactions [32]:

$$Fe_{(s)} \rightarrow Fe^{2+}_{(aq)} + 2e^- \quad (2)$$

$$H_2S_{(aq)} + 2e^- \rightarrow S^{2-}_{(aq)} + H_{2(g)} \quad (3)$$

Giving the overall reaction

$$Fe_{(s)} + H_2S_{(aq)} \rightarrow FeS_{(s)} + H_{2(g)} \quad (4)$$

The hydrogen can then be adsorbed to the material surface and form atomic hydrogen

$$H_{2(ad)} \rightarrow 2H_{(ad)} \quad (5)$$

The iron sulphide acts also as a poison and prevents of the formation of atomic hydrogen back to molecular hydrogen [33]. The atomic hydrogen can diffuse into the material lattice, making the material more brittle and susceptible to SSC. If the susceptible material is under applied or residual tensile stresses in an H_2S environment and with other favourable environmental factors, a brittle fracture, SSC can be promoted in the material [31,34].

Other Hydrogen Damage

Hydrogen cracking is localized corrosion damage normally classified into three categories, hydrogen-induced cracking (HIC), sulphide stress cracking (SSC) and stress oriented hydrogen induced cracking (SOHIC) which is a combination of both HIC and SSC [35]. The crack mechanism depends on the environment but also the microstructure of the material and stresses exerting on/in the material [36–41]. Hydrogen embrittlement arises from atomic hydrogen diffusion into the material lattice and is normally more favoured for hardened materials at low temperatures [42].

Hydrogen can be provided with H_2S but also with acidic environments and the cathodic reaction of water according to:

$$2H^+_{(aq)} + 2e^- \rightarrow H_{2(g)} \quad (6)$$

$$2H_2O_{(l)} + 2e^- \rightarrow H_{2(g)} + 2OH^-_{(aq)} \quad (7)$$

Atomic hydrogen can recombine and form hydrogen molecules which can increase the pressure inside the material and form hydrogen blisters which can start a cracking or rupture due to excess hydrogen gas pressure [31]. The supply of hydrogen with other hydrogen sources can also promote hydrogen embrittlement as in SSC. At elevated temperatures, the hydrogen can react with carbon precipitates at the grain boundaries and dislocations and can form methane gas ($CH_{4(g)}$) or decarburize which can produce a sudden rupture or crack mechanism due to increased gas pressure inside the material [31,39]. The formation of methane can be reduced by precipitating titanium, zirconium or vanadium carbides in the grain boundaries of the material [31]. Titanium and other alloys can also form brittle hydrides when reacting with hydrogen normally at temperatures above 250 °C [31].

Formation of Sulphide Corrosion Product with an Oxide Layer

Hydrogen sulphide, in non-oxygen (O_2) containing fluid, has also been reported to react with fast forming magnetite (F_3O_4) to form iron sulphide (FeS) according to Gao et al. [43] by the following chemical reaction:

$$Fe_3O_{4(s)} + 3H_2S_{(aq)} + 2H^+_{(aq)} + 2e^- \rightarrow 3FeS_{(s)} + 4H_2O_{(l)} \quad (8)$$

The formation of the external sulphide layer on the internal oxide layer is well known in the geothermal industry [44,45].

Corrosion due to CO_2

Carbon dioxide (CO_2) when dissolved in aqueous fluid, can form an acidic environment which can promote corrosion of materials in a geothermal environment [27,46]:

$$H_2CO_{3(aq)} \leftrightarrow H^+_{(aq)} + HCO_3^-{}_{(aq)} \quad (9)$$

$$HCO_3^-{}_{(aq)} \leftrightarrow H^+_{(aq)} + CO_3^{2-}{}_{(aq)} \quad (10)$$

With the anodic dissolution of iron for instance as mentioned in (2) and the corrosion product of iron carbonate:

$$Fe^{2+}_{(aq)} + CO_3^{2-}_{(aq)} \leftrightarrow FeCO_{3(s)} \quad (11)$$

A study by Jingen et al. has revealed retarding effect of H_2S on CO_2 corrosion of carbon steel [26] and other studies have revealed both retarding and promoting effects, depending on the temperature of the environment [47]. It has also been concluded that the CO_2 corrosion of steel is strongly pH-dependent and accelerates at lower pH [48]. The presence of CO_2 increases the rate of hydrogen evolution which increases the overall dissolution rate of iron in brine or aqueous solutions. Furthermore, at pH>4, CO_2 can lead to much higher corrosion rates, than corrosion in strong acids, at the same pH. This phenomenon is explained by the presence of H_2CO_3 in CO_2 solutions, increasing the hydrogen evolution step in the iron anodic dissolution mechanism and due to the slow mass transfer of H^+ from strong acids towards the iron surface at pH>4 which limits the hydrogen evolution step and hence the overall iron dissolution rate [49,50].

Stress Corrosion Cracking

Stress corrosion cracking (SCC) is brittle localized damage that occurs when constant tensile stress is applied or when internal stresses are present in susceptible material, commonly passive materials in high-temperature chloride-rich environments [51]. Austenitic stainless steels have been reported to be prone to SCC in geothermal environments, with and without, chloride in the geothermal fluid [52–55]. Testing in a dry superhot geothermal fluid under stress has shown SCC behaviour of austenitic stainless steels but not in carbon steels or other corrosion-resistant alloys tested [10].

Pitting and Crevice Corrosion

Pitting and crevice corrosion are both localized corrosion damage forms. Pitting corrosion can be experienced in passive metal alloys where the localized corrosion rate is relatively rapid and anions, such as chloride (Cl^-), prevents the formation of a passive layer at localized sites after the breakage of the passive layer in the corrosive environment. Crevice corrosion can be experienced in passive metal alloys and materials that do not passivate and is experienced where the crevice is at lower reduction potentials than the external surface of the crevice. In the geothermal industry, pitting and crevice corrosion has been experienced for corrosion-resistant alloys but also in non-passive such as carbon and low alloyed steels [56–61].

De-alloying

De-alloying is when one or more of the alloying elements in the material is more susceptible to corrosion than the rest of the alloy [62]. A limited number of de-alloying incidents have though been reported in the geothermal environment.

Intergranular Corrosion

Intergranular corrosion is localized corrosion damage where selective corrosion at the grain boundaries of the material occurs. The grain boundaries can have different composition and reduction potentials than the rest of the materials and hence, a driving force for internally driven corrosion or corrosion due to the environment can occur. Intergranular corrosion can be experienced in some austenitic stainless steels at grain

boundaries where chromium carbide precipitation has occurred due to heat treatment of the material [63].

Fluid Flow Induced Corrosion and Erosion Corrosion

Fluid flow-induced corrosion can be categorized into four types of corrosion; mass transport controlled corrosion where the corrosion mechanism is induced by the increased convective effect of the flowing fluid, phase transport corrosion where the flowing fluid supplies aggressive phases towards the corrosive surface, cavitation corrosion where gas bubbles implode from the flowing fluid on the corrosive surface and finally erosion-corrosion [64]. Erosion corrosion is associated with moving or high-velocity fluid containing solid particles that break or remove the surface film of the material that otherwise acts as a protective film for the material. Erosion corrosion occurs for soft materials in a high-velocity fluid where turbulent flow or changes in flow conditions and patterns occur. Vapour-phase steam carrying water can be very erosive corrosive to steel [65]. As geothermal fluid can travel at high velocity from the geothermal source through the geothermal casing, piping and equipment, erosion-corrosion has been reported in the geothermal industry and simulated tests [66,67].

Galvanic Corrosion and Concentration Cell Corrosion

Galvanic corrosion is localized corrosion damage when two dissimilar metals or materials submerged in the same electrolyte are also electrically connected via direct contact. The metal with the lower reduction potential will corrode due to the potential difference with the other metal (at higher reduction potential) or/and due to the synergic effect of the environment and the other metal [68]. Solid precipitates on a solid surface exposed to electrolytes can also be a subject of galvanic coupling. Pyrrhotite, one iron sulphide form, has also been reported by Esmaeely et al. to have a galvanic effect on an iron surface and induce localized corrosion damage in the iron where H^+ dominates the reduction reaction. Furthermore, galvanic coupling between sulphide layers (cathodic pyrite and anodic pyrrhotite) has also been reported by the same authors [69–71]. In our study, attention was paid to sites where washers and fasteners were connected to the test samples to observe if any galvanic corrosion had occurred in the tests. Concentration cell corrosion occurs where a gradient in concentration of the cathodic species results in a gradient in oxidizing power on the surface that can result in anodic dissolution.

2.2 Wet and Dry Corrosion Mechanism

Wet corrosion occurs in liquid electrolytes when anodic material reacts in its environment due to the oxidative power of some cathodic species. In case of corrosion of metal/metal alloy, the anodic metal/metal alloy loses an electron (or electrons) to the corrosive species or the cathode and the anodic material is then afterwards solvated in the liquid electrolyte where corrosion product is formed on the surface at the anode-cathode interface or dissolved in the fluid. The liquid electrolyte has a high dipole moment and solvation capability that acts as a charge carrier in the corrosion process [72].

For the electrochemical wet corrosion reaction to proceed, electronic charge transfer occurs between the anodic and cathodic material but charge transfer via ion movement occurs also via the electrolyte. Wet corrosion can have many forms and driving mechanisms but the main factors affecting wet corrosion are; the potential difference between the anodic and

cathodic half cells, electrolyte conductivity, surface properties (kinetics) of the electrodes, the concentration of the solvated anodic/cathodic materials, mass transport of cathodic species towards the anodic surface (convection of electrolyte), the relative surface area of anode vs. cathode and more [31]. A schematic of the wet corrosion mechanism is given in Figure 2.

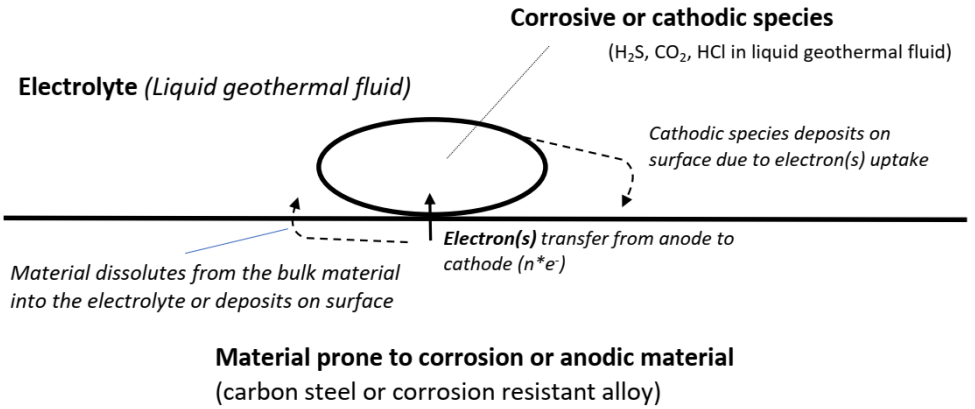

Figure 2 Schematic of wet corrosion mechanism

Dry corrosion is distinct from wet corrosion mainly due to the absence of liquid electrolytes in the corrosion process. The mechanism of dry corrosion is not straightforward and can be the result of many intermediate reactions occurring to the final corrosion product [73]. Dry corrosion can occur at temperatures below 200 °C [74] where the gas is adsorbed on the metal/metal alloy and reacts with the surface if the enthalpy of formation for the corrosion product is negative i.e. the formation of the corrosion product is possible in the environment.

The dry corrosion reaction is dependent on the temperature and partial gas pressure of the corrosive species in the gas phase. If the reaction between the corrosive gas species and the solid metal/metal alloy occurs, a thin surface scale, corrosion film, initially forms. The progress and nature of the corrosion film can progress depend then to some extent on the properties of the film such as melting point, conductivity, lattice structure and defects, ionic nature of the surface scale (charged vacancies) and more. The amount of lattice disorder in the corrosion film can determine the growth rate of the corrosion film. A highly disordered lattice in the corrosion film leads to a high growth rate but a lattice with low defects has a low growth rate. The growth of the corrosion film can be determined by the mass diffusion of metal/metal alloy through the corrosion film towards the surface or determined by the permeation of the corrosive gas species through the corrosion film to the metal/metal alloy and corrosion film interface. As a result, the corrosion film growth can either be dominated by growth on the surface of the corrosion film or by the growth at the corrosion film and the metal/metal alloy interface [75]. The mechanism of the two dominant dry corrosion mechanisms is schematically drawn in Figure 3.

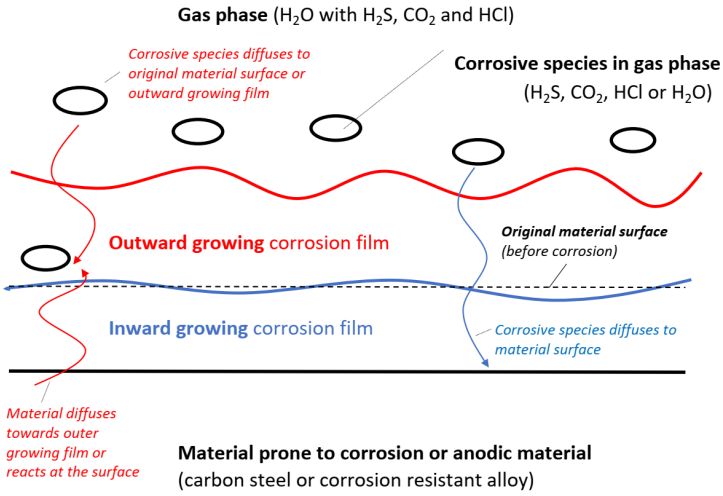

Figure 3 Schematic of the two dominant corrosion mechanisms for growth of corrosion film in dry corrosion

2.3 Conventional and Deep Geothermal Wells

To exploit the geothermal energy from the earth´s crust, geothermal wells are commonly drilled to less than 3 km depth into geothermal systems [76] where the transportation of the high enthalpy geothermal fluid, towards the surface, occurs via open holes or pipes/casing material that has been inserted into the well to maintain its integrity and energy output efficiency. The geothermal fluid is most commonly dominated by H_2O, with other major gases being example CO_2, H_2S and H_2. "Conventional" high-temperature geothermal wells typically discharge two-phase (liquid and vapour) fluids. In such cases, carbon steel casing materials are commonly selected from the American Petroleum Industry (API) standards which are prone to corrosion [3,77,78]. The extent of corrosivity of the geothermal fluid can vary, depending on several factors such as temperature and the fluid composition including pH, the concentration of dissolved gasses and more [79]. The more common high-temperature wells are normally in the temperature range of 240 – 340 °C [6] but in recent years there has been growing attention toward drilling wells at even more depths to provide higher temperature and enthalpy geothermal fluids than the conventional high-temperature wells. These wells onward referred to as high temperature deep geothermal wells, are expected to produce additional energy or an enthalpy output with estimated power production of an order of magnitude higher than from the more conventional high-temperature wells [6]. Depending on the good design and physical condition of the fluid, the fluid velocities of high temperature deep geothermal wells can be expected to be on the scale of 30 -100 m/s [66,80]. Due to high cost and some technical challenges, only a few deep geothermal wells have been drilled to the present date [81]. As a result, few corrosion tests have been conducted in-situ in deep geothermal wells. The lack of availability of corrosion facilities for corrosion studies at temperatures above 250 °C has also limited the number of corrosion studies in simulated high-temperature geothermal environments.

3 Experimental

3.1 Test Materials and Sample Preparation

Carbon steel and low alloyed steel are common casing materials and hence one carbon steel type was selected for this study. The corrosion-resistant alloys tested were austenitic stainless steels, nickel-based alloys, titanium alloys and high entropy alloys are given in Tables 1 to 4 but more detailed descriptions of the characteristics and composition of materials are given in the publication of this study.

Table 1 Summary of main alloying elements in carbon steel and CRAs tested in JA1

Material	UNS no.	Other design.	Nominal composition [% wt]											
			C	Cr	Ni	Mo	N	Cu	Al	Nb	Ti	W	Sn	Fe
Carbon steel	N/A	NS-EN S235JRG2	0.04	0.04	0.02	0.00	0.003	0.040	0.04	0.00	0.00			bal.
Austenitic stainless steel	S31254		0.02[a]	20.0	18.0	6.1	0.2	0.7						bal.
	S31277		0.02[a]	23[a]	28[a]	8[a]	0.4[a]	1.5[a]						bal.
Nickel-based alloy	N06255		0.03[a]	26[a]	52[a]	9[a]		1.2[a]				3[a]		bal.
	N06845		0.05[a]	25[a]	50[a]	7[a]		4[a]				5[a]		bal.
	N06625		0.1[a]	23[a]	58.0[b]	10[a]			0.4[a]	4.15[a,b]	0.4[a]			5.0[a]
Titanium alloy	N/A	Ti-4Al-4Mo-2Sn				5[a]	0.27		5[a]		bal.		2.5[a]	0.2[a]

[a)]Maximum value *[b)]Nb + Ta*

Table 2 Summary of alloying elements in HEA tested in JA2

Material	Nominal composition [% wt]					
	Cr	**Ni**	**Mo**	**Cu**	**Co**	**Fe**
HEA1[a)]	16.2	18.3	29.9		18.3	17.4
HEA 2	19.4	21.9	15.9		22	20.8
HEA 3	13.3	15	42.2		15.1	14.3
HEA 4	14.3	16.1	26.4		27.8	15.4
HEA 5	13.5	15.2	24.9	16.5	15.3	14.5
HEA 6	15.6	16.5	13	22.6	16.6	15.7

[a)]*HEA = "High Entropy Alloy"*

Table 3 Summary of alloying elements in carbon steel and titanium alloy tested in JA3

Material	Other designation	Nominal composition [% wt]											
		C	**Si**	**Mn**	**Cr**	**Ni**	**Mo**	**Cu**	**Al**	**Ti**	**Fe**	**O**	**Zr**
Carbon steel	NS-EN S235JRG2	0.04	0.02	0.2	0.04	0.02		0.04	0.04		bal.		
Tit-based alloy	Ti-0.4Ni-3.6Mo-0.75Zr					0.44	3.4			bal.	0.18	0.16	0.74

Table 4 Summary of alloying elements in the nickel-based alloys tested in JA4

UNS no.	Nominal composition [% wt]								
	C	**Si**	**Mn**	**Cr**	**Ni**	**Mo**	**Cu**	**W**	**Fe**
N06255	0.03[a]	1.0[a]	1.0[a]	23-26	47.0-52.0	6.0-9.0	1.2[a]	3.0[a]	bal.
N06845	0.05[a]	0.5[a]	0.5[a]	20-25	44.0-50.0	5.0-7.0	2.0-4.0	2.0-5.0	bal.

[a)]*Minimum value*

Three flat coupon samples of each material were tested in each test reactor. Two longer coupon samples and one shorter coupon sample were accommodated in each test reactor. The longer test samples had dimensions of 100 mm x 7 mm x 1-2 mm the shorter coupon had a dimension of 50 mm x 7 mm x 1-2 mm as seen in Figure 4. The thickness of the coupons for each material depended on their availability from the producers.

Figure 4 Mounting piece (left) and three-flat coupon samples connected with alumina washers and fasteners after corrosion test

All the samples were ground to 600 grit with SiC abrasive paper before corrosion testing except for the HEA samples tested in journal article no. 2 (due to brittleness) which were not ground. The samples were then cleaned in an ethanol and ultrasound bath and weighed and measured according to ASTM G1-90 [30] before corrosion testing.

3.2 Testing Conditions

The conditions of the corrosion tests varied in this study. They are summarized in Table 5.

In the first journal article, the first few tests were conducted at lower concentrations of H_2S and CO_2 (30 and 80 mg/kg respectively) to verify the robustness and leak proofing of the test equipment before testing at higher concentrations. Testing of UNS N06255, N06845 and N06625 nickel-based alloys at lower H_2S and CO_2 concentrations were also done to test to investigate if the concentration level of the species had any significant effect on the corrosion behaviour in the test environment.

In all the corrosion tests, three reactors were connected in series where the test fluid entered the first reactor and eventually flowed out from the outlet of the third reactor. Figures 5 and 6 show a photo of the corrosion test equipment (the flow-through reactor test setup) developed in the study and a simplified process flow diagram of the setup.

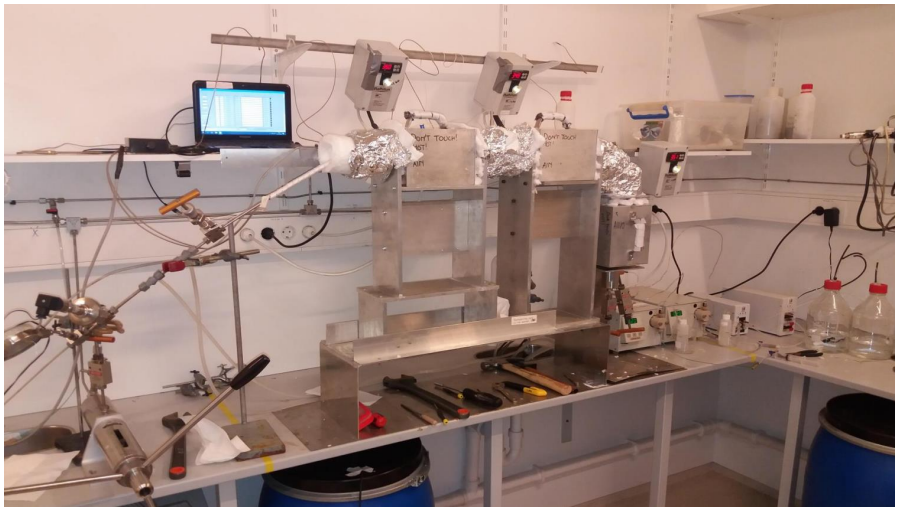

Figure 5 Test equipment for superhot test in all test volumes

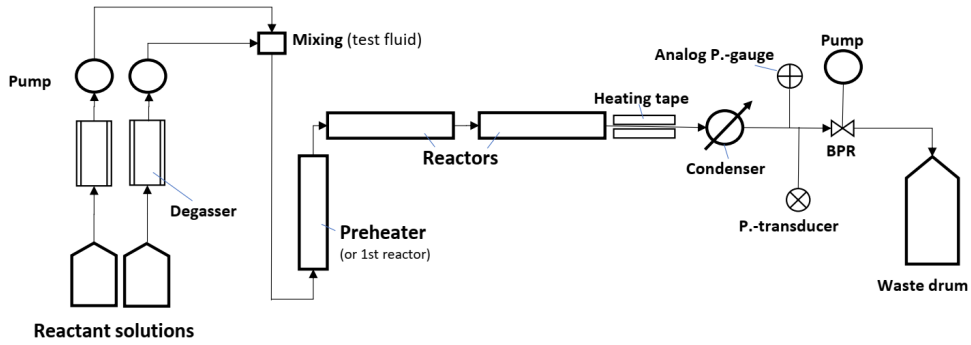

Figure 6 Simplified process flow diagram of the flow-through test setup

The first reactor was used in the majority of the tests, only as a preheater for the solution to achieve a superheated state before entering the second reactor. Hence, the first reactor did not accommodate any samples in the research outlined in the first two journal articles. In the third and fourth journal articles, however, the first reactor accommodated corrosion test samples to study the effect of the boiling state of the simulated geothermal fluid on the corrosion behaviour of the samples. Due to the expected high corrosion rate of the carbon steel tested in the aqueous geothermal fluid in the first and third reactor, only a 3-day test period was decided for the carbon steel tested and outlined in the third journal article.

In the first two journal articles, all the samples were tested at similar conditions i.e. synthetic superheated geothermal fluid at 350 °C and 10 barG. In the third journal article, however, the third reactor was at 180 °C to investigate the effect of condensed simulated HT geothermal fluid on the corrosion behaviour of the test samples.

In all the tests, deaerating of the flow-through test volume was done first with water at RT for 24 hours and then flushed and stabilized with superheated steam at 350 °C and 10 barG for 3 hours to stabilize the test volume before the simulated geothermal fluid entered the test volume. After each test period, the test volume was flushed with superheated steam at 350 °C and 10 barG to prevent condensation of the corrosive species in the test fluid when the test equipment was cooled down to room temperature (RT).

Risks involved with the experimental procedure are the exposure to high temperature and high pressure (an acidic) fluid and the danger of inhalation of hydrogen sulphide from gas leakage from the testing equipment. Hydrogen sulphide is well known to have a toxic effect on the nervous and respiratory systems [82]. For safety reasons, a gas detector, with H_2S (and CO_2) sensors was applied in the laboratory room near the testing equipment. Furthermore, the location of the gas detector was selected near the testing equipment and the sensor assembly was placed at the floor level due to the higher density of H_2S and CO_2 in comparison with the atmosphere. In addition, an alarm was triggered, a sound alarm from equipment and via SMS message to mobile phones of lab staff if the concentration of the gasses exceeded some threshold value (1 ppm for H_2S).

Table 5 Type of experiments and test conditions used in the study and presented in journal articles J1-J4

Journal Article	T [°C]	P [barG]	H_2S [mg/kg]	CO_2 [mg/kg]	HCl[a] [mg/kg]	pH[b]	Test fluid phase	Silica scale on samples	Test period [days]
#1	350	10	30 (and 150)	80 (and 250)	36.5	3	Superheated	None	21[c] (and 10)
#2	350	10	150	250	36.5	3	Superheated	None	10
#3	RT to 350	10	150	250	36.5	3	Boiling, Condensed and superheated	None	3 and 10
#4	RT to 350	10	150	250	36.5	3	Boiling and superheated	None and silica scale	10

[a] *From pH = 3*

[b] *At RT and condensed state*
[c] *One test was only at 16 days*

3.3 Sample & Fluid Preparation and Analysis

The test fluid preparation and analysis were done with known methods [83,84]. The testing fluid was prepared by a mixture of two aqueous reactant solutions, one reactant solution containing dissolved HCl and another reactant solution containing dissolved H_2S and CO_2 made by dissolving solid anhydrous >99.9% pure Na_2S and >99.7% pure solid $NaHCO_3$ from Sigma Aldrich in degassed deionized water. The two solutions were mixed in line to produce an aqueous and acid solution with pH = 3 with the desired concentration of H_2S, CO_2 and HCl and a background electrolyte Na^+ and Cl^-. The concentrations of the dissolved H_2S and CO_2 were further analysed using standard methods, i.e. Hg-precipitation titrations with a dithizone as an indicator for analysis of H_2S and modified alkalinity titration for total dissolved CO_2 [72,73].

During corrosion tests, the flow rate and pH of the fluid condensate at the outlet were regularly measured as well as the titration of H_2S and CO_2 of the fluid was done at the outlet to ensure the correct concentration in the test fluid. The flow rate was measured via the volumetric flow rate of the condensed fluid at the outlet of the cooled condensed fluid. The pH was analysed by taking samples from the outlet of the cooled condensed fluid. To conduct the titration of the outlet fluid, H_2S and CO_2 gases were extracted with 0.1 M NaOH solution to avoid the escape of the gases from the fluid and titrated with the method described earlier in this subchapter.

3.4 Test Equipment and Procedure

3.4.1 Development of Test Equipment

From the previous test of Jonsson [15], it was evident that modification of the flow-through test equipment was necessary to ensure superheated conditions in the test volume and exclude the boiling effect in the inlet and prevent condensation at the outlet of the test

volume. Furthermore, some design adjustments were made to maintain thermal stability in the test volume. In this study, some modifications were done by trial and error until satisfactory temperature measurements were obtained that indicated a superheated state of the test fluid in the test volume as outlined in conference papers no. 1 and 2 and journal article no. 1.

The first step in the development of modified test equipment and simulating HT geothermal environment was to connect in series three reactors together in a flow-through loop. The first reactor acted as a preheater but the following two reactors accommodated corrosion test samples when tested in a superheated fluid. The preheater was decided to be oriented vertically to increase the probability that small liquid droplets formed in the boiling at the inlet of the preheater, that may travel in the gas phase towards the first test reactor, would drop due to gravity back into the preheater in the relatively slow flow of the test fluid.

The preheater and reactors were all custom made at the University of Iceland by applying UNS N10276 reactor pipes 300 mm in length and with 11.7 mm inner diameter. The reactor pipes were inserted into an Aluminium cylinder that had been drilled through for the insert of the reactor pipes. In the Aluminium cylinders, extra holes for the insert of heating elements were also drilled. The Aluminium cylinder and reactor pipe were then wrapped with glass wool and assembled in thermally insulated refractory material forming an insulative box around the Aluminium cylinder and the reactor pipe. The whole assembly was then sealed by aluminium plates, bolted together to form a box. A controller from Rafhitun Ltd. was used to regulate the heat input and temperature in the tests.

Flow rates were also changed significantly from previous tests. The total flow was reduced from 1 ml/min (0.5 ml/min from each pump) down to 0.3 ml/min (0.15 ml/min each pump) which equals 1.2 cm/sec superficial velocity of the fluid at 10 barG and 350 °C. When flow was set to lower values, the variance was observed to be too high but a stable flow rate was achieved when each pump was set to 0.15 ml/min (0.3 ml/min total flow). Stable flow of each pump is required to maintain total flow and that the reactants to react.

To minimize heat loss between preheater and test reactors, the length of pipes connecting the preheater and the test volumes was minimized. Pipings between preheater and test reactors and at the outlet were also thermally insulated with flexible glass wool and wrapped with aluminium foil.

In the previous test by Jonsson [15], some condensation of superheated fluid was experienced at the outlet, likely due to the orientation of the reactor in a vertical position. To prevent condensation of the superheated test fluid at the outlet, the pipe length between the outlet of the second (last) reactor and the condenser was increased to minimize the effect of the condenser on the test fluid at the outlet of the second (last) reactor. Furthermore, a heating tape was wrapped around the pipe at the outlet of the second (last) reactor to heat the pipe and to ensure that the superheated state of the test fluid was maintained at the outlet of the second (last) reactor. The thermal tape was connected to an AC motor speed controller to regulate the heat input to the thermal tape. The control box was built for the whole assembly.

Some modifications were also done in the design and material selection of the test equipment to minimize corrosion of the material inside the hot testing and preheating

volume during the corrosion tests and affect the test results. All pipes at the inlet, outlet and between the preheater and test reactors were replaced by stainless steel to UNS N10276 corrosion-resistant nickel-based alloy. Furthermore, all copper ferrules were replaced with custom made Teflon ferrules.

The back-pressure regulator (BPR) from the previous test was replaced with a custom made back pressure regulator to prevent the accumulation of salts and plugging of the BPR during tests. In principle, the new BPR consists of outer housing that was filled with water where the pressure was regulated by a hand pump. Inside the housing, a flexible Viton™ hose was connected to the test flow-through loop. By exerting pressure on the outer house volume by the hand pump, the Viton™ hose was squeezed together, forming a small inner diameter flow-through channel which resulted in pressure build-up inside the test flow-through loop.

To monitor that no excess pressure build-up occurred in the flow-through loop during the test, a pressure transducer was connected to a data logger in the flow-through loop. The stability of pressure within the system was critical to maintaining phase equilibrium but excess pressure can result in condensation inside the test volume which must be avoided in tests in the superheated test fluid. The temperature of the reactor pipes was also monitored via K-type thermocouples connected to a data logger during the tests.

To verify the performance of the test equipment i.e. if the simulated HT geothermal fluid was superheated, the temperature was measured between the preheater and the test reactors and at the outlet of the second test reactor by a resistance temperature detector (RTD). This was also supported by the low uniform corrosion rate of carbon steel tested in the test reactors, thus the superheated condition of the test fluid could be concluded.

3.4.2 Description of Test Equipment

A detailed description of the test equipment is outlined in JA1. Two Chrom Tech series I pumps were used to pump the two reactant solutions. The solutions were degassed by Labhut degassers and then mixed before entering the preheater. The material in the flow-through loop in the hot temperature part of the flow line i.e. in the preheater, the reactors and tubing between the preheater and reactor, the tubing between reactors and tubing between the second reactor and pipe at the outlet towards the condenser was made of corrosion-resistant alloy UNS N10276. The sample holder and fasteners were made of Inconel UNS N06625 and UNS S31603 materials which were used depending on the alloy type of the sample in the testing batch. Washers between samples and fasteners are made of ceramic alumina provided by Ortech. The hot temperature part of the flow-through loop was highly insulated with ceramic material ($SiO_2/Al_2O_3/MgO$) and glass wool to minimize heat loss. The preheater, reactors, and heating units were custom made at the University of Iceland. The temperature of the reactors was regulated by a temperature controller and elements from Rafhitun. Thermocouples used in the system were K-type connected to the reactor pipes externally. Another set of thermocouples was connected to the reactor pipes externally to the Labjack U6 series data logger. Stainless steel and nickel-based alloy tubing, fittings and condenser were provided by SITEC. The piping at the outlet of the second reactor was wrapped with HTS Amptek heating tape and power input was controlled by an AC motor regulator. An analogue pressure meter was connected to the

flow line after the condenser. The Digital pressure transducer, WIKA model S-20, was connected to the Labjack U6 data logger to monitor the pressure in the flow-through loop system. The back-pressure regulator (BPR) was designed and custom made by Prologo to set and control fluid pressure in the system. The external pressure controller exerting on the BPR was a SITEC 750 hand pump.

3.4.3 Flow Setting of Equipment

The flow of the two pumps was set to 0.15 ml/min or a total volumetric flow rate of 0.3 ml/min which equals 1.2 cm/sec superficial flow velocity of the fluid in the reactors which were applied in all the tests. This flow rate is significantly lower than expected in in-situ geothermal wells as previously outlined in the introduction chapter. This flow rate corresponds to a reactor residence time of approximately 25 seconds in each reactor. The fluid injection, from the pumps, into the test volume was not continuous but was done in small discrete injection batches at a few seconds intervals. The pressure fluctuations (recorded at high resolution with pressure transducer and datalogger) were though only observed to be a few pascals during the injection batches and were therefore concluded to simulate continuous injection fairly well.

3.4.4 Testing: Pre and Post Procedures

In all the testing, flushing of air inside the test volume was done first with water at RT for 24 hours and then flushed and stabilized with superheated steam at 350 °C and 10 barG for 3 hours to stabilize the pressure and temperature in the test volume before the simulated geothermal fluid entered the test volume. After each test period, the test volume was flushed with superheated steam at 350 °C and 10 barG to prevent condensation of the corrosive species in the test fluid when the test equipment was cooled down to RT. Test samples were removed immediately from the test volume when the test equipment had dropped down to RT, samples were then dried and kept in a desiccator before the samples were processed for mass loss analysis or microstructural analysis. Before each test run, the test equipment was dismantled and the test pipes and reactor pipes were cleaned in strong HCl acid solution (and alkaline and organic solvent cleaned if needed).

3.4.5 Test Runs

For each test run, the reactant solutions were prepared in two flasks with several day reservoirs but each reactant flask was though only used for two days before new reactant solutions were prepared. This was done to maintain a high concentration of Na_2S and $NaHCO_3$ in the solutions. For each reactant solution prepared, titration and analysis of the concentration of the reactants were conducted. Flow measurements and pH measurements at the outlet were also conducted daily. Analysis of the sulphide and CO_2 concentrations in the test fluid was also done daily at the inlet but less frequently at the outlet. At the outlet where the fluid had been condensed and cooled, the gas and the liquid part of the test fluid were separated (acid fluid). It was observed that the gas from the test volume did not come regularly from the test volume but in a more irregular, discrete manner. As a result, the gas concentration of H_2S and CO_2 were highly irregular and therefore concluded to be insignificant in concluding the average H_2S and CO_2 concentration at the outlet. The temperature of the preheater and reactors and pressure inside test volume were monitored continuously via a datalogger.

Due to the aggressive test environment (corrosive fluid, thermal expansion and contraction of equipment materials) substantial maintenance work and replacement of accessories for the test equipment needed to be done between test periods. The reactor tubes and pipings in the high-temperature part of the test equipment needed regularly (approximately every third test run) needed to be fixed and milled by a private owned professional maintenance shop (Vélvik Ltd.) which took normally few weeks. This needed to be done to make the equipment leak-proof and efficient for the tests. Pump parts and fittings were also replaced regularly due to wear and degradation.

3.4.6 Limitation of Experimental Design

In this study, flow-through test equipment was established to simulate high-temperature geothermal conditions. The test equipment and test conditions have though some limitations that should be mentioned:

Small volume reactors – Due to the small volume of the test reactors/preheater and rapid heating of the fluid, it cannot be neglected that some microdroplets (liquid) have been transported between the preheater and the test reactors. It is well known in boiler systems that liquid droplets can be carried over from the boilers [85]. This may have affected the phase condition and equilibrium in the test volumes.

Preheater and reactor tube material not inert – The UNS N10276 reactor tubes and UNS N06625 pipe material were not completely insusceptible to corrosion. Some corrosion damage was observed at the inlet of the preheater. These corrosion products may have been transported to the test volume where test samples were accommodated, affecting the results and conclusion of the study.

3.5 Mass Loss Analysis

The measured corrosion rate (CR) of the material tested in mm/year was calculated via the MLM and according to ASTM G1-90 [30]:

$$\mathrm{CR} = \frac{K \cdot W}{A \cdot t \cdot \rho} \tag{20}$$

where K is the corrosion rate constant equal to $8.76 \cdot 10^4$, W is the mass loss in grams of the tested material with a ±0.00005 gram precision, A is the exposed surface area in cm^2 of a tested sample, t is the exposure time in hours, and ρ is the material density in g/cm^3. For MLM analysis, the samples were cleaned to remove corrosion products according to ASTM G1-90. It is to be noted here that there is no standard cleaning procedure available for Ti-based alloys due to extreme adhering to the titanium oxide film. Therefore, the Ti-based alloy in the experiment was only cleaned with ethanol in the ultrasonic bath after testing.

3.6 Microstructural Analysis

3.6.1 Etching for Grain Boundary Analysis

Following etching solutions were applied for grain boundary analysis in journal article 1. For grain boundary analysis, 2% nital [86] was used for the etching of carbon steel S235JRG2. Kroll´s reagent [87] was used for the etching of alloy Ti-4Al-4Mo-2Sn. Mixed acids [88] were used for etching the nickel-based alloys and the austenitic stainless steels.

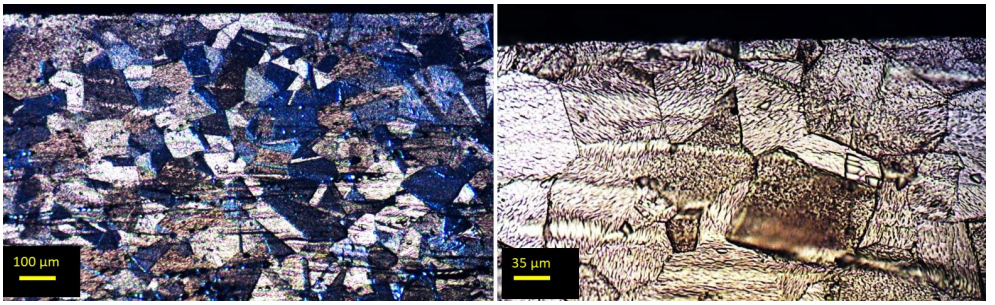

Figure 7 Etching of austenitic stainless steel UNS 31254 at two magnifications after test in superhot fluid at 350 °C and 10 barG with H_2S = 150 ppm and CO_2 = 250 ppm and pH = 3 upon condensation

3.6.2 Microstructure and Chemical Composition Analysis

For microstructural and chemical composition analysis scanning electron microscope (SEM) and X-ray electron dispersive spectroscopy (XEDS) were used. The samples used for the microstructural analysis were sectioned using a diamond wafering blade, then mounted in thermosetting phenol-formaldehyde resin (i.e., bakelite) and cast under pressure. The samples were ground to 1000 grit with SiC abrasive paper and polished with 3 µm and 1 µm diamond paste slurry and 0.02-0.06 µm particle size colloidal silica. The samples were analysed using SEM and XEDS before and after the corrosion testing to examine corrosion effects (corrosion damages), for grain boundary analyses and evaluation of the corrosion film structure and composition. The SEM equipment used was a Zeiss Supra 25. The XEDS instrument used was Oxford Instruments with Si(Li) X-ray detector and INCA Energy 300 and with AzTec software.

3.6.3 Crystal Structure Analysis

X-ray diffraction (XRD) analysis was used for crystal structure analysis of the materials. For the bulk materials tested an X´Pert Pro MRD system from PANalytical with a Göbel mirror on the incident side and parallel plate collimator on the diffracted side was used. The data were collected in a standard θ-2θ geometry and analysed with the HighScore software. Samples were analysed by XRD before and after the corrosion testing.

For the crystal structure analysis of the powders of the geothermal brine scaling material (amorphous and crystal) present on the samples in the second and third reactor a Bruker AXS D8 Focus, X-Ray Diffractometer was used, with Ni-filtered Cu ka radiation at 1.54 Å wavelength at 40 mA and 40 kV with fixed 1° slit and NaI oscillation counter. Validation/calibration of the Bruker D8 Focus X-ray diffractometer was performed using NIST (SRM-1976) standard sample.

4 Results

4.1 Summary of Results of Journal Articles

4.1.1 Journal Article 1 (JA1)

A.I. Thorhallsson, A. Stefansson, D. Kovalov, S.N. Karlsdottir, Corrosion testing of materials in the simulated superheated geothermal environment, Corros. Sci. 168 (2020) 108584. https://doi.org/10.1016/j.corsci.2020.108584.

A.I. Thorhallsson, A. Stefansson, D. Kovalov, S.N. Karlsdottir, Corrigendum to "Corrosion testing of materials in a simulated superheated geothermal environment" [Corros. Sci. 168 (2020) 10], Corros. Sci. 174 (2020) 108807. https://doi.org/10.1016/j.corsci.2020.108807.

Summary of results of journal article 1:

In this article, the aim was to investigate the corrosion behaviour of the materials in a simulated HT geothermal environment where carbon steel and corrosion-resistant alloys were tested in superheated steam containing H_2S, CO_2 and HCl at 350 °C and 10 barG with condensate of pH =3 at RT. As expected, the general corrosion rate was extremely low for all the materials tested but carbon steel was the only material tested that was prone to localized corrosion damage. In the article, it is concluded that HCl had a significant contribution to the localized corrosion damage. The results and conclusions made in journal article 1 contribute to the answer of RQ1 i.e. superheated steam of geothermal origin results in localized corrosion damage in carbon steel.

4.1.2 Journal Article 2 (JA2)

A.I. Thorhallsson, I. Csáki, L.E. Geambazu, F. Magnus, S.N. Karlsdottir, Effect of alloying ratios and Cu-addition on corrosion behaviour of CoCrFeNiMo high-entropy alloys in superheated steam containing CO_2, H_2S and HCl, Corros. Sci. 178 (2021) 109083. https://doi.org/10.1016/j.corsci.2020.109083.

Summary of results of journal article 2:

High-entropy alloys (HEAs) containing CoCrNiFeMo (4 alloys) and CoCrNiFeMoCu (2 alloys) with different molar ratios were tested in the same environment as in journal article 1. The CoCrNiFeMoCu alloys were prone to general corrosion and localized damage which was accelerated by Cu-rich intermetallics. In this study, it was concluded that H_2S was the main corrosive factor for the CoCrNiFeMoCu alloys. The other CoCrNiFeMo alloys were not prone to corrosion damage. These results contribute to the answer to RQ1.

4.1.3 Journal Article 3 (JA3)

A.I. Thorhallsson, S.N. Karlsdottir, Corrosion Behaviour of Titanium Alloy and Carbon Steel in a High-Temperature, Single and Mixed-Phase, Simulated Geothermal Environment Containing H_2S, CO_2 and HCl, Corros. Mater. Degrad. 2 (2021) 190–209. https://doi.org/10.3390/cmd2020011.

Summary of results of journal article 3:

Testing of carbon steel and corrosion-resistant titanium alloy was conducted at three separate testing reactors connected in series in an H_2O testing fluid containing H_2S, CO_2 and HCl with condensate of pH = 3 at 10 barG. The first reactor heated the testing fluid from RT to a boiling state (~184 °C for pure steam) and eventually to a superheated state at 350 °C. The second reactor maintained a superheated state at 350 °C but the temperature was lowered down to 180 °C in the third reactor which resulted in condensation of the test fluid. The carbon steel showed localized corrosion damages in all three test reactors but the extent of corrosion was more severe when samples were exposed to the liquid state of the test fluid (in the first and third reactor). The titanium alloy was not prone to corrosion in the test environment. These results show that distinct corrosion behaviours can be expected for materials susceptible to corrosion in different phase states of the geothermal fluid. These results and conclusions contribute to the answer to RQ3.

4.1.4 Journal Article 4 (JA4)

A.I. Thorhallsson, A. Stefansson, S.N. Karlsdottir, Silica scaling and boiling effect on corrosion behaviour of nickel-based alloys associated with superheated hydrothermal fluids containing HCl, H_2S and CO_2, Geothermics 101 (2022) 102384. https://doi.org/10.1016/j.geothermics.2022.102384

Summary of results of journal article 4:

Nickel-based alloys were tested in the same test environment as reported in journal articles 1 and 2 with the exception that the materials were coated with amorphous silica from geothermal brine during the test to investigate if the amorphous silica coating contributed to some localized corrosion damage in the materials. The amorphous silica-coated nickel-based alloys were not prone to corrosion damage in the superheated geothermal fluid indicating that the silica does not promote localized corrosion damage in corrosion-resistant alloys in the test environment. These results and conclusions contribute to the answer to RQ2.

4.2 Summary of results of conference papers

4.2.1 Conference Paper 1

Andri I. Thorhallsson, S.N. Karlsdottir, A. Stefansson, Corrosion Testing of UNS N06625 in a Simulated High-Temperature Geothermal Environment, PROCEEDINGS in CORROSION 2018 Conference and Expo, April 15-19, Phoenix, Arizona, USA, paper no. 11058

Summary of results of a conference paper I:

A 3-week corrosion testing of UNS N06625 was conducted in superheated steam with H_2S, CO_2 and HCl at 350°C and 10 bars at the early stage of the development of test equipment and setup. The result of the simulated experiment showed that some localized corrosion and sulphide crystals occurred on some of the samples, indicating that the test conditions were not homogeneous in the test volume. The result of this study led to further improvement of test equipment.

4.2.2 Conference Paper II

Andri I. Thorhallsson, S.N. Karlsdottir, A. Stefansson, Corrosion Testing of UNS S31603 in Simulated HT Geothermal Environment at Boiling, Superheated and Condensation Conditions, PROCEEDINGS in CORROSION 2019 Conference and Expo, March 24-28, 2019, Nashville, Tennessee, USA, paper no. 13195.

Summary of results of conference paper II:

Corrosion testing of austenitic stainless steel, UNS S31603 (AISI 316L), was conducted in flow-through reactors during the first stages of lab setup development to obtain a superheated steam environment with H_2S/CO_2/HCl at 350°C and 10 bars. As in conference paper I, various corrosion forms and products were observed in the UNS S31603 samples tested indicating that the test setup and conditions were not homogeneous in the test volume. The result of this study led to further improvement of test equipment to make test conditions homogeneous and the fluid superheated when aimed.

4.2.3 Conference Paper III

Andri Isak Thorhallsson, Ioana Csaki, Sigrun Nanna Karlsdottir, Laura Elena Geambazu, $Co_{20}Cr_{20}Fe_{20}Ni_{20}Mo_{20}$ high entropy alloys behavior in superheated geothermal steam, PROCEEDINGS IN WGC 2020+1, 2021.

Summary of results of conference paper III:

Equiatomic high entropy alloys (EHEA), $Co_{20}Cr_{20}Fe_{20}Ni_{20}Mo_{20}$ and copper added $Co_{16.67}Cr_{16.67}Fe_{16.67}Ni_{16.67}Mo_{16.67}Cu_{16.67}$ were tested in superheated steam containing H_2S, CO_2 and HCl at 350°C and 10 bar gauge. The samples were prepared using the vacuum arc melting (VAM) technique. The results showed that HEAs could be promising candidates as a coating material for high-temperature geothermal applications but some corrosion was observed in the Cu added HEA alloy. This study contributed partly to the results published in JA2. The results in JA2 cover the whole results and conclusions outlined in conference paper III.

4.2.4 Conference Paper IV

Andri I. Thorhallsson, Sigrun Nanna Karlsdottir, William MacDonald, James S. Grauman, Titanium Alloy Casing for High-Temperature Geothermal, PROCEEDINGS IN WGC 2020+1, 2021.

Summary of results of conference paper IV:

A new titanium alloy and carbon steel were tested in a temperature range of 180-350 °C in three testing units connected in series; in the first reactor where the rapid heating and boiling of the aqueous testing solution from RT to boiling and superheating of the fluid occurred (~184 °C for pure water), in the second reactor where superheated conditions at 350°C and in the third reactor where the temperature was set to 180°C or below the saturation temperature of the fluid to provoke condensation in the test chamber. The corrosion behaviour of carbon steel was used as a test fluid phase condition indicator in all three test volumes. The new titanium alloy was not susceptible to corrosion in all three test volumes and was hence concluded to have good corrosion resistance in liquid and gaseous fluid conditions. The titanium alloy could hence be a promising future candidate material in geothermal environments.

4.3 Answers to Research Questions – Study Results

The objective of the PhD project was to investigate the corrosion behaviour of materials in a simulated HTD geothermal environment to answer the three research questions (RQ1-RQ3) addressed before in the dissertation:

RQ1: Does superheated fluid, where the bulk is H_2O that contains H_2S, CO_2 and HCl, promote localized corrosion damage in carbon steel or corrosion-resistant alloys tested in this study?

Answer to question 1: Localized corrosion damage was observed in the carbon steel tested in journal articles 1 & 3 and in the Cu added HEA in journal article 2. Localized corrosion damage was not observed in other materials i.e. corrosion-resistant alloys tested. In the carbon steel, prone to localized corrosion damage, the reaction of HCl with the carbon steel to form Cl rich pits under the sulphide sublayer and magnetite layer was concluded to be the cause of the localized corrosion damage as outlined in JA1. The corrosion behaviour of carbon steel in the test fluid in a liquid state showed distinct corrosion behaviour than in the test fluid in a superheated state. The Cu added HEAs were prone to general and localized corrosion damage due to the reaction of H_2S from the simulated geothermal fluid with Cu in the HEA tested. The corrosion rate was increased by Cu-rich intermetallic phases observed in the higher Cu alloyed HEA reported in journal article 2.

RQ2: Does commonly observed scaling (i.e. amorphous silica) promote localized corrosion damage on a material surface in superheated steam of geothermal origin/nature?

Answer to question 2: No localized corrosion damage was observed in the silica covered corrosion-resistant alloys tested in the simulated superheated geothermal environment. As a result, silica does not promote localized corrosion damage in the simulated superheated geothermal environment as outlined in journal article no. 4. Some corrosion products were observed on the samples indicating corrosion damage occurring, likely associated with the boiling regime in the test volume, but no evidence of localized corrosion damage or corrosion damage induced by silica deposits could be observed.

RQ3: Is there a significant difference in material corrosion behaviour depending on the phase properties of the solution, i.e. the fluid is superheated or in a liquid state

Answer to question 3: Yes, more corrosion rate and localized corrosion damage were observed in carbon steel tested in a liquid state in comparison with testing in the gaseous state of the simulated HT deep geothermal test fluid containing H_2S, CO_2 and HCl with pH = 3 at condensate as outlined in journal article no. 3. This result applies to carbon steel that is susceptible to corrosion both in the liquid and gaseous state of the test fluid but showed different corrosion behaviours for the different states of the test fluid.

5 Discussion and Conclusions

In this study, corrosion tests were conducted in well-controlled conditions in laboratory equipment to simulate high temperature (HT) geothermal environments. When the study started, few such tests had been conducted before and the need for a similar test environment in a laboratory was obvious. The results of this study have without doubt increased our understanding of such corrosion behaviour of various materials in relevance to high-temperature deep (HTD) geothermal environments and can provide input for the decision making of appropriate material selection for HT deep geothermal systems.

This study shows that the corrosion rate, in superheated HTD geothermal fluid, is low for carbon steel and corrosion-resistant alloys. The corrosion rate can though be significantly accelerated for susceptible materials when the gaseous superheated fluid undergoes condensation (partly or fully) or when the liquid geothermal fluid undergoes boiling from liquid to gaseous state. The novelty of this study is the increased understanding of the effect of HTD geothermal fluid containing H_2S, CO_2 and HCl on the localized corrosion behaviour of materials. Carbon steel was prone to corrosion in all the environments tested containing H_2S, CO_2 and HCl. The localized corrosion damage of carbon steel in the superheated HTD geothermal environment is concluded to be driven by HCl as explained in JA1. The synergy effect of H_2S and CO_2 with the HCl may though not be neglected. Dry, superheated HTD geothermal environments, not containing HCl or any condensates in the geothermal fluid, could hence likely result in less corrosion damage for the carbon steel and hence, could make the carbon steel a feasible equipment material in such geothermal environments. From the previous in-situ studies of carbon steel and corrosion-resistant alloys by Karlsdottir et al. [10], localized corrosion damage was observed in the carbon steel but also in all the corrosion-resistant materials tested. In these tests, a very long exposure period (113 days) was applied and the geothermal fluid contained H_2S, CO_2, HCl but also HF and H_2. Previous corrosion study results, in simulated HT geothermal environments, by Jonsson [15] indicated that a few days or weeks test period would result in some significant corrosion products in the materials tested. As a result, a 10-day test period for most of our corrosion tests was selected. In our study, only H_2S, CO_2 and HCl were applied in the test fluid to reduce the complexity of the system and to investigate further the effect of these chemicals on the corrosion behaviour of the materials. Furthermore, HF was not an option as a chemical in the test fluid due to the volatility and extreme toxic danger effects of the chemical [89,90]. From the results of this dissertation and comparison with the previous in-situ test, it can be concluded that HF, H_2 and/or long exposure periods are likely contributors to localized corrosion damage that was experienced in the in-situ test.

High-entropy alloys (HEAs) are a relatively new type of alloys that have little or no experience in application in the geothermal industry as a bulk or a coating material. The HEAs could be an interesting choice as a corrosion-resistant coating material. In this study, four CoCrNiFeMo alloys and two CoCrNiFeMoCu alloys were tested in a simulated HT geothermal environment. The result of this study indicates that the CoCrNiFeMo alloys could be applicable as a coating material in HTD geothermal environments as no significant corrosion damage was observed in all the alloys. The Cu added CoCrNiFeMoCu alloys however were prone to corrosion as the Cu rich phase was prone to dissolution induced by the reaction of Cu with H_2S.

A correct selection of equipment/casing materials could aid in the prevention of corrosion damage in HTD geothermal systems. From the perspective of the application of some corrosion-resistant alloys in HTD geothermal environments, the most economical alloy tested (for example stainless steel UNS S31254) in this study could be a feasible candidate for future material selection in geothermal equipment/casing as the corrosion rate was measured very low for all the corrosion-resistant alloys tested. The nickel-based alloys and the new titanium alloy, Ti-0.4Ni-3.6Mo-0.75Zr, have good mechanical strength at HT and should therefore be considered as a promising future application material in an HT geothermal environments.

This study provides also a comprehensive analysis of the design criteria for experimental setup for an HT flow-through system for future research in the field of simulating HT geothermal environment for corrosion tests. In this study, the limitations of the test setup and facility design are described in detail which will aid in the future development and design of next-generation testing facilities in the area of high-temperature corrosion laboratory testing. Which will add to the tools that can be used for the geothermal industry and scientific community in the field of corrosion where limitations have existed in experimental corrosion facilities and a gap of knowledge in experimental data from corrosion testing of materials at temperatures above 200°C in H_2O fluid with geothermal gasses such as H_2S, CO_2 and HCl.

In addition, the methodology in this study, to conclude on the test fluid phase condition inside the test volume from a corrosion gradient results in low corrosion-resistant samples located along the small test volume, is a practical approach when a small test volume excludes the possibility to install low corrosion-resistant thermocouples inside the test volume.

5.1 Contribution of Dissertation

The results reported in this dissertation will aid in the future selection of materials and future design and engineering of geothermal systems to maximize the lifetime of equipment and economics of deep geothermal energy utilization in a fluid containing H_2S, CO_2 and HCl. Carbon steel is concluded not to be a feasible material in HTD geothermal environments containing HCl where it was concluded to be the key corrosive factor in HTD geothermal environments containing H_2S, CO_2 and HCl as outlined in journal articles 1 and 3. Copper containing HEA materials are also concluded to be not feasible materials due to the corrosive effect of H_2S on the Cu rich phases or Cu rich intermetallic phases as outlined in journal article 2. This study also supports the conclusion that silica scaling is not likely to promote localized corrosion damage in HTD geothermal environments as outlined in journal article 4 and hence is likely to have some protective effect on the material from the corrosive effect of the geothermal fluid.

The scientific contribution is a deeper understanding of corrosion mechanisms and the effect and contribution of the common corrosive species (H_2S, CO_2, HCl) observed in high-temperature or deep geothermal systems. This dissertation also contributes to the further development of improved test equipment to simulate HT geothermal environments for future corrosion studies.

5.2 Validity of the Test Environment

In this study, one of the aims was to simulate in-field HTD geothermal conditions in a laboratory test setup with a scientific approach. Due to some technical and time-consuming challenges, some items should be mentioned that may have affected the validity of the results.

Due to long preparation and post-test procedures and numbers of planned test batches, only one test run was conducted for each test batch case (alloys in the test environment) i.e. the same test was not repeated or done multiple times to verify if the results were reproducible. The single tests conducted were done with precision and standard procedure.

The concentration of oxygen was not analysed in the test fluid due to technical limitations of the test equipment. The test fluid was degassed (vacuum degasser) before injection into the test volume. As the flow rate of the test fluid was extremely low, the degassing was very effective but it should be noted that the prevention of ingress of dissolved oxygen with the test fluid into the test volume cannot be completely guaranteed.

Application of deionised water before and after the test period might have possibly affected the corrosion of carbon steel as it is known that H_2O at a high temperature can oxidize iron [91] but the test fluid had to be flushed with deionized H_2O at the heating up and cooling period, before and after the test period. Because of the relatively short time of this procedure, it is not considered to have affected the overall conclusion of the study of the corrosion behaviour of the carbon steel in the simulated deep geothermal environment.

Due to the function of the fluid pumps, the test fluid injection into the test volume was not continuous but was done in batches in few seconds intervals to achieve the average flow per minute. As a result, continuous steady-state conditions of the test fluid in the test volume were not guaranteed due to these discrete test fluid injections. It shall though be noted that the test pressure was observed stable during the test period (within a few Pa). This stability was experienced because an extremely small liquid volume of the test fluid was injected in every discrete injection and hence, no big pressure fluctuations in the test loop were observed.

5.3 Future work

Recommendations for future work will be divided into two categories in this chapter; firstly the improvement(s) that can be done in the test setup to simulate HTD geothermal environments and secondly further corrosion studies that could improve understanding of the effect of individual factors in HTD geothermal environments on the corrosion behaviour of materials.

5.3.1 Improvement of Test Setup and Methodology

For the improvement of test equipment, the improved design should aim to ensure that sufficient heat transfer from preheaters to the test fluid occurs during the flow-through testing and prevent possible liquid microdroplets transportation between preheater and test reactor(s). This could be done by increasing the length of the preheaters, installing pumps with higher precision at lower volumetric flow rates or application of hot moisture traps between preheaters and test reactors.

Application of H_2S and CO_2 gas instead of Na_2S and $NaHCO_3$ reactants to prevent the formation of NaCl salt deposits in the test reactor could also aid to have a more representative simulated test fluid i.e. reflecting more in-situ conditions. This is though only capable if no H_2S leakproof or exposure is fulfilled.

Application of inert gas (N_2, argon) for flushing out atmospheric air before the test period and flushing out superheated test fluid after the test period could exclude the oxidizing effect of hot H_2O during heat up and cooling of the test fluid.

5.3.2 Further Research Recommendations

To gain a better understanding of the effect of HT or HTD geothermal environments on the corrosion behaviour of carbon steel and corrosion-resistant alloys following investigations could be conducted:

- Testing at higher pressures in superheated or supercritical HTD geothermal fluid. Pressure affects the conductivity of the geothermal fluid and hence can affect the corrosion behaviour of the materials to incline towards "dry corrosion" or "wet corrosion" behaviour.
- Testing in the same test environment, as tested in this dissertation, but only include H_2S, CO_2 or HCl separately in each test batch to investigate the contribution of every single factor (excluding the possible synergistic effect of chemical species) on the corrosion behaviour of materials.
- The corrosion reaction mechanism of HCl in carbon steel in a superheated geothermal environment containing H_2S, CO_2 and HCl should be investigated further. From the results, it is not evident how the proposed reaction of volatile iron chloride with H_2O to form Fe_3O_4 and other corrosion products proceeds.
- Testing with HF or H_2 to study the effect on localized corrosion damage behaviour as a result of previous in-situ tests and the result of this dissertation indicates that either species could be the root cause of localized corrosion damage experienced in previous in-situ tests.
- Test in simulated HT or HTD geothermal environment in prolonged exposure periods (>100 days) to investigate the effect of long term exposure.
- Testing at higher temperatures (400 – 600 °C) to investigate the effect of higher temperatures on the corrosion behaviour would be interesting. Corrosion phenomena such as decarburization or hydrogen damage could be more profound at higher temperatures.

5.4 Conclusions

From this study the following conclusions and findings can be summarized:

- Localized corrosion damage can be experienced in materials when exposed to a superheated fluid of geothermal origin. In our study, carbon steel and Cu added HEA was prone to corrosion damage in a superheated fluid of geothermal origin.

- Carbon steel and Cu added HEA were prone to corrosion damage in dry superheated high temperature simulated geothermal fluid but other corrosion-resistant alloys were not susceptible to corrosion.
- The corrosion behaviour in a geothermal fluid in a dry or a liquid state is distinct for materials prone to corrosion.
- Scaling deposits i.e. amorphous silica, do not promote localized corrosion damage of the nickel-based alloys tested in this study.

This PhD project has contributed to increased understanding of corrosion behaviour of materials in dry and liquid state geothermal fluid and can assist in the aid of proper material selection for future HT geothermal power utilization. Also, a limited number of test setups at temperatures above 200°C in a controlled, simulated HT geothermal environment have been established before and as a result, this study provides valuable results and methodology for future research and design of test equipment in this field.

References

[1] M.R. Karlsdottir, J. Heinonen, H. Palsson, O.P. Palsson, Life cycle assessment of a geothermal combined heat and power plant based on high temperature utilization, GEOTHERMICS. 84 (2020). https://doi.org/10.1016/j.geothermics.2019.101727.

[2] M.R. Karlsdottir, J. Heinonen, H. Palsson, O.P. Palsson, High-Temperature Geothermal Utilization in the Context of European Energy Policy-Implications and Limitations, ENERGIES. 13 (2020). https://doi.org/10.3390/en13123187.

[3] R. Corsi, Scaling and corrosion in geothermal equipment: Problems and preventive measures, GEOTHERMICS. 15 (1986) 839–856.

[4] I. Gunnarsson, S. Arnorsson, Impact of silica scaling on the efficiency of heat extraction from high-temperature geothermal fluids, GEOTHERMICS. 34 (2005) 320–329. https://doi.org/10.1016/j.geothermics.2005.02.002.

[5] S. Arnórsson, Geothermal systems in Iceland: Structure and conceptual models—I. High-temperature areas, Geothermics. 24 (1995) 561–602. https://doi.org/10.1016/0375-6505(95)00025-9.

[6] G.O. Fridleifsson, W.A. Elders, A. Albertsson, The concept of the Iceland deep drilling project, GEOTHERMICS. 49 (2014) 2–8. https://doi.org/10.1016/j.geothermics.2013.03.004.

[7] G.O. Fridleifsson, W.A. Elders, R.A. Zierenberg, A.P.G. Fowler, T.B. Weisenberger, K.G. Mesfin, O. Sigurdsson, S. Nielsson, G. Einarsson, F. Oskarsson, E.A. Gudnason, H. Tulinius, K. Hokstad, G. Benoit, F. Nono, D. Loggia, F. Parat, S.B. Cichy, D. Escobedo, D. Mainprice, The Iceland Deep Drilling Project at Reykjanes: Drilling into the root zone of a black smoker analog, J. Volcanol. Geotherm. Res. 391 (2020). https://doi.org/10.1016/j.jvolgeores.2018.08.013.

[8] W.A. Elders, G.O. Fridleifsson, B. Palsson, Iceland Deep Drilling Project: The first well, IDDP-1, drilled into magma Preface, GEOTHERMICS. 49 (2014) 1. https://doi.org/10.1016/j.geothermics.2013.08.012.

[9] G.O. Fridleifsson, W.A. Elders, R.A. Zierenberg, A. Stefansson, A.P.G. Fowler, T.B. Weisenberger, B.S. Hardarson, K.G. Mesfin, The Iceland Deep Drilling Project 4.5km deep well, IDDP-2, in the seawater-recharged Reykjanes geothermal field in SW Iceland has successfully reached its supercritical target, Sci. Drill. 23 (2017) 1–12. https://doi.org/10.5194/sd-23-1-2017.

[10] S.N. Karlsdottir, K.R. Ragnarsdottir, I.O. Thorbjornsson, A. Einarsson, Corrosion testing in superheated geothermal steam in Iceland, Geothermics. 53 (2015) 281–290. https://doi.org/10.1016/j.geothermics.2014.06.007.

[11] W.A. Elders, G.O. Fridleifsson, A. Albertsson, Drilling into magma and the implications of the Iceland Deep Drilling Project (IDDP) for high-temperature geothermal systems worldwide, GEOTHERMICS. 49 (2014) 111–118. https://doi.org/10.1016/j.geothermics.2013.05.001.

[12] B. Palsson, S. Holmgeirsson, A. Gudmundsson, H.A. Boasson, K. Ingason, H. Sverrisson, S. Thorhallsson, Drilling of the well IDDP-1, GEOTHERMICS. 49 (2014) 23–30. https://doi.org/10.1016/j.geothermics.2013.08.010.

[13] T. Hauksson, S. Markusson, K. Einarsson, S.N. Karlsdóttir, Á. Einarsson, A. Möller, Þ. Sigmarsson, Pilot testing of handling the fluids from the IDDP-1 exploratory geothermal well, Krafla, N.E. Iceland, Geothermics. 49 (2014) 76–82. https://doi.org/10.1016/j.geothermics.2013.07.003.

[14] D. B. van den Heuvel, E. Gunnlagsson, L.G. Benning, Passivation of metal surfaces against corrosion by silica scaling, in: 41st Workshop Geotherm. Reserv. Eng., Stanford, California, 2016.

[15] T. Jónsson, Corrosion Testing in a Simulated High Temperature Geothermal Environment, M.Sc. Thesis, University of Iceland, 2015.

[16] S.N. Karlsdottir, I.O. Thorbjornsson, K.R. Ragnarsdottir, A. Einarsson, Corrosion Testing of Heat Exchanger Tubes in Steam from the IDDP-1 Exploratory Geothermal Well in Krafla, Iceland, in: Corros. 2014, NACE International, San Antonio, Texas, USA, 2014: p. Paper no. NACE-2014-4152.

[17] I.O. Thorbjornsson, B.C. Krogh, G.S. Kaldal, G. Rørvik, S.S. Jonsson, F. Oskarsson, O. Sigurdsson, H. Husby, A. Ragnarsson, I.-I. Geosurvey, Corrosion Testing in Direct Geothermal Steam of Cladded and Standalone Materials at 210°C and 450°C, in: World Geotherm. Congr. 2020 1, Reykjavik, Iceland, 2021.

[18] I.O. Thorbjornsson, G.S. Kaldal, B.C. Krogh, B. Palsson, S.H. Markusson, P. Sigurdsson, A. Einarsson, B.S. Gunnarsson, S.S. Jonsson, Materials investigation of the high temperature IDDP-1 wellhead, GEOTHERMICS. 87 (2020). https://doi.org/10.1016/j.geothermics.2020.101866.

[19] N. Yanagisawa, Y. Masuda, H. Asanuma, K. Osato, K. Sakura, Estimation of casing material corrosion rates for supercritical geothermal development, GEOTHERMICS. 96 (2021). https://doi.org/10.1016/j.geothermics.2021.102149.

[20] Y. Kurata, N. Sanada, H. Nanjo, J. Ikeuchi, Casing pipe materials for deep geothermal wells, Geotherm. Resour. Counc. Trans. 19 (1995) 105–109.

[21] J. Nogara, S.J. Zarrouk, Corrosion in geothermal environment Part 2: Metals and alloys, Renew. Sustain. Energy Rev. 82 (2018) 1347–1363. https://doi.org/10.1016/j.rser.2017.06.091.

[22] J. Nogara, S.J. Zarrouk, Corrosion in geothermal environment: Part 1: Fluids and their impact, Renew. Sustain. ENERGY Rev. 82 (2018) 1333–1346. https://doi.org/10.1016/j.rser.2017.06.098.

[23] T. Kaya, P. Hoshan, Corrosion and Material Selection for Geothermal Systems, in: World Geotherm. Congr. 2005, Antalya, Turkey, 2005.

[24] R. Rihan, B. Al-Wakaa, N. Tanoli, H. Shalaby, The susceptibility of P110 downhole tubular steel to sulfide stress cracking in H2S and NaCl, J. Pet. Sci. Eng. 174 (2019) 1034–1041. https://doi.org/10.1016/j.petrol.2018.10.102.

[25] M. Monnot, R.P. Nogueira, V. Roche, G. Berthomé, E. Chauveau, R. Estevez, M. Mantel, Sulfide stress corrosion study of a super martensitic stainless steel in H2S sour environments: Metallic sulfides formation and hydrogen embrittlement, Appl. Surf. Sci. 394 (2017) 132–141. https://doi.org/10.1016/j.apsusc.2016.10.072.

[26] D. Jingen, Y. Wei, L. Xiaorong, D. Xiaoqin, Influence of H2S Content on CO2 Corrosion Behaviors of N80 Tubing Steel, Pet. Sci. Technol. 29 (2011) 1387–1396. https://doi.org/10.1080/10916466.2010.545784.

[27] J. Banaś, U. Lelek-Borkowska, B. Mazurkiewicz, W. Solarski, Effect of CO2 and H2S on the composition and stability of passive film on iron alloys in geothermal water, Electrochimica Acta. 52 (2007) 5704–5714. https://doi.org/10.1016/j.electacta.2007.01.086.

[28] Y. Gui, Z. Liang, Q. Zhao, Corrosion and Carburization Behavior of Heat-Resistant Steels in a High-Temperature Supercritical Carbon Dioxide Environment, Oxid. Met. 92 (2019) 123–136. https://doi.org/10.1007/s11085-019-09917-x.

[29] L. Krumm, M.C. Galetz, Chlorine Attack of Carbon Steel Between 350 and 500 degrees C and Its Importance Regarding Corrosion in Waste Incineration, Oxid. Met. 87 (2017) 757–766. https://doi.org/10.1007/s11085-017-9749-x.

[30] ASTM G1-03(2017)e1 Standard Practice for Preparing, Cleaning, and Evaluating Corrosion Test Specimens, ASTM International, 2017. http://www.astm.org/cgi-bin/resolver.cgi?G1-90(1999)e1.

[31] D.A. Jones, Effects of Metallurgical Structure on Corrosion - 10.1 Hydrogen Damage, in: Princ. Prev. Corros., 2nd ed., Prentice Hall, United States of America, 1996: pp. 334–343.

[32] E. Ramirez, J.G. Gonzalez-Rodriguez, A. Torres-Islas, S. Serna, B. Campillo, G. Dominguez-Patino, J.A. Juarez-Islas, Effect of microstructure on the sulphide stress cracking susceptibility of a high strength pipeline steel, Corros. Sci. 50 (2008) 3534–3541. https://doi.org/10.1016/j.corsci.2008.09.014.

[33] D.A. Jones, Corrosive-Related Damage by Hydrogen, Erosion, and Wear, in: Princ. Prev. Corros., 2nd ed., Prentice Hall, United States of America, 1996: pp. 334–341.

[34] NACE International, NACE MR0175/ISO 15156, NACE, Houston, Tex., 2009.

[35] M. Iannuzzi, 15 - Environmentally assisted cracking (EAC) in oil and gas production, in: V.S. Raja, T. Shoji (Eds.), Stress Corros. Crack., Woodhead Publishing, 2011: pp. 570–607. https://doi.org/10.1533/9780857093769.4.570.

[36] J. Davidson, Hydrogen-induced cracking of low carbon - Low alloy steel weldments, Mater. FORUM. 19 (1995) 35–51.

[37] K.-S. Kim, J.-H. Kang, S.-J. Kim, Effect of Grain Boundary Carbide on Hydrogen Embrittlement in Stable Austenitic Stainless Steels, ISIJ Int. 59 (2019) 1136–1144. https://doi.org/10.2355/isijinternational.ISIJINT-2018-639.

[38] K.-S. Kim, J.-H. Kang, S.-J. Kim, Nitrogen effect on hydrogen diffusivity and hydrogen embrittlement behavior in austenitic stainless steels, Scr. Mater. 184 (2020) 70–73. https://doi.org/10.1016/j.scriptamat.2020.03.038.

[39] M.L. Martin, M. Dadfarnia, S. Orwig, D. Moore, P. Sofronis, A microstructure-based mechanism of cracking in high temperature hydrogen attack, Acta Mater. 140 (2017) 300–304. https://doi.org/10.1016/j.actamat.2017.08.051.

[40] P. Rhodes, Environment-assisted cracking of corrosion-resistant alloys in oil and gas production environments: A review, CORROSION. 57 (2001) 923–966. https://doi.org/10.5006/1.3290320.

[41] A. Traidia, E. Chatzidouros, M. Jouiad, Review of hydrogen-assisted cracking models for application to service lifetime prediction and challenges in the oil and gas industry, Corros. Rev. 36 (2018) 323–347. https://doi.org/10.1515/corrrev-2017-0079.

[42] M.H. Bartz, C.E. Rawlins, Effects of Hydrogen Generated by Corrosion of Steel, in: Annu. Meet. NACE, NACE International, St. Lois, 1948.

[43] S. Gao, B. Brown, D. Young, M. Singer, Formation of iron oxide and iron sulfide at high temperature and their effects on corrosion, Corros. Sci. 135 (2018) 167–176. https://doi.org/10.1016/j.corsci.2018.02.045.

[44] F. Pessu, R. Barker, F. Chang, T. Chen, A. Neville, Iron sulphide formation and interaction with corrosion inhibitor in H2S-containing environments, J. Pet. Sci. Eng. 207 (2021). https://doi.org/10.1016/j.petrol.2021.109152.

[45] S. Soylemezoglu, R. Harper, Oxygen ingress into geothermal steam and its effect on corrosion of low carbon steel at Broadlands, New Zealand, Geothermics. 11 (1982) 31–42. https://doi.org/10.1016/0375-6505(82)90005-0.

[46] E. Dayalan, G. Vani, J.R. Shadley, S.A. Shirazi, E.F. Rybicki, Modelling CO2 Corrosion of Carbon Steel in Pipe Flow, in: NACE Int. Annu. Conf. Corros. Show, NACE International, Orlando, FL, USA, 1995: p. Paper #118.

[47] A. Ikeda, M. Ueda, S. Mukai, Incluence of Environmental Factors on Corrosion in CO2 Source Well, in: Corros. Symp. Corros. CO2 Oil Gas Ind., NACE International, New Orleans, LA, USA, 1984.

[48] M.A. Islam, Z.N. Farhat, Characterization of the Corrosion Layer on Pipeline Steel in Sweet Environment, J. Mater. Eng. Perform. 24 (2015) 3142–3158. https://doi.org/10.1007/s11665-015-1564-4.

[49] L.G. Gray, B.G. Anderson, M.J. Danysh, P.R. Tremaine, Mechanisms of carbon steel corrosion in brines containing dissolved carbon dioxide at pH 4, Corros. Pap. (1989) 1–18.

[50] S. Nesic, Key issues related to modelling of internal corrosion of oil and gas pipelines - A review, Corros. Sci. 49 (2007) 4308–4338. https://doi.org/10.1016/j.corsci.2007.06.006.

[51] D.A. Jones, Environmentally Induced Cracking, in: Princ. Prev. Corros., 2nd ed., Prentice Hall, United States of America, 1996: pp. 236–244.

[52] S. Wu, H. Chen, H.L. Ramandi, P.C. Hagan, A. Crosky, S. Saydam, Effects of environmental factors on stress corrosion cracking of cold-drawn high-carbon steel wires, Corros. Sci. 132 (2018) 234–243. https://doi.org/10.1016/j.corsci.2017.12.014.

[53] W. Qi, Q. Gao, Y. Zhao, T. Zhang, F. Wang, Insight into the stress corrosion cracking of HP-13Cr stainless steel in the aggressive geothermal environment, Corros. Sci. 190 (2021). https://doi.org/10.1016/j.corsci.2021.109699.

[54] L. Wu, Y. Takeda, H. Morita, T. Shoji, A Comparison of Stress Corrosion Cracking Susceptibility of Steam Turbine Blade Materials for Geothermal Plants, CORROSION. 73 (2017) 125–137. https://doi.org/10.5006/2058.

[55] S.N. Karlsdottir, S.M. Hjaltason, K.R. Ragnarsdottir, Corrosion behavior of materials in hydrogen sulfide abatement system at Hellisheioi geothermal power plant, GEOTHERMICS. 70 (2017) 222–229. https://doi.org/10.1016/j.geothermics.2017.06.010.

[56] R. Bassler, A. Keserovi, J. Sobetzki, H.S. Klapper, MATERIALS EVALUATION FOR GEOTHERMAL APPLICATIONS, J. Teknol. 75 (2015) 7–14.

[57] M. Cabrini, S. Lorenzi, T. Pastore, M. Favilla, R. Perini, B. Tarquini, Materials selection for dew-point corrosion in geothermal fluids containing acid chloride, GEOTHERMICS. 69 (2017) 139–144. https://doi.org/10.1016/j.geothermics.2017.05.010.

[58] W. Faes, S. Lecompte, J. Van Bael, R. Salenbien, R. Baessler, I. Bellemans, P. Cools, N. De Geyter, R. Morent, K. Verbeken, M. De Paepe, Corrosion behaviour of different steel types in artificial geothermal fluids, GEOTHERMICS. 82 (2019) 182–189. https://doi.org/10.1016/j.geothermics.2019.05.018.

[59] U. Ince, M. Toksoy, M. Guden, Testing corrosion rates on steel piping in geothermal district heating, Mater. Perform. 47 (2008) 56–59.

[60] W. Zhang, B. Brown, D. Young, G. Bota, S. Nesic, M. Singer, Pitting mechanism of mild steel in marginally sour environments—Part I: A parametric study based on formation of protective layers, Corros. Sci. 183 (2021) 109305. https://doi.org/10.1016/j.corsci.2021.109305.

[61] W. Zhang, B. Brown, D. Young, M. Singer, Pitting mechanism of mild steel in marginally sour environments – Part II: Pit initiation based on the oxidation of the chemisorbed iron sulfide layers, Corros. Sci. 184 (2021) 109337. https://doi.org/10.1016/j.corsci.2021.109337.

[62] D.A. Jones, Effects of Metallurgical Structure on Corrosion - 9.5 De-alloying, in: Princ. Prev. Corros., 2nd ed., Prentice Hall, United States of America, 1996: pp. 323–331.

[63] D.A. Jones, Effects of Metallurgical Structure on Corrosion - 9.1 Intergranular Corrosion of Austenitic Steels, in: Princ. Prev. Corros., 2nd ed., Prentice Hall, United States of America, 1996: pp. 292–304.

[64] E. Heitz, Mechanistically based prevention strategies of flow-induced corrosion, ELECTROCHIMICA ACTA. 41 (1996) 503–509. https://doi.org/10.1016/0013-4686(95)00336-3.

[65] D.A. Jones, Corrosion-Related Damage by Hydrogen, Erosion and Wear - 10.2 Erosion-Corrosion, in: Princ. Prev. Corros., 2nd ed., Prentice Hall, United States of America, 1996: pp. 343–347.

[66] S.N. Karlsdottir, K.R. Ragnarsdottir, A. Moller, I.O. Thorbjornsson, A. Einarsson, On-site erosion-corrosion testing in superheated geothermal steam, GEOTHERMICS. 51 (2014) 170–181. https://doi.org/10.1016/j.geothermics.2014.01.007.

[67] F. Brownlie, T. Hodgkiess, A. Pearson, A.M. Galloway, A study on the erosion-corrosion behaviour of engineering materials used in the geothermal industry, WEAR. 477 (2021). https://doi.org/10.1016/j.wear.2021.203821.

[68] D.A. Jones, Galvanic and Concentrated Cell Corrosion, in: Princ. Prev. Corros., 2nd ed., Prentice Hall, United States of America, 1996: pp. 168–199.

[69] S.N. Esmaeely, G. Bota, B. Brown, S. Nesic, Influence of Pyrrhotite on the Corrosion of Mild Steel, CORROSION. 74 (2018) 37–49. https://doi.org/10.5006/2505.

[70] S.N. Esmaeely, S. Nesic, Reduction Reactions on Iron Sulfides in Aqueous Acidic Solutions, J. Electrochem. Soc. 164 (2017) C664–C670. https://doi.org/10.1149/2.1381712jes.

[71] S.N. Esmaeely, S. Nesic, Localized Corrosion of Mild Steel in H2S Containing Aqueous Environments-Case Studies and Common Mechanisms, CORROSION. 75 (2019) 938–945. https://doi.org/10.5006/3164.

[72] H.H. Strehblow, P. Marcus, Fundamentals of Corrosion, in: Corros. Mech. Theory Pract., 3rd ed., CRC Press, 2017: pp. 3–12.

[73] Y. Kawahara, High temperature corrosion mechanisms and effect of alloying elements for materials used in waste incineration environment, Corros. Sci. 44 (2002) 223–245. https://doi.org/10.1016/S0010-938X(01)00058-0.

[74] M. Schütze, High-Temperature Corrosion, in: Corros. Mech. Theory Pract., 3rd ed., CRC Press, 2012: p. 573.

[75] M. Schütze, High-Temperature Corrosion, in: Corros. Mech. Theory Pract., 3rd ed., CRC Press, 2017: pp. 573–584.

[76] E. Barbier, Geothermal energy technology and current status: an overview, Renew. Sustain. ENERGY Rev. 6 (2002) 3–65. https://doi.org/10.1016/S1364-0321(02)00002-3.

[77] K.A. Licthi, S. Soylemezoglu, K.D. Cuncliffe, Geotherrmal corrosion and corrosion products., in: 1981: pp. 103–108.

[78] C. Miranda-Herrera, I. Sauceda, J. Gonzalez-Sanchez, N. Acuna, Corrosion degradation of pipeline carbon steels subjected to geothermal plant conditions, ANTI-Corros. METHODS Mater. 57 (2010) 167–172. https://doi.org/10.1108/00035591011058165.

[79] M. Finster, C. Clark, J. Schroeder, L. Martino, Geothermal produced fluids: Characteristics, treatment technologies, and management options, Renew. Sustain. ENERGY Rev. 50 (2015) 952–966. https://doi.org/10.1016/j.rser.2015.05.059.

[80] J.A. Acuna, B. Arcedera, Two-Phase Flow Behavior and Spinner Data Analysis in Geothermal Wells, in: Thirtieth Workshop Geotherm. Reserv. Eng., Stanford, California, 2005.

[81] M. Kruszewski, V. Wittig, Review of failure modes in supercritical geothermal drilling projects, Geotherm. ENERGY. 6 (2018). https://doi.org/10.1186/s40517-018-0113-4.

[82] A. Hansell, C. Oppenheimer, Health hazards from volcanic gases: A systematic literature review, Arch. Environ. Health. 59 (2004) 628–639. https://doi.org/10.1080/00039890409602947.

[83] S. Arnorsson, J.Ö. Bjarnason, N. Giroud, A. Stefansson, Sampling and analysis of geothermal fluids, in: Geofluids, Wiley, 2006: pp. 203–216. https://onlinelibrary.wiley.com/doi/full/10.1111/j.1468-8123.2006.00147.x.

[84] S. Arnorsson, Isotopic and chemical techniques in geothermal exploration, development and use: sampling methods, data handling, interpretation, Int. At. Energy Agency. (2000) 108–113.

[85] Procedures for the Measurement of Carryover of Boiler Water into Steam, (2008). http://www.iapws.org/techguide/Carryover.pdf (accessed November 28, 2021).

[86] G. Petzow, Metallographic Etching, in: Metallogr. Etch., American Society for Metals, Ohio, USA, 1978: p. 87.

[87] G. Petzow, Metallographic Etching, in: Metallogr. Etch., American Society for Metals, Ohio, USA, 1978: p. 64.

[88] G.F. Vander Voort, J.W. Bowman, R.B. Frank, Microstructural characterization of custom age 625 plus alloy, in: Miner. Met. Mater. Soc., 1994: pp. 489–498. https://www.researchgate.net/publication/269258305_Microstructural_Characterization_of_Custom_Age_625_Plus_Alloy.

[89] H. Jia, H. Qian, W. Qu, L. Zheng, W. Feng, W. Ren, Fluoride Occurrence and Human Health Risk in Drinking Water Wells from Southern Edge of Chinese Loess

Plateau, Int. J. Environ. Res. Public. Health. 16 (2019). https://doi.org/10.3390/ijerph16101683.

[90] M. Meldrum, Toxicology of hydrogen fluoride in relation to major accident hazards, Regul. Toxicol. Pharmacol. 30 (1999) 110–116. https://doi.org/10.1006/rtph.1999.1342.

[91] REVIEW OF LOW-TEMPERATURE OXIDATION OF CARBON STEELS AND LOW-ALLOY STEELS FOR USE AS HIGH-LEVEL RADIOACTIVE WASTE PACKAGE MATERIALS, (2007). https://www.nrc.gov/docs/ML0402/ML040200112.pdf (accessed November 28, 2021).

Papers as Published

Journal Article 1

A.I. Thorhallsson, A. Stefansson, D. Kovalov, S.N. Karlsdottir, Corrosion testing of materials in simulated superheated geothermal environment, Corros. Sci. 168 (2020) 108584. https://doi.org/10.1016/j.corsci.2020.108584.

A.I. Thorhallsson, A. Stefansson, D. Kovalov, S.N. Karlsdottir, Corrigendum to "Corrosion testing of materials in simulated superheated geothermal environment" [Corros. Sci. 168 (2020) 10], Corros. Sci. 174 (2020) 108807. https://doi.org/10.1016/j.corsci.2020.108807.

Corrosion Science 168 (2020) 108584

Contents lists available at ScienceDirect

Corrosion Science

journal homepage: www.elsevier.com/locate/corsci

Corrosion testing of materials in simulated superheated geothermal environment

Andri Isak Thorhallsson[a,*], Andri Stefansson[b], Danyil Kovalov[a], Sigrun Nanna Karlsdottir[a]

[a] Faculty of Mechanical Eng., Industrial Eng. and Computer Science, University of Iceland, Hjardarhagi 2-6, 107 Reykjavik, Iceland
[b] Institute of Earth Sciences, University of Iceland, Sturlugata 7, 101 Reykjavik, Iceland

ARTICLE INFO

Keywords:
Carbon steel
Superalloys
SEM
XRD
Acid corrosion
High temperature corrosion

ABSTRACT

This paper reports the results of corrosion study for carbon steel, austenitic stainless steel, as well as titanium and nickel-based alloys which were tested in a simulated superheated geothermal environment (SSGE) in flow-through reactors to investigate the corrosion behaviour to aid in the future material selection for high temperature deep geothermal application. The testing fluid was superheated steam (T = 350 °C and P = 10 bars gauge) containing H_2S, CO_2 and HCl with condensate of pH = 3. The corrosion rate for all samples was negligible but carbon steel was prone to localized damage under a magnetite film with a sulphur rich sublayer.

1. Introduction

Geothermal fluids formed in the upper part of the Earth's crust associated with active volcanism have been utilized for energy production worldwide. Conventional exploitation of geothermal fluids from such systems typically produces an average of ~3–5 MW electric power per well [1]. The reservoir fluid temperatures of such geothermal systems are typically 230 − 350 °C. However, geothermal fields where temperatures exceed the critical temperature of water have also been reported for several fields in Iceland, Kenya, Italy, USA, Japan and Mexico [2]. Utilization of such fluids has been predicted to increase power production per well of up to ~30 − 50 MW [3]. Utilizing geothermal energy from geothermal wells is important in the renewable energy mixture and drilling deeper geothermal wells can, therefore, potentially increase the power production from each well. At the beginning of the 21st century, a scientific program called the Iceland Deep Drilling Project was founded. The aim of the project was to drill 3.5–5 km deep wells in three geothermal fields in Iceland and extract 450 − 600 °C supercritical fluid to make the geothermal energy output much higher and the operation per well more economical [3]. Supercritical water is where temperatures and pressures are above the critical point of 221.2 bars and 375.15 °C but the supercritical point of H_2O shifts when dissolved components are present in the fluid [4]. For pure water, if enthalpy is higher than the critical enthalpy of 2086 J/g, the steam exists in single phase supercritical condition. Experience from the first deep drilled well of the IDDP, IDDP-1, revealed that the energy output of deep geothermal wells can be an order of magnitude higher than from a regular high temperature well [5]. The temperature in the IDDP-1 well in Iceland was 450 °C and 140 bars at the wellhead. Gas samples from the steam in IDDP-1 were collected during the discharge of the well and average concentrations recorded for some corrosive species were H_2S = 339 mg/kg, CO_2 = 732 mg/kg, H_2 = 10 mg/kg, Cl = 93 mg/kg, F = 5 mg/kg, NH_3 = 0.14 mg/kg. Other chemical species in the steam were Fe = 8.4 mg/kg, B = 1 mg/kg and the pH of the condensed steam was 2.62 [6]. Due to the high temperature and high pressure conditions met in the IDDP-1 well and future plans for drilling more deep drilling wells, corrosion tests were conducted at the wellhead during the discharge of the IDDP-1 well to gain a better understanding of the corrosion behaviour of materials in high temperature deep geothermal environment. Extensive corrosion testing was conducted in-situ during the discharge of the IDDP-1 well [7–10]. From these corrosion studies, corrosion coupon testing [7] conducted at the wellhead is probably the most significant in-situ study made so far in deep geothermal superheated systems and most relevant for this research. In the in-situ corrosion coupon testing, several alloys (including carbon steel, austenitic stainless steel, duplex steel, nickel-based and titanium alloys) were tested in a pipe connected to the wellhead for a total of 113 days at 350 − 360 °C and 12 − 13 bars pressure. Due to the pressure drop used in the test pipe during testing, amorphous silica supersaturated in the steam and formed heavy silica scaling on the test samples [7]. All the samples in the in-situ coupon test had low corrosion rates, well below 0.01 mm/year where low carbon steel S235JRG2 and nickel-based alloy UNS N06625 had corrosion rates of 0.004 mm/year and 0.001 mm/year respectively [7]. Even though corrosion rates were

* Corresponding author.
E-mail address: ath196@hi.is (A.I. Thorhallsson).

https://doi.org/10.1016/j.corsci.2020.108584
Received 14 October 2019; Received in revised form 2 March 2020; Accepted 3 March 2020
Available online 05 March 2020

low in the in-situ testing, localized corrosion damage was found in all the tested samples. Furthermore, the localized damage was observed under the silica scale and questions arose whether the silica scaling was catalysing corrosion in the samples tested. From the overall corrosion coupon testing in the first deep geothermal well in Iceland, it was concluded that silica scale covering the samples provided protection against general corrosion but possibly promoted localized corrosion under the silica deposits [7]. The corrosive species in the superheated geothermal steam mentioned previously [6] included; CO_2, H_2S, HCl, HF and H_2. It has to be noted here that there were no conclusions on the corrosion effect or contribution of each corrosive species to the localized corrosion of the alloys investigated after the in-situ testing. Eventually, the IDDP-1 well was quenched and closed in 2012 due to operational problems resulting from corrosion in valves [11].

Only a few studies have reported corrosion data in superheated geothermal systems other than the corrosion testing conducted during the discharge of the IDDP-1 well [7–10]. In 1980, corrosion testing was done in well KG-12 in Krafla, Iceland at 7 bars gauge in a 220 °C superheated geothermal fluid containing HCl. All of the alloys, including carbon steel, stainless steel and nickel-based alloys were prone to localized damage except the austenitic stainless-steel UNS S31254 and the nickel-based alloy UNS N06255. The corrosion rate for the carbon steel was approximately 0.3 mm/year in the superheated steam [12] which was an order of magnitude higher than the corrosion rate observed in the in-site testing in IDDP-1 well mentioned above [7]. Due to the high corrosion rate of carbon steel in KG-12 and small superheat of the steam, condensation of the geothermal fluid in the testing pipe was considered to have occurred during the testing in well KG-12. In 2010, down-hole corrosion testing was done for alloys in an acidic, high temperature geothermal well KJ-39 in Krafla Iceland. The temperature was around 293 °C at the wellhead but around 350 °C at the bottom with a pressure range from 13 bar to 20 bar. The pH of the condensate sampled at the wellhead was measured as 4.1. The geothermal fluid contained CO_2, H_2S, HCl, H_2 as well as CH_4 and SO_4. The results of the corrosion testing showed pitting in the carbon steels, the stainless-steel and the nickel-based alloys tested. The corrosion rate reported was very high for the carbon steel and martensitic stainless steel but very low for austenitic stainless steel and the nickel-based alloys or below 0.1 mm/year. From the data gathered and experience in the operation of the KJ-39 well, it was concluded that superheated geothermal fluid from the bottom of well mixed with colder geothermal fluid flowing into the well at lower depth resulting in severe corrosion of the well liner at 1600 m depth [13]. This resulted in acidic conditions in the mixing zone which produced low pH fluid to be in contact with the testing samples in the sour well. The electrochemical study by Bogaerts et al. [14] on stainless steels and nickel-based alloys in relevant environment (chloride rich with some anions) but in aqueous solutions up to 300 °C and 120 bars implies that pitting potential of all the alloys is at a minimum between 150 − 200 °C [14]. These results indicate a link between corrosion behaviour and temperature is not straightforward.

From the studies and diverse results mentioned above, it can be concluded that corrosion behaviour of materials in high temperature, superheated and supercritical geothermal environment has not yet been fully understood. Testing material in-situ in superheated geothermal fluid has not been possible since 2012 or when the first Iceland deep drilling well was quenched and closed. Thus, there is lacking a platform to study the corrosion behaviour of potential candidates of deep geothermal wells, which is crucial for the design of such future wells.

The objective of this work was to study the corrosion behaviour of materials in a simulated superheated geothermal environment at a stable, controlled condition. A testing facility of flow-through reactors was established with a purpose to simulate geothermal high temperature environment that can be encountered in deep geothermal wells. In this paper, we report on the simulated testing done for carbon steel, austenitic stainless-steels, nickel-based alloys and titanium alloy in sequential flow-through reactors containing superheated steam of 350 °C and at 10 bar gauge containing CO_2, H_2S and HCl as the corrosive species. The aim of the paper was to 1) establish laboratory testing facility that can accommodate testing samples in a superheated steam containing H_2S, CO_2 and HCl from a laboratory-made solution and 2) perform corrosion experiments to understand the corrosion behaviour of carbon steel, austenitic stainless steel, nickel-based alloys and titanium alloy in a controlled simulated superheated geothermal environment.

2. Experimental

2.1. Flow-through reactors testing facility and condition

One of the objectives of this study was to design flow-through reactors testing facility with controlled testing parameters to be able to perform corrosion testing in superheated laboratory prepared fluid that has similar properties as geothermal fluid from a field. Pre-testing trials were done to adjust and optimize the testing conditions, including change in design, flow, insulation and external heating, etc. In the first steps of developing the testing equipment, low grade stainless-steel samples were used for assessing the uniformity in the test conditions. For the 1st generation of the test setup, the design of equipment and set testing parameters resulted in inhomogeneous conditions in the reactors i.e. boiling and condensation of the fluid at inlet and outlet, respectively, in the test volume [15]. Based on the unsatisfactory experimental conditions stated above, additional adjustments of the laboratory equipment and parameters were done. Subsequent to these adjustments, nickel-based alloy samples were tested in the next testing batch, but some localized nickel sulphide deposits were observed on part of the samples indicating non-uniform conditions in the reactor [16]. The non-uniform conditions occurred probably due to cooling effects at inlet and outlet to the reactors and due to transportation of liquid solution due to flashing of liquid from preheater to the reactors when pumps primed during the first pretesting. Further adjustments of the equipment and tuning of process parameters led to homogeneous corrosion behaviour and consistent corrosion rate between all the tested samples within the two reactors indicating more uniform conditions in the reactor volume. To confirm the superheated state of the testing fluid, resistor temperature detector (RTD) with platinum detector was connected between the preheater and the first reactor; between the two reactors and at the outlet of the second reactor. In this paper, the results for testing using the fully developed laboratory facility are reported. Fig. 1 shows a photo of the corrosion testing equipment and Fig. 2 shows the corresponding flow diagram of the flow-through loop equipment.

Two combinations of H_2S and CO_2 concentrations were used in the testing; a lower concentration of H_2S = 30 ppm and CO_2 = 80 ppm, and a higher concentration of H_2S = 150 ppm and CO_2 = 250 ppm. Two solutions were mixed to obtain the H_2S and CO_2 gases for simulating a geothermal steam environment in the tests. The setup and operation of the testing facility can be outlined as follows: two reactant solutions were pumped from two volumetric flasks using Chrom Tech series I pumps. The solutions were degassed by Labhut degassers and then mixed before entering the preheater. The tubing at the inlet of the flow-through loop, from mixing to the inlet of the preheater is made of stainless UNS S31603. The material in the flow-through loop in the hot temperature part of the flow line i.e. in the preheater, the reactors and tubing between the preheater and reactor, a tubing between reactors and tubing between second reactor and pipe at outlet towards condenser was made of corrosion resistant alloy UNS N10276. The sample holder and fasteners were made of Inconel UNS N06625 and UNS S31603 materials of which were used depending on the alloy type of the sample in the testing batch. Washers between samples and fasteners are made of ceramic alumina provided by Ortech. The hot temperature part of the flow-through loop was highly insulated with ceramic material ($SiO_2/Al_2O_3/MgO$) and glass wool to minimize heat loss. The preheater,

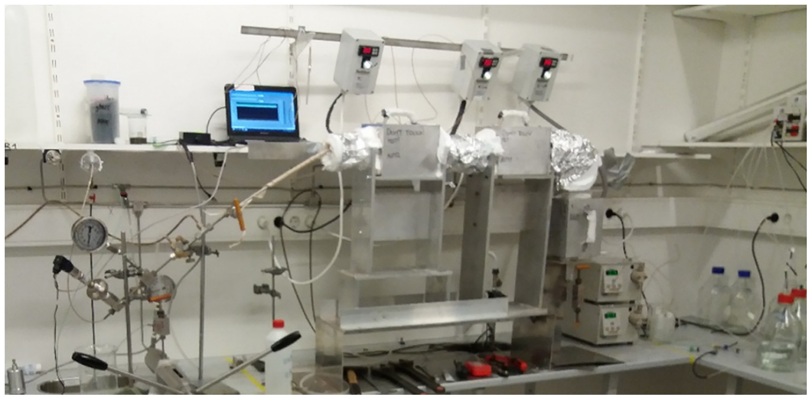

Fig. 1. Corrosion testing equipment setup.

reactors, and heating units were custom made. The temperature of the reactors was regulated by a temperature controller and elements from Rafhitun. Thermocouples used in the system were connected to the reactor pipes externally. Another set of thermocouples were connected to the reactor pipes externally to the Labjack U6 series data logger. All thermocouples connected to the heating units are K-type. Stainless steel and nickel-based alloy tubing, fittings and condenser were provided by SITEC. The piping at the outlet of the second reactor was wrapped with HTS Amptek heating tape. Analog pressure meter was connected to the flow line after the condenser. Digital pressure transducer, WIKA model S-20, was connected to the Labjack U6 datalogger to monitor the pressure in the flow-through loop system. The back pressure regulator (BPR) was designed and custom made by Prologo to set and control fluid pressure in the system. The external pressure controller exerting on the BPR was a SITEC 750 hand pump.

The initial plan was to run a 21-day testing period for all the testing batches at low and high concentration. At a higher concentration of H_2S and CO_2, deposits accumulated at the condensing part of the experiment that led to a slow build-up of pressure inside the system, after approximately two weeks of testing. As a result, the testing period at higher concentration was decided to be limited to 10 days. Testing periods and main parameters for all the materials tested are shown in Table 1.

Before each run of the test batches, the process volume was flushed with deionized water at room temperature for 24 h to remove air in the system. The system volume was then heated up to 350 °C at 10 bars with pure steam to stabilize the system before the testing fluid was injected into the flow-through loop. At the end of each testing batch experiment, testing fluid was flushed with pure steam before the preheater and reactor temperature was lowered to ambient temperature. This procedure was done to prevent acidic condensation in the reactor volume during shut down of experiment. The stability of pressure within the system was ± 0.5 bar and stability of preheater and reactors was ± 2 °C.

2.2. Testing fluid

The testing fluid was a mixture of two aqueous solutions, whereas the first solution contained HCl while the second solution contained anhydrous Na_2S and $NaHCO_3$. Anhydrous Na_2S and $NaHCO_3$ were weighted in deionized water solution to get the target concentrations of H_2S and CO_2 in the final corrosion testing solution. The chemical reactions between Na_2S and HCl, and $NaHCO_3$ and HCl when the reactant solutions were mixed were as follows:

$$Na_2S + 2HCl = H_2S + 2NaCl \quad (1)$$

$$NaHCO_3 + HCl = CO_2 + H_2O + NaCl \quad (2)$$

The sulphide [S^{2-}], hence the H_2S, and CO_2 concentration in the reactant solutions were verified and titrated after preparation of the reactant solutions. To determine S^{2-} concentration in the Na_2S/$NaHCO_3$ reactant solution, 5 ml of acetone and 5 ml of 5 M NaOH were mixed into mixing flask. A 0.2 ml of the Na_2S/$NaHCO_3$ solution was

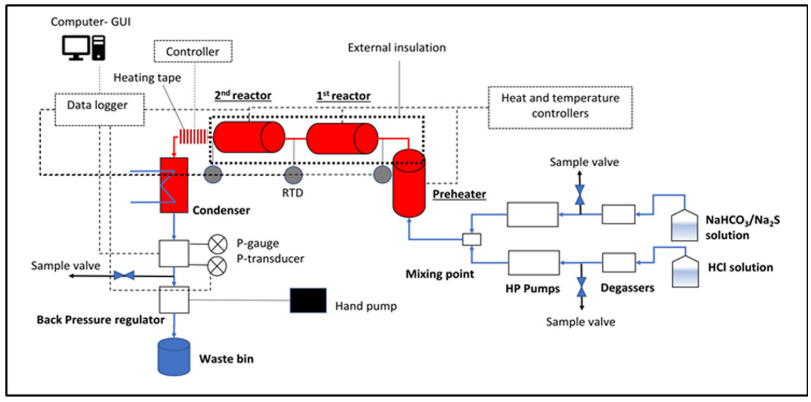

Fig. 2. Corrosion testing flow diagram.

Table 1
Materials tested and main parameters in test batches.

Test batch no.	Material type	Alloy	Test period [Days]	Inlet volumetric flow [ml/min]	Fluid gauge pressure [bar]	Fluid temperature [°C]	H_2S [mg/kg]	CO_2 [mg/kg]
1	Ni-based alloys	UNS N06255	21	0.3	10	350	30	80
2[a]		UNS N06845	16	0.3	10	350	30	80
3		UNS N06625	21	0.3	10	350	30	80
4	Carbon steel	S235JRG2	10	0.3	10	350	150	250
5	Aust. St. steel	UNS S31254	10	0.3	10	350	150	250
6		UNS S31277	10	0.3	10	350	150	250
7	Ni-based alloys	UNS N06625	10	0.3	10	350	150	250
8		UNS N06845	10	0.3	10	350	150	250
9	Ti-based alloy	Ti-4Al-4Mo-2Sn	10	0.3	10	350	150	250

[a] Stopped at 16th day due to leakage at fitting.

added to the mixing flask with a precise and calibrated micropipette. Afterwards, 40 ml of deionized water was poured into the Erlenmeyer flask and then trace amount of dithizone crystals was added to the total solution until turned pale yellow. The total solution in the Erlenmeyer flask was then titrated with 0.001 M Hg-acetate solution until the colour of the total solution changed to pale pink, indicating that all sulphide ions were reacted with mercury ions. When mercury acetate is used to titrate the sulphur ions, where mercury cations react with the sulphur anions in the solution according to

$$Hg^{2+} + S^{2-} -> HgS \quad (3)$$

When all the sulphur anions S^{2-} have reacted in the solution, the mercury cations start to react with dithizone ($C_{13}H_{12}N_4S$) and the colour of solution changes to pink [17]. To determine the concentration of the CO_2 in the solution, the equilibrium of CO_2 with carbonic acid, bicarbonate and carbonate was considered [18,19] according to equilibrium in:

$$CO_2 + H_2O = H_2CO_3 \quad (4)$$

$$H_2CO_3 = HCO_3^- + H^+ \quad (5)$$

$$HCO_3^- = CO_3^{2-} + H^+ \quad (6)$$

The carbonic acid is a weak acid, hence the left side of reaction (4) is dominant at low pH (< 4.5). Furthermore, the dissolved CO_2 in the solution is volatile at low pH with a tendency to degas from the solution. To determine the CO_2 concentration in the $Na_2S/NaHCO_3$ reactant solution, a known volume of the reactant solution was titrated with Metrohm 765 Dosimat (with Metrohm 780 pH meter calibrated with standardized pH = 4.00 and 7.00 solutions) until the solution pH was 8.3 with 0.1 M HCl solution. Subsequently, the solution was further titrated with 0.1 M HCl until pH = 4.5. The solution was then degassed for at least 15 min with bubbling inert N_2 gas until CO_2 and H_2S were eliminated from the solution. The solution was set again to pH = 4.5 with the 0.1 M HCl. The solution was then back titrated with 0.1 M NaOH solution until pH = 8.3. From the amount of HCl and NaOH used in titration and back-titration and from the known concentration of H_2S in the solution, the CO_2 could be determined (Table 2).

During corrosion tests, the flow rate and pH of the fluid condensate at the outlet were regularly measured as well as the titration of H_2S and CO_2 of the fluid were done at the outlet. In order to conduct the titration of the outlet fluid, H_2S and CO_2 gases were to be extracted with 0.1 M NaOH solution to avoid the escape of the gases from the fluid. The waste fluid was eventually accumulated in a waste bin containing the solution of NaOH with Zn-acetate to neutralize the H_2S gas.

The chemical composition of the testing fluid for simulating high temperature geothermal fluid with two different concentration of H_2S and CO_2 is given in Table 3. A comparison of the physical and chemical properties of the two testing fluids in the simulated testing to IDDP-1 fluid is also shown in Table 3. The testing in simulated geothermal environment were done at two different concentrations of H_2S and CO_2 in laboratory; low concentration (H_2S = 30 mg/kg and CO_2 = 80 mg/kg) and high concentration ((H_2S = 150 mg/kg and CO_2 = 250 mg/kg).

Table 2
Number of moles of the chemical species and total volume of the reactant solutions at low and high concentration of H_2S and CO_2 in the mixed solution.

Parameter	Simulated testing - low concentration	Simulated testing - high concentration	Unit
Reactant solution no. 1			
HCl	9.2	31	mmol
Total volume	1000	1000	ml
Reactant solution no. 2			
Na_2S	1.8	8.8	mmol
$NaHCO_3$	3.6	11.4	mmol
Total volume	1000	1000	ml

Table 3
Comparison between fluid properties in simulated testing vs. previous in-situ testing in Iceland Deep Geothermal Well no. 1 [9].

Parameter	Simulated testing - low concentration	Simulated testing - high concentration	In-situ testing IDDP-1	Unit
pH	3.0	3.0	2.62	
Temperature	350	350	350 – 360	°C
Fluid pressure	10	10	12 – 13	bar
Fluid velocity	0.012	0.012	2 – 5	m/s
Testing period	21[a]	10	113	Days
Cl	35.5[b]	35.5[b]	93	mg/kg
CO_2	80	250	732	mg/kg
H_2S	30	150	339	mg/kg
H_2	–	–	10	mg/kg
F	–	–	5	mg/kg

[a] UNS N06226 tested in 16 days.
[b] From pH = 3.

2.3. Testing materials

The types of materials tested included carbon steel (S235JRG2), two types of austenitic stainless-steels (UNS S31254 and S31277) and three nickel-based alloys (UNS N06255, N06625 and N06845) and one titanium alloy grade (Ti-4Al-4Mo-2Sn). Three flat coupon samples of each material were tested in each testing batch. Two of the coupons had dimensions 100 mm x 7 mm x 1 – 2 mm for weight loss analysis and one coupon for microstructural and chemical composition analysis of the cross-section had a dimension of 100 mm x 7 mm x 1 – 2 mm. The thickness of the coupons for each material depended on their availability from the producers. The nickel-based alloys were the only material tested in the low concentrations of H_2S and CO_2. Overview of the

Table 4
Chemical composition (main elements) of the alloys tested in the simulated corrosion testing.

Material	UNS number	Other designation	Nominal composition [% wt]												
			C	Si	Mn	Cr	Ni	Mo	Cu	Al	Nb	Ti	W	Sn	Fe
Carbon steel	N/A	NS-EN S235JRG2 (ASTM A 284C)	0.04	0.02	0.20	0.04	0.02	0.00	0.040	0.04	0.00	0.00			bal.
Austenitic stainless steel	S31254		0.02[a]	0.8[a]	1.0[a]	20.0	18.0	6.1	0.7						bal.
	S31277		0.02[a]	0.5[a]	3.0[a]	23[a]	28[a]	8[a]	1.5[a]						bal.
Nickel-based alloy	N06255		0.03[a]	1.0[a]	1.0[a]	26[a]	52[a]	9[a]	1.2[a]				3[a]		bal.
	N06845		0.05[a]	0.5[a]	0.5[a]	25[a]	50[a]	7[a]	4[a]				5[a]		bal.
	N06625		0.1[a]	0.5[a]	0.5[a]	23[a]	58.0[b]	10[a]		0.4[a]	4.15[a,c]	0.4[a]			5.0[a]
Titanium alloy	N/A	Ti-4Al-4Mo-2Sn		0.7[a]				5[a]		5[a]		bal.		2.5[a]	0.2[a]

[a] Maximum value.
[b] Minimum value.
[c] Nb + Ta.

materials and their chemical composition is given in Table 4.

2.4. Sample preparation and geometry

All the samples were ground to 600 grit with SiC abrasive paper before corrosion testing. The samples were then cleaned in ethanol and ultrasound bath and weighed and measured according to ASTM G1-90 before corrosion testing. The measured corrosion rate (CR) of the material tested in mm/year was calculated via the weight loss method and according to standard [20]:

$$CR = \frac{K \bullet W}{A \bullet t \bullet \rho} \quad (7)$$

Where K is the corrosion rate constant equal to $8.76 \cdot 10^4$ mm/year, W is the mass loss in grams of the tested material with a ± 0.00005 g precision, A is the exposed surface area in cm^2 of a tested sample, t is the exposure time in hours, and ρ is the material density in g/cm^3.

2.5. Post exposure measurements and analysis

For weight loss analysis, the samples were cleaned to remove corrosion products according to ASTM G1-90. It is to be noted here that there is no standard cleaning procedure available for Ti-based alloys due to extreme adhering titanium oxide film. Therefore, the Ti-based alloy in the experiment was only cleaned by ethanol in the ultrasonic bath after testing. For Scanning Electron Microscope (SEM), X-ray Electron Dispersive Spectroscope (XEDS) and grain boundary analysis, the samples applied for microstructural analysis were sectioned using a diamond wafering blade, mounted in thermosetting phenol formaldehyde resin (i.e., bakelite) and cast under pressure. The samples were ground to 1000 grit with SiC abrasive paper and polished with 3 µm and 1 µm diamond paste slurry and 0.02-0.06 µm particle size colloidal silica. The samples were analysed using SEM and XEDS before and after the corrosion testing. The SEM equipment used was a Zeiss Supra 25. The XEDS instrument used is Oxford Instruments with Si(Li) X-ray detector and INCA Energy 300 software. For grain boundary analysis, 2% nital [21] was used for etching of carbon steel S235JRG2. Kroll´s reagent [22] was used for etching of alloy Ti-4Al-4Mo-2Sn. Mixed acids [23] were used for etching of the nickel-based alloys and the austenitic stainless-steels. The grain boundary analysis was done using Meiji Techno´s MT7530OH optical microscope with Infinity Analyze software. The corrosion rate was determined via the weight loss method. The microstructure and corrosion forms of the samples were analysed using SEM. The chemical analysis was done by XEDS. The crystal structure of the materials was analysed in-situ by X-Ray Diffractometer (XRD) before and after corrosion tests with XPert Pro XRD meter from PANalytical with Data Collector software.

3. Results

3.1. Weight loss analysis

The weight loss method was applied to determine the corrosion rate of the tested samples. The corrosion rate for all the tested materials, at low and high concentration of H_2S and CO_2, was low, as shown in Fig. 3. The corrosion rates of nickel-based alloys tested in a low concentration of H_2S = 30 mg/kg and CO_2 = 80 mg/kg were in the order of 0.001 mm/year for all three nickel-based alloys tested. The corrosion rate of the nickel-based alloys UNS N06625 and N06845 in the higher concentration environment was comparable to the corrosion rate observed for the nickel-based alloys in the lower concentration testing. The corrosion rates of the austenitic stainless steels UNS S31254 and S31277 were higher than for the nickel-based alloys. No weight loss was measured for the titanium alloy Ti-4Al-4Mo-2Sn but negligible weight gain was observed with a negative corrosion rate value of -0.005 mm/year (presented as 0 mm/year in Fig. 3). The measured corrosion rate of the carbon steel S235JRG2 was low, 0.042 mm/year, but one to two orders of magnitude higher than the corrosion rate in comparison with the corrosion resistant alloys.

3.2. Microstructural and chemical analysis

3.2.1. Low Concentration, H_2S = 30 mg/kg and CO_2 = 80 mg/kg

Negligible corrosion film and no form of localized corrosion damage were observed in the nickel-based alloys in the SEM and XEDS analysis after tests at H_2S = 30 mg/kg and CO_2 = 80 mg/kg shown in Fig. 4. Titanium and niobium enriched nitrides were detected in blank and exposed samples of UNS N06625. A small amount of sulphur was detected at the surface on all the nickel-based alloys tested but were not easily detected in cross-section analysis as can be seen from the XEDS results in the table in Fig. 4.

3.2.2. Higher Concentration, H_2S = 150 mg/kg and CO_2 = 250 mg/kg

SEM images of the cross-sectional analysis of the austenitic stainless-steels are shown in Fig. 5 and for the nickel-based alloys and the titanium alloy in Figs. 6 and 7, respectively. Figs. 8 and 9 show SEM images of the cross-sectional and surface analysis of the carbon steel. Crystalline magnetite surface film formed on the surface of carbon steel after the corrosion testing as shown in Fig. 9. The XEDS analysis of the area shown in Fig. 10 indicates that this was likely magnetite crystals, Fe_3O_4, that have formed during the testing. The more corrosion resistant alloys i.e. the austenitic stainless-steels, nickel-based alloys and the titanium alloy were not susceptible to any localized corrosion damages in the simulated geothermal environment. No indication of pitting or cracking was observed in the austenitic stainless-steels, nickel-based alloys or the titanium-based alloy. In general, only small traces of sulphur were detected on the surface of the corrosion resistant alloys. The low carbon steel, however, had approximately 10 µm thick film

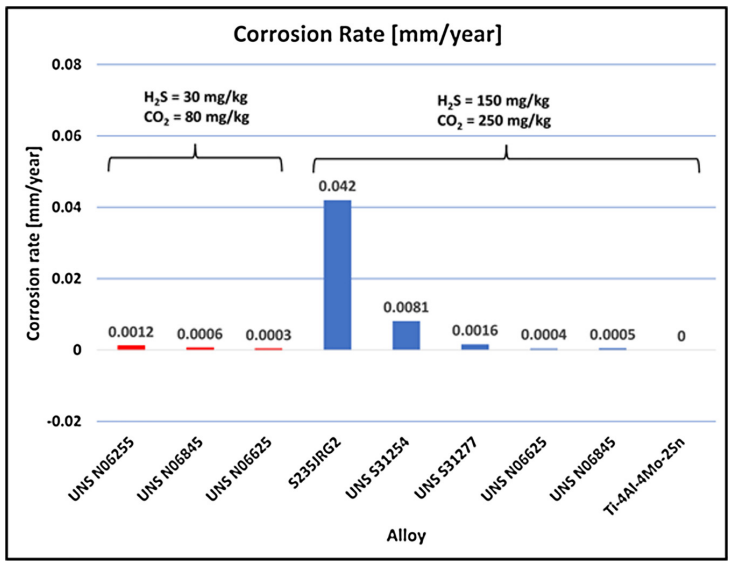

Fig. 3. Corrosion rate in low (H_2S = 30 mg/kg, CO_2 = 80 mg/kg) and high (H_2S = 150 mg/kg, CO_2 = 250 mg/kg).

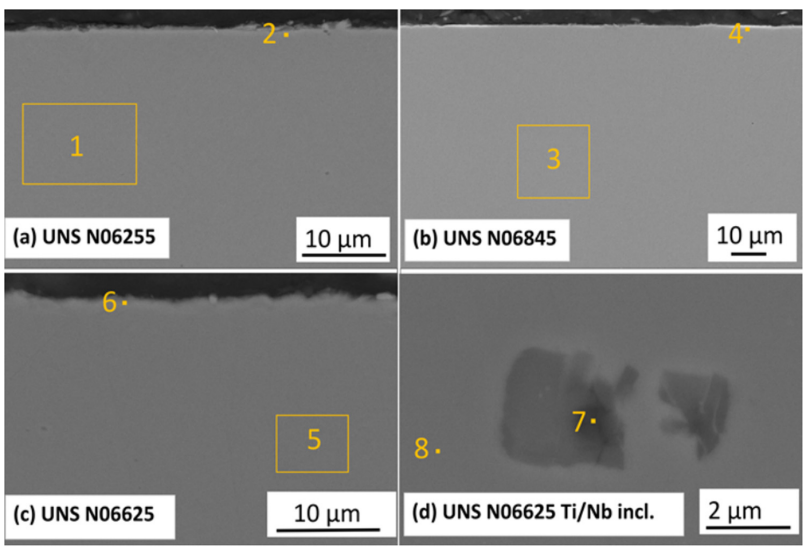

	Element														
Location	N	O	Mg	Al	S	Si	Ti	Cr	Mn	Fe	Ni	Nb	Cu	Mo	W
1	-	-	-	-	-	0.4	-	24.5	0.8	19.3	47.9	-	0.6	6.2	0.4
2	-	1.7	-	-	-	0.5	-	21.9	0.7	19.1	50.0	-	0.5	5.5	0.2
3	-	-	-	-	-	-	-	22.9	-	16.4	47.4	-	3.0	6.0	4.4
4	-	6.1	-	-	0.3	-	-	19.8	-	15.3	44.7	-	2.7	5.2	5.9
5	-	-	-	-	-	-	0.3	22.4	-	3.3	61.7	3.5	-	8.8	-
6	-	-	-	1.7	-	1.6	0.3	19.5	-	3.8	60.9	3.1	-	9.1	-
7	4.5	4.1	15.8	-	-	-	41.2	7.0	-	0.9	14.9	9.8	-	1.9	-
8	-	-	-	-	-	-	0.2	22.3	-	3.4	61.9	3.1	-	9.1	-

Fig. 4. SEM cross section images and XEDS analysis of testing materials in H_2S = 30 mg/kg and CO_2 = 80 mg/kg (a) UNS N06255, (b) UNS N06845, (c) UNS N06625 and (d) Ti/Nb rich inclusions in UNS N06625.

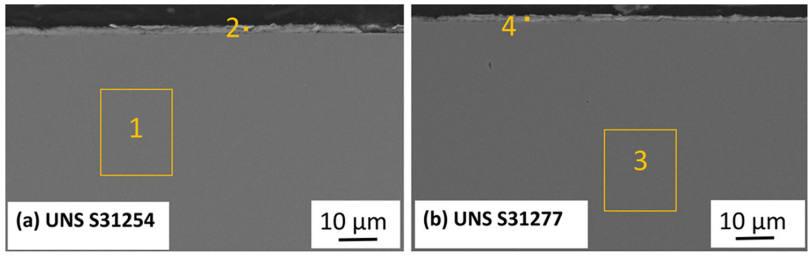

	Element (%wt)								
Location	O	Si	S	Cr	Mn	Fe	Ni	Cu	Mo
1	-	0.6	-	20.3	0.7	54.2	17.8	0.5	6.0
2	6.2	1.7	0.2	18.5	0.4	49.1	17.0	0.6	6.3
3	-	0.4	-	22.0	1.3	41.1	26.4	1.0	7.8
4	11.3	0.8	0.1	18.4	1.1	34.8	24.3	0.5	8.7

Fig. 5. SEM cross section images and XEDS analysis of austenitic stainless steels (a) UNS S31254 and (b) UNS S31277 in H_2S = 150 mg/kg and CO_2 = 250 mg/kg.

rich in oxygen and iron indicating the presence of Fe_3O_4, magnetite layer on the surface. Between the thick outermost layer and the bulk material, a thinner sulphur rich film was observed. Furthermore, chloride rich pits were distributed under the magnetite and sulphur layers as can be seen in Fig. 10. From the deepest pit observed it was concluded that the maximum pit penetration rate was approximately 0.4 mm/year.

3.3. XRD analysis

X-Ray Diffraction (XRD) analysis was done for all the corroded and blank samples to study morphology and formation of new crystalline phases on the surface after the testing. No significant difference was observed between XRD graphs for the nickel-based alloys in low concentration of H_2S and CO_2 as seen in Fig. 11. This was also the case for the nickel-based alloys at the higher concentration of H_2S and CO_2, but small magnetite peaks were detected in the austenitic stainless-steels as seen in Fig. 12. The α-phase in the titanium alloy Ti-4Al-4Mo-2Sn was analysed but in essence, no new crystalline phases were observed after corrosion testing as seen in Fig. 13. For the carbon steel tested, however, magnetite crystals of Fe_3O_4 formed on the surface which is consistent with the XEDS analysis. The XRD graphs of the un-tested and corrosion tested carbon steel are given in Fig. 14. This result implies that the hot steam is oxidizing the iron surface of the carbon steel according to Eqs. (1) and (2) in Cotton [32] and Evans [33], respectively as described in the Discussion chapter.

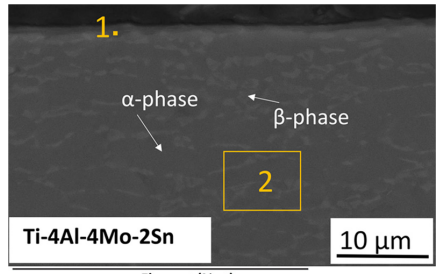

	Element (%wt)						
Location	O	Al	Si	S	Ti	Mo	Sn
1	38.4	2.4	2.9	0.3	52.6	1.8	1.6
2	-	3.8	0.6	-	88.9	4.5	2.2

Fig. 7. SEM image of a cross section and XEDS analysis of titanium alloy Ti-4Al-4Mo-2Sn in H_2S = 150 mg/kg and CO_2 = 250 mg/kg.

3.4. Microetching

Microetching of all the tested samples was done to determine if intergranular corrosion could be observed after the corrosion testing and because of previous experience from in-site testing in IDDP-1 [7]. No grain boundary defects were however observed in the samples but localized damage (pitting) was observed under the surface of the

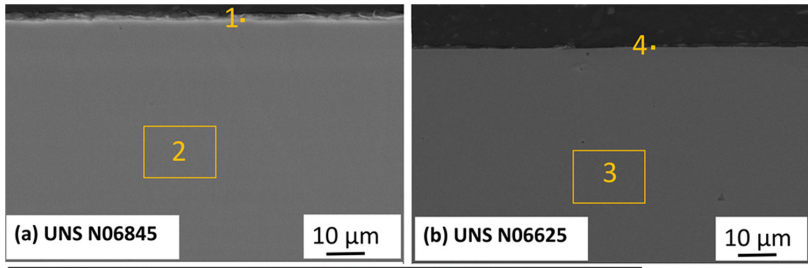

	Element (%wt)													
Location	O	Al	Si	S	Ti	Cr	Mn	Fe	Co	Ni	Cu	Nb	Mo	W
1	15.7	-	-	0.6	-	17.3	-	13.0	-	38.9	2.0	-	6.9	5.7
2		-	-	-	-	23.0	-	16.7	-	47.3	3.0	-	5.9	4.1
3	-	0.2	0.3	-	0.2	21.7	0.1	3.2	0.2	61.2	-	3.8	9.0	-
4	5.9	0.8	3.4	0.5	0.2	18.0	0.3	3.5	0.1	56.1	-	-	-	-

Fig. 6. SEM cross section images and XEDS analysis of nickel-based alloys (a) UNS N06845 and (b) UNS N06625 in H_2S = 150 mg/kg and CO_2 = 250 mg/kg.

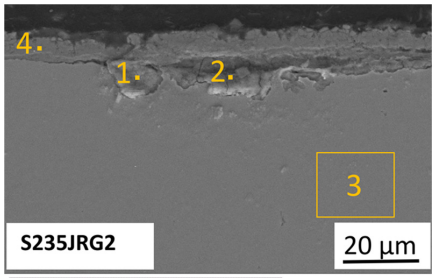

Location	Element (%wt) O	Si	S	Cl	Mn	Fe
1	26.5	7.8	0.5	1.8	0.2	63.2
2	23.4	0.6	0.5	10.0	0.1	65.4
3	-	0.2	-	-	0.2	99.7
4	28.4	0.3	0.7	0.1	0.1	70.4

Fig. 8. SEM images and XEDS analysis of a cross section of carbon steel S235JRG2 in H_2S = 150 mg/kg and CO_2 = 250 mg/kg.

magnetite film on the carbon steel S235JRG2 as previously mentioned in Section 3.2. Microething of the cross section of some of the nickel-based alloys after corrosion testing in low concentration of H_2S and CO_2 can be viewed in Fig. 15.

4. Discussion

Factors influencing corrosion behaviour in high temperature aqueous solution and corrosion behaviour in superheated steam were explained by the difference in fluid properties which have a significant effect on the corrosion behaviour. Kritzer [24] and Tjelta [25] conclude that the most important property of H_2O is the density when determining the corrosion rate in superheated or supercritical water. The polarity and solvent property of a superheated fluid are different from the aqueous fluid. In superheated low-density steam, the relatively long distance between the H_2O molecules makes the steam non-polar and a poor solvent for salts and as a result, ionic compounds such as HCl, will not dissociate into ions. The ionic species are the driving force for the conventional electrochemical corrosion in aqueous electrolyte. Kritzer [24] concluded that the corrosion rate is insignificant when the density of superheated steam is below $200-300\ kg/m^3$ in superheated/supercritical environment. Due to lack of polarity and hence electrochemical pathways for the corrosion reactions for low density fluids, a slow radical chemical reaction is more favourable than electrochemical driven reactions. Marroe [26] states that the most severe corrosion in supercritical water systems is when electrolyte density and concentration of ionic species are high. In the conducted corrosion testing, the density of the superheated fluid was only about 4 kg/m^3 (calculated for pure steam) which is well below the density limit [24] required for the superheated steam to act more like a polar solvent. The density of pure water at a variable temperature at 10 bar gauge can be viewed in Fig. 16. Furthermore, it can be expected that slow radical reactions are preferably occurring but not electrochemical reactions in the testing environment. As a result, radical reactions at the surface of low carbon steel S235JRG2 are likely to have occurred. The difference between the corrosion behaviour of the carbon steel and the more corrosion resistant alloys can be explained by the lack of adherent and sustainable passive film on the low carbon steel S235JRG2. The S235JRG2 lacks chromium and molybdenum to enhance the ability to maintain passive behaviour. It is well known that chromium oxide (Cr_2O_3) film makes a protective film on stainless-steels and nickel-based alloys containing chromium. Molybdenum, which is also a major alloying element in all the corrosion resistant alloys has an ability to enhance the films that provide protective property of nickel-based alloys in corrosive Cl^--H_2S environment [28]. Tomio [28] demonstrated with membrane potential measurements how molybdenum sulphide corrosion film is a cation selective, but in the same paper, it was demonstrated that iron sulphide corrosion film is an anion selective i.e. allowing for instance passage of negative chloride ions through the iron sulphide film. The anion selectivity of iron sulphide film can explain to some extent the reason for chloride enrichment under the sulphide (iron sulphide) layer in S235JRG2 but it should be noted that due to low density of the superheated fluid in the testing, the chloride was from the HCl gas rather than on anionic Cl^- form. However, transportation of liquid microdroplets, enriched with NaCl salt, from preheater to the testing volume should also not be neglected as a possibility. Bornak [29] and Potter [30] reported magnetite formation of iron in oxygen free water/steam environment and addressed also porosity of magnetite film(s). Porous magnetite films have been reported as well in supercritical CO_2 systems at high temperatures and pressures [31]. Magnetite (Fe_3O_4) is a well-known corrosion product on iron. Carbon steel in a superheated environment has been reported with porous magnetite surface films that might promote the under-film corrosion in supercritical CO_2 systems at high temperatures [31]. Magnetite formation on iron surfaces in a boiler system is also well known where it can evolve in water/steam temperatures above 100 °C according to the following reaction [32],

$$3Fe_{(s)} + 4H_2O_{(g)} -> Fe_3O_{4(s)} + 4H_{2(g)} \quad (8)$$

where it is believed that $Fe(OH)_2$ is an intermediate species in the Fe_3O_4 formation according to [33] with the following reaction

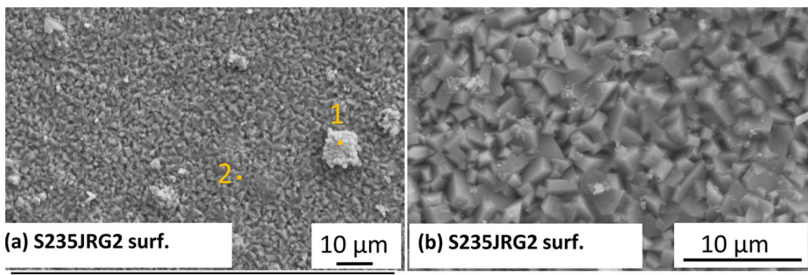

Location	Element (%wt) O	Na	Si	S	Cl	Mn	Fe
1	27.0	7.0	0.2	10.4	-	0.2	55.3
2	25.0	2.4	0.1	0.6	0.9	0.3	70.7

Fig. 9. SEM images and XEDS analysis on external surface of carbon steel S235JRG2 in H_2S = 150 mg/kg and CO_2 = 250 mg/kg at (a) low magnification and (b) at higher magnification.

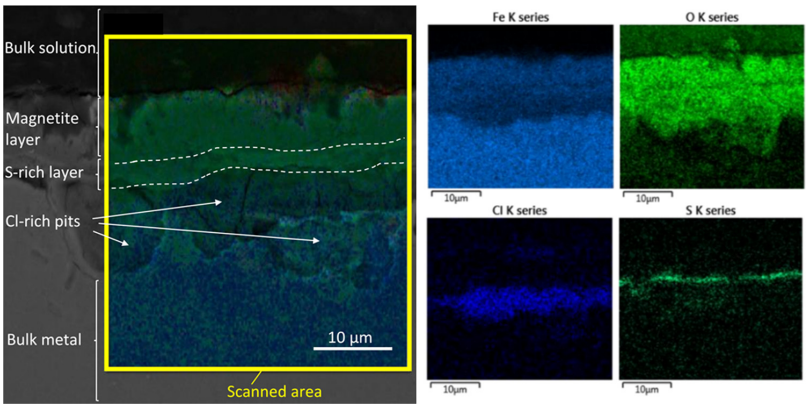

Fig. 10. SEM scanning image (left) of cross section of carbon steel S235JRG2 of oxide layer, sulphur layer and pits profile in the carbon steel in H_2S = 150 mg/kg and CO_2 = 250 mg/kg. The elemental profile for Fe, O, Cl and S from yellow frame from image (left) can be seen in smaller images at right. (For interpretation of the references to colour in this figure legend, the reader is referred to the web version of this article).

$$3Fe(OH)_{2(s)} \text{ - > } Fe_3O_{4(s)} + H_{2(g)} + 2H_2O_{(g)} \quad (9)$$

Some oxide, magnetite like and sulphide corrosion products were reported in carbon steel tested in IDDP-1 well [7,9]. Small magnetite formation according to XRD and SEM analysis in the stainless steels in this study implies that steam is oxidizing the iron in the stainless steels alloy but to smaller extend in comparison with the low carbon steel. Chromium oxide passive layer in the stainless-steel alloys could explain the low extend of magnetite formation from iron in the stainless-steel alloys in comparison with the iron in the carbon steel. Corrosion effect of hydrogen sulphide on iron in geothermal systems is quite well known and proposed mechanism of a reaction of H_2S corrosion on Fe has been proposed Banas [34] where the total reaction is

$$Fe + H_2S \text{ - > } FeS + H_2 \quad (10)$$

The proposed mechanism for acidic chloride attack and diffusion of chlorides through porous magnetite film in boilers resulting in pitting in an aqueous environment is also described in Strehblow [35] but limited data about pitting behaviour of low carbon steel in superheated H_2S-CO_2-HCl environment is available. Literature [36–42] discussing various reaction mechanism between sulphur or hydrogen sulphide

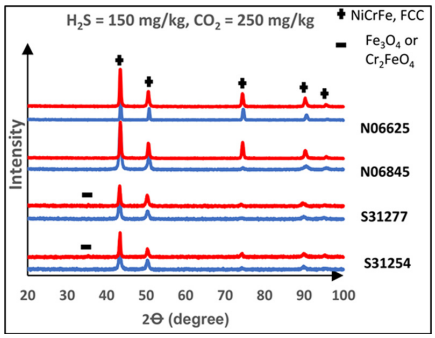

Fig. 12. XRD analysis of corroded (red) and blank (blue) austenitic stainless steels and nickel-based alloys samples in the higher concentration of H_2S/CO_2 testing. (For interpretation of the references to colour in this figure legend, the reader is referred to the web version of this article).

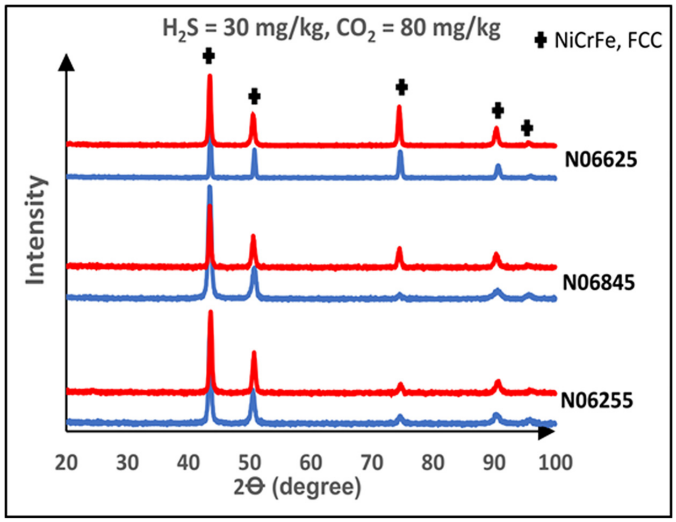

Fig. 11. XRD analysis of corroded (red) and blank (blue) nickel-based samples in the low H_2S/CO_2 concentration testing. (For interpretation of the references to colour in this figure legend, the reader is referred to the web version of this article).

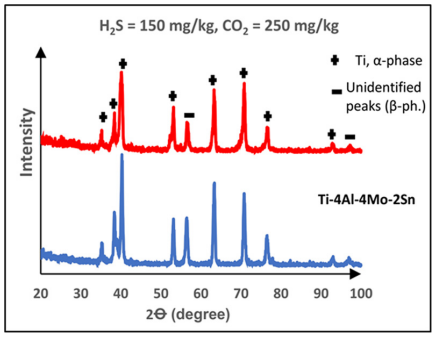

Fig. 13. XRD analysis of corroded (red) and blank (blue) titanium Ti-4Al-4Mo-2Sn samples in the higher concentration of H_2S/CO_2 testing. (For interpretation of the references to colour in this figure legend, the reader is referred to the web version of this article).

vapours with iron shows that corrosion rate, corrosion film structure, integrity and porosity is dependent on several factors including temperature and the composition of the corrosive media. Gao et al. [36] studied formation and propagation mechanism of iron sulphide film on mild steel when the mild steel was tested without oxide film and with preformed $Fe_3O_{4(s)}$ film in a high temperature H_2S environment. The corrosion film mechanism proposes that $Fe_3O_{4(s)}$ forms as an inner layer and $FeS_{(s)}$ forms as an outer layer. Furthermore, the layer growth mechanism in the study indicated that the outer iron sulphide film converts directly from the inner magnetite film. In the carried out testing, the surface of the carbon steel S235JRG2 had chloride enriched pits under inner sulphide corrosion layer and outer magnetite corrosion layer. This layer orientation indicates a different reaction mechanism than experienced in an aqueous environment [36]. The occurrence of inner sulphide layer, outer magnetite layer and chloride rich localized damage under the films in S235JRG2 indicates different corrosion mechanism of low carbon steel is occurring in H_2S-CO_2-HCl environment in comparison with H_2S or H_2S-CO_2 environment. The reaction mechanism of S235JRG2 in our testing could have some similarities with a reaction mechanism proposed by Schmid et al. [43] for stainless steels in H_2S-CO_2-HCl at 680 °C. Schmid et al. proposed gaseous HCl could penetrate oxides passive film in stainless steels and react with the metallic substrate and form volatile $FeCl_{2(g)}$ that could diffuse outwards the corrosion film towards higher partial pressure of $H_2O_{(g)}$ where they would react and produce HCl and iron oxide. The resulting corrosion film would accommodate chloride enriched sites under iron oxide inner layer and iron sulphide outer layer. In our testing, however, the sulphide layer was the inner layer and magnetite the outer layer. This film layer orientation might be explained by the additional effect of gaseous HCl when it penetrates through the porous/disrupted sulphide and preformed magnetite film and reacts with the iron in the bulk metal or with the inner preformed $Fe_3O_{4(s)}$ layer and forms volatile $FeCl_{3(g)}$ and less volatile $FeCl_{2(s)}$ intermediate corrosion product accumulating at the bulk metal surface. From stoichiometry, the reactions at the bulk iron surface and inner magnetite could be as follows:

$$3Fe_{(s)} + 8HCl_{(g)} \text{ - > } FeCl_{2(s)} + 2FeCl_{3(g)} + 4H_{2(g)} \quad (11)$$

$$Fe_3O_{4(s)} + 8HCl_{(g)} \text{ - > } FeCl_{2(s)} + 2FeCl_{3(g)} + 4H_2O_{(g)} \quad (12)$$

The volatile $FeCl_{3(g)}$ corrosion product could then diffuse towards the surface i.e. towards higher partial pressure of $H_20_{(g)}$ where $FeCl_{3(g)}$ reacts with $H_2O_{(g)}$ and forms magnetite, $Fe_3O_{4(s)}$, other chloride and hydrogen-based corrosion products at the external side of iron sulphide layer. Our testing was conducted at 350 °C and from physical properties of iron chlorides [44,45] it is likely that only $FeCl_{3(g)}$ but not $FeCl_{2(g)}$ would act as a volatile corrosion product and diffuse outwards of corrosion film towards higher partial pressures of $H_2O_{(g)}$ and form outer magnetite layer. The reaction mechanism of $FeCl_{3(g)}$ and $H_2O_{(g)}$ to form $Fe_3O_{4(s)}$ is not straightforward and could be a field of future research. We will therefore simplify our proposed mechanism for the reaction mechanism and evolvement of the corrosion form of the carbon steel S235JRG2 in superheated H_2S-CO_2-HCl environment as illustrated in Fig. 17. In our testing of the carbon steel S235JRG2, some amount of sodium (Na) in the chloride enriched pits were detected in the carbon steel at 350 °C but Simonson et al. [46] have shown that NaCl is present in both vapour and liquid state at 350 °C but potential transportation of NaCl dissolved in microdroplets from boiling in preheater to the reactor (s) should not be neglected. It is also quite well known that inclusions can affect corrosion behaviour of metals and alloys as described by Yang [47]. Inclusions could have served as a weak point or initialisation

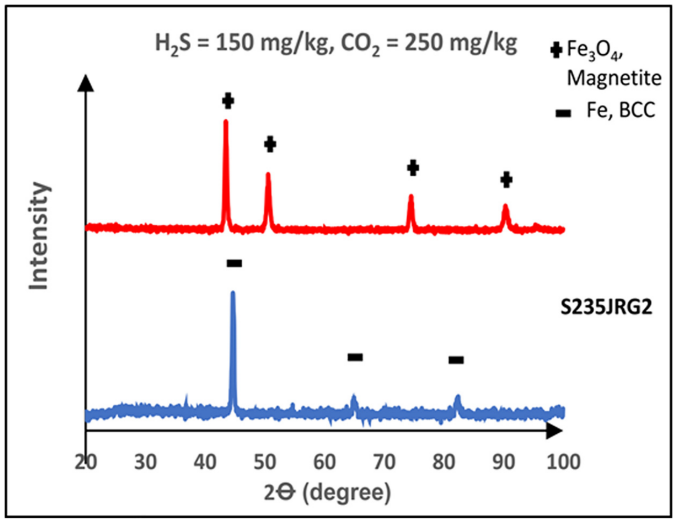

Fig. 14. XRD analysis of corroded (red) and blank (blue) carbon steel S235JRG2 samples in the higher concentration of H_2S/CO_2 testing. (For interpretation of the references to colour in this figure legend, the reader is referred to the web version of this article).

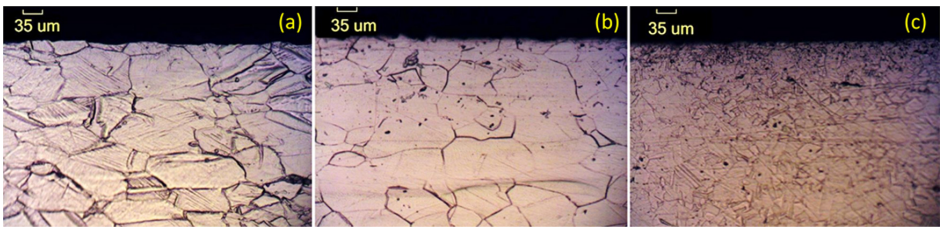

Fig. 15. Etching of (a) UNS N06255, (b) UNS N06845 and (c) UNS N06625 after testing in H_2S = 30 mg/kg and CO_2 = 80 mg/kg.

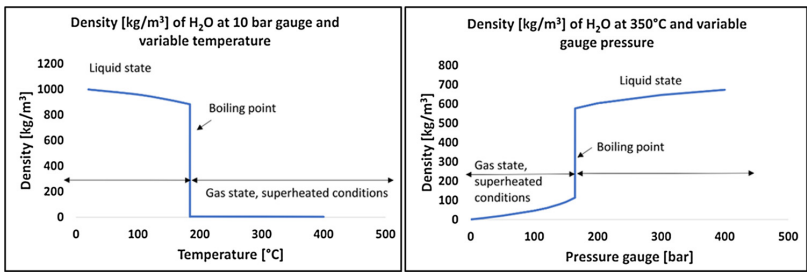

Fig. 16. Density of pure H_2O at 10 bar gauge vs. temperature (left) and density of H_2O at 350 °C vs. gauge pressure (right) with adapted data from [27]. Saturation point of pure water at 10 bar gauge is 184.1 °C and critical temperature of water is at 374 °C.

point for a disruption in the corrosion film, where penetration of $HCl_{(g)}$ through the corrosion film could have occurred and induced the formation of a localized chloride enriched pits in our testing. Oxygen and sulphur rich corrosion products, pitting and localized damage were also observed in carbon steel samples tested in-situ in IDDP-1 well [7,48]. Magnetite has a relatively high electrical conductivity and when magnetite is in contact with carbon steel, it has found to bridge galvanic coupling between the magnetite and the carbon steel. As a result, magnetite film has been reported to accelerate the corrosion rate of carbon steel in a corrosive environment [49]. In our low conductivity corrosive testing fluid, however, the corrosion damage was localized, uniformly distributed at the surface of low carbon steel but more general corrosion damage on the carbon steel would be expected if the galvanic coupling between magnetite and the low carbon steel were inducing corrosion. Corrosion rate experiments in various temperature and pressure indicate that the general corrosion rate below a density of 200 kg/m^3 is very low due to the low ionic character of the fluid [50]. The measured corrosion rate in this study is also consistent with the corrosion rate results observed in the field testing conducted in the superheated fluid in the Iceland Deep Drilling Project no. 1 well [7] as seen in Table 5.

5. Conclusions

In low density, superheated, simulated geothermal fluid containing H_2S, CO_2 and HCl at 350° and 10 bars gauge, the general corrosion rate of carbon steel, austenitic stainless steel, nickel-based alloys and the titanium alloy tested is low. No significant corrosion or morphology changes were observed on the nickel-based alloys and titanium alloy. These results imply that these alloys are more resistant to corrosion than the carbon steel and the austenitic stainless steel in the simulated high temperature geothermal environment. Minor morphology changes were observed on the austenitic stainless steels after the testing. The carbon steel, S235JRG2, was the only material tested that was prone to some localized corrosion damage. Chloride rich pits, under the sulphide inner film and magnetite outer film on the carbon steel, could be explained by a penetration of $HCl_{(g)}$ through the corrosion film that reacts with iron and magnetite, forming volatile $FeCl_{3(g)}$ that diffuses outwards of corrosion film towards higher partial pressures of $H_2O_{(g)}$ where external magnetite layer is formed. No intergranular corrosion was observed in all the materials. All materials tested, except the carbon steel, could be applicable as a construction material in a superheated geothermal environment. From another field testing in the superheated geothermal environment containing H_2S, CO_2, HCl, HF, H_2 and other species, the general corrosion rate was also measured very low, but all the materials tested were however prone to localized corrosion damage. In the current study, localized damage was though only observed in the carbon steel in the simulated high temperature geothermal testing. As the main difference between the reported geothermal field testing and the simulated high temperature geothermal testing is HF and H_2, silica deposition and longer exposure time, it can be concluded that the main reason for localized corrosion damage observed in previous field testing could be due to effect of these additional factors.

Research on the interaction between corrosion and scaling in low temperature geothermal environment has confirmed the protective role of scaling for low grade alloys but limited literature is presently found for this behaviour in superheated geothermal environment. The lower corrosion rate reported in superheated geothermal field in comparison with the testing results presented in the paper might also be due to the protective effect of silica on covering the field samples. Currently, there is an ongoing study by the authors to address this topic by using the current laboratory setup, to study under deposit corrosion behaviour of nickel-based alloys in superheated conditions covered with amorphous silica scale from geothermal field fluid.

Data availability

The raw/processed data required to reproduce these findings cannot be shared at this time as the data also forms part of an ongoing study.

Author statement

Andri Isak Thorhallsson: Conceptualization, methodology, experimental/laboratory work and development of laboratory testing facility, experimental analysis; SEM, XEDS, XRD, micro etching of alloys,

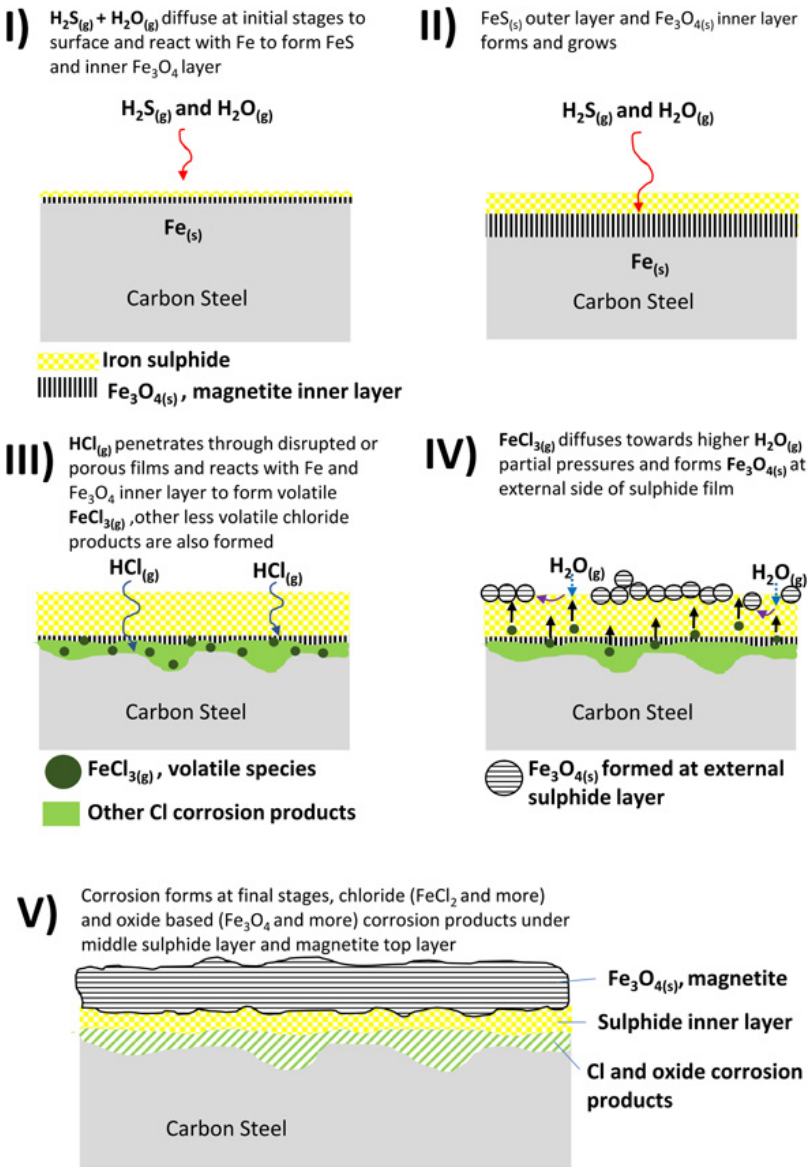

Fig. 17. Proposed mechanism of outer magnetite (Fe_3O_4) film formation, sulphide rich inner layer formation and chloride rich pit formation in carbon steel (S235JRG2) in the simulated geothermal environment.

Table 5
Corrosion rate of few alloys in in-situ testing in Iceland Deep Geothermal Well no.1 – IDDP-1 [5].

Material type	Alloy	Corrosion rate [mm/year]
Low carbon steel	SJ235JRG2	0.004
Austenitic st. steel	UNS S31254	0.001
Nickel based alloy	UNS N06255	0.000
	UNS N06625	0.001
Titanium alloy	UNS R50400	0[a]
	UNS R52400	0.011

[a] Weight gain detected.

optical microscopic analysis, titration, preparation of fluids, validation, visualization, writing original draft preparation, reviewing and editing.

Andri Stefansson: Conceptualization, methodology and reviewing.

Danyil Kovalov: Reviewing and editing of article.

Sigrun Nanna Karlsdottir: Conceptualization, methodology, supervision of project, funding acquisition, reviewing and editing of article.

Declaration of Competing Interest

The authors declare that they have no known competing financial interests or personal relationships that could have appeared to

influence the work reported in this paper.

Acknowledgements

The authors would like to thank the Icelandic Research Fund (RANNÍS, grants no. 163108-051, 163108-052 and 163108-053) and Geothermal Research Group (GEORG) for funding this project. Employees at Innovation Center of Iceland (ICI) and employees at Grein Research for their technical assistance. The authors would also like to give gratitude to Nippon Steel Sumitomo Metals and TIMET for collaboration and providing samples for testing.

Appendix A. Supplementary data

Supplementary material related to this article can be found, in the online version, at doi:https://doi.org/10.1016/j.corsci.2020.108584.

References

[1] S.K. Sanyal, J.W. Morrow, Success and the Learning Curve Effect in Geothermal Well Drilling – A World side Survey, Thirty-Seventh Workshop on Geothermal Reservoir Engineering/2012, Stanford, CA, SGP-TR-194. https://pangea.stanford.edu/ERE/db/IGAstandard/record_detail.php?id=8346.

[2] T. Reinsch, P. Dobson, H. Asanuma, E. Huenges, F. Poletto, B. Sanjuan, Utilizing supercritical geothermal systems: a review of past ventures and ongoing research activities, Geotherm Energy 5 (2017) 16, https://doi.org/10.1186/s40517-017-0075-y.

[3] G.O. Fridleifsson, W.A. Elders, The Iceland Deep Drilling Project: a search for deep unconventional geothermal resources, Geothermics 34 (2005) 269–285, https://doi.org/10.1016/j.geothermics.2004.11.004.

[4] R.O. Fournier, Hydrothermal processes related to moment of fluid from plastic into brittle rock in the magmatic-epithermal environment, Econ. Geol. 94 (1999) 1193–1211, https://doi.org/10.2113/gsecongeo.94.8.1193.

[5] G.O. Fridleifsson, A. Albertsson, W.A. Elders, The iceland deep drilling project (IDDP): planning for the second deep well at Reykjanes, GRC Trans. 35 (2011) 347–354.

[6] T. Hauksson, S. Markusson, K. Einarsson, S.N. Karlsdottir, A. Einarsson, A. Moller, T. Sigmarsson, Pilot testing of handling the fluids from the IDDP-1 exploratory geothermal well, Krafla, N.E. Iceland, Geothermics 49 (2014) 76–82, https://doi.org/10.1016/j.geothermics.2013.07.003.

[7] S.N. Karlsdottir, K.R. Ragnarsdottir, I.O. Thorbjornsson, A. Einarsson, Corrosion testing in superheated geothermal steam in Iceland, Geothermics 53 (2015) 281–290, https://doi.org/10.1016/j.geothermics.2014.06.007.

[8] S.N. Karlsdottir, K.R. Ragnarsdottir, A. Moller, I.O. Thorbjornsson, A. Einarsson, On-site erosion-corrosion testing in superheated geothermal steam, Geothermics 51 (2014) 170–181, https://doi.org/10.1016/j.geothermics.2014.01.007.

[9] S.N. Karlsdottir, I.O. Thorbjornsson, T. Sigmarsson, Corrosion and Scaling in Wet Scrubbing Equipment of the Superheated Geothermal Well IDDP-1 in Iceland, Corrosion/2013, NACE, Orlando, FL, paper no. 2556. https://store.nace.org/corrosion-and-scaling-in-wet-scrubbing-equipment-of-superheated-geothermal-well-iddp-1-in-iceland.

[10] I.O. Thorbjornsson, S.N. Karlsdottir, T. Sigmarsson, Corrosion Testing of Heat Exchanger Tubes in Steam from the IDDP-1 Exploratory Geothermal Well in Krafla Iceland, Corrosion/2014, San Antonio, TX, paper no. 9680. https://store.nace.org/corrosion-testing-of-heat-exchanger-tubes-in-steam-from-the-iddp-1-exploratory-geothermal-well-in-kr.

[11] K. Ingason, V. Kristjánsson, K. Einarsson, Design and development of the discharge system of IDDP-1, Geothermics 49 (2014) 58–65, https://doi.org/10.1016/j.geothermics.2013.05.002.

[12] E.T. Eliasson, A. Einarsson, Corrosion in Icelandic high-temperature geothermal systems, Mater. Perform. Charact. 10 (21) (1982) 35–39.

[13] S.N. Karlsdottir, I.O. Thorbjornsson, Corrosion Testing Down-hole in a Sour High Temperature Geothermal Well in Iceland, Corrosion/2013, NACE, Orlando, FL, paper no. 2550. https://store.nace.org/corrosion-testing-downhole-in-sour-high-temperature-geothermal-well-in-iceland.

[14] W.F. Bogaerts, I. Winstons, Geothermal Corrosion: High-temperature Pitting of Stainless steels and Ni-alloys, Corrosion/2017, NACE, New Orleans, LA, paper no. 9269. https://store.nace.org/geothermal-corrosion-high-temperature-pitting-of-stainless-steels-and-ni-alloys.

[15] A.I. Thorhallsson, S.N. Karlsdottir, A. Stefansson, Corrosion Testing of UNS S31603 in Simulated HT Geothermal Environment at Boiling, Superheated and Condensation Condition, Corrosion/2019, NACE, Nashville, TN, paper no. 13195. https://www.onepetro.org/conference-paper/NACE-2019-13195.

[16] A.I. Thorhallsson, S.N. Karlsdottir, A. Stefansson, Corrosion Testing of UNS N06625 in Simulated High Temperature Geothermal Environment, Corrosion/2018, NACE, Phoenix, AZ, paper no. 11058. https://store.nace.org/corrosion-behavior-of-austenitic-stainless-steels-and-nickel-alloys-in-simulated-ht-geth-environm-2.

[17] S. Arnorsson, Isotopic and Chemical Techniques in Geothermal Exploration, Development and Use: Sampling Methods, Data Handling, Interpretation, International Atomic Energy Agency, Vienna, 2000, pp. 114–115 https://www.iaea.org/publications/5733/isotopic-and-chemical-techniques-in-geothermal-exploration-development-and-use-sampling-methods-data-handling-interpretation-edited-by-stefan-arnorsson.

[18] S. Arnorsson, J.O. Bjarnason, N. Giroud, I. Gunnarsson, A. Stefansson, Sampling and analysis of geothermal fluids, Geofluids 6 (2006) 203–216, https://doi.org/10.1111/j.1468-8123.2006.00147.x.

[19] S. Arnorsson, Isotopic and Chemical Techniques in Geothermal Exploration, Development and Use: Sampling Methods, Data Handling, Interpretation, International Atomic Energy Agency, Vienna, 2000, pp. 108–113 https://www.iaea.org/publications/5733/isotopic-and-chemical-techniques-in-geothermal-exploration-development-and-use-sampling-methods-data-handling-interpretation-edited-by-stefan-arnorsson.

[20] ASTM International, ASTM G1-90: Standard Practice for Preparing, Cleaning, and Evaluating Corrosion Test Specimens, (2017), p. 3 https://www.astm.org/Standards/G1.

[21] G. Petzow, Metallographic Etching, American Society for Metals, Ohio, USA, 1978, p. 64.

[22] G. Petzow, Metallographic Etching, American Society for Metals, Ohio, USA, 1978, p. 87.

[23] G.F. Vander Voort, J.W. Bowman, R.B. Frank, Microstructural characterization of custom age 625 plus alloy, The Minerals, Metals & Materials Society (1994) 489–498 https://www.researchgate.net/publication/269258305_Microstructural_Characterization_of_Custom_Age_625_Plus_Alloy.

[24] Peter Kritzer, Corrosion in high-temperature and supercritical water and aqueous solutions: a review, J. Supercrit. Fluids 29 (2004) 1–29, https://doi.org/10.1016/S0896-8446(03)00031-7.

[25] M. Tjelta, B.C. Krogh, S. Sæther, M. Seiersten, Corrosion, Scaling and Material Selection in Deep Geothermal Wells - Application to IDDP-2, Corrosion/2019, paper no. 13299 NACE, Nashville, TN, 2019https://store.nace.org/corrosion-scaling-and-material-selection-in-deep-geothermal-wells-a-case-study-of-iddp-2-63025.

[26] P.A. Marroe, G.T. Hong, Corrosion control methods in supercritical water oxidation and gasification processes, J. Supercrit. Fluids 51 (2009) 83–103, https://doi.org/10.1016/j.supflu.2009.08.001.

[27] Wolfram Alpha LLC, Wolfram Alpha Widgets, (2019) (Accessed 7 August 2019), https://www.wolframalpha.com/widgets/view.jsp?id=1de7d2b90d554be9f0db1c338e80197d.

[28] A. Tomio, M. Sagara, T. Doi, H. Amaya, N. Otsuka, T. Kudo, Role of alloyed molybdenum on corrosion resistance of austenitic Ni-Cr-Mo-Fe alloys in H_2S-Cl^- environments, Corros. Sci. 98 (2015) 391–398.

[29] W.E. Bornak, Chemistry of Iron and its corrosion products in boiler systems, Corrosion 44 (3) (1988) 154–158, https://doi.org/10.1016/j.corsci.2015.05.053.

[30] E.C. Potter, G.M.W. Mann, The fast linear growth of magnetite on mild steel in high-temperature aqueous conditions, Br. Corros. J. 1 (1) (1965) 26–35, https://doi.org/10.1179/000705965798328182.

[31] V. Firouzdor, K. Sridharan, G. Cao, M. Anderson, T.R. Allen, Corrosion of a stainless steel and nickel-based alloys in high temperature supercritical carbon dioxide environment, Corros. Sci. 69 (2013) 281–291, https://doi.org/10.1016/j.corsci.2012.11.041.

[32] F.A. Cotton, G. Wilkinson, Advanced Inorganic Chemistry, 4th edition, Wiley-Interscience, New York, New York, 1980, pp. 752–766.

[33] U.R. Evans, J.N. Wanklyn, Evolution of hydrogen from ferrous hydroxide, Nature 162 (1948) 27, https://doi.org/10.1038/162027b0.

[34] J. Banas, U. Lelek-Borkowska, B. Mazurkiewics, W. Solarski, Effect of CO_2 and H_2S on the composition and stability of passive film on iron alloys in geothermal water, Electrochm. Acta 52 (2007) 5704–5714, https://doi.org/10.1016/j.electacta.2007.01.086.

[35] H.H. Strehblow, Mechanism of pitting corrosion, in: P. Marcus (Ed.), Corrosion Mechanisms in Theory and Practice, CRC Press, Boca Raton, 2012, p. 370.

[36] S. Gao, B. Brown, D. Young, S. Nesic, M. Singer, Formation Mechanism of Iron Oxide and Iron Sulfide at High Temperature in H2S Corrosion Environment, Corrosion/2018, NACE, Phoenix, AZ, paper no. 11027. https://store.nace.org/formation-mechanisms-of-iron-oxide-and-iron-sulfide-at-high-temperature-in-h2s-corrosion-environment-2.

[37] Z.A. Foroulis, Kinetics and mechanism of the reaction of iron with sulfur vapor in the temperature range of 250 to 500°C, Werkst. Und Korrosion 29 (1978) 385–393, https://doi.org/10.1002/maco.19780290602.

[38] H. Ma, X. Cheng, G. Li, S. Chen, Z. Quan, S. Zhao, L. Niu, The influence of hydrogen sulfide on corrosion of iron under different conditions, Corros. Sci. 42 (2000) 1669–1683, https://doi.org/10.1016/S0010-938X(00)00003-2.

[39] W. Sun, S. Nesic, S. Papavinasam, Kinetics of corrosion layer formation. Part 2 – iron sulfide and mixed Iron sulfide/carbonate layers in carbon Dioxide/Hydrogen sulfide corrosion, Corrosion 64 (no.7) (2008) 586–599, https://doi.org/10.5006/1.3278494.

[40] S. Ramachandran, M.B. Ward, K.A. Bartrip, Molecular Modelling of Corrosion of Iron in H2S Environments, Corrosion/2002, Denver, CO, paper no. 02240. https://store.nace.org/02240-molecular-modeling-of-corrosion-of-iron-.

[41] R.C. John, A.L. Young, New Understanding on Corrosion of Alloys in High-Temperature Sulfidizing Gases, Corrosion/2002, Denver, CO, paper no. 02486. https://store.nace.org/02486-new-understanding-on-corrosion-of-.

[42] N.A.C.E. International, Task Group (TG) 176, Overview of Sulfidation (Sulfidic) Corrosion in Petroleum Refining Hydroprocessing Units, NACE International Publication, 2014, p. 34103 https://store.nace.org/nace-publication-34103-2014-.

[43] A. Schmid, G. Mori, E. Bucher, R. Haubner, Model about the course of corrosion reactions of austenitic steels in H2S-, HCl- and CO2-Containing atmospheres at 680°C, Oxid. Met. 91 (2019) 1–10, https://doi.org/10.1007/s11085-018-9876-z.

[44] Pierre R. Roberge, Handbook of Corrosion Engineering, second ed., McGraw-Hill,

USA, 2012, p. 218.
[45] Michael Schütze, High-temperature corrosion, in: P. Marcus (Ed.), Corrosion Mechanisms in Theory and Practice, CRC Press, Boca Raton, 2012, p. 575.
[46] J.M. Simonson, D.A. Palmer, R.W. Carter, Liquid-Vapor Partitioning of NaCl(aq) from Concentrated Brines at Temperatures to 350°C, Nineteenth Workshop on Geothermal Reservoir Engineering/1994, Stanford, CA. https://www.osti.gov/servlets/purl/10126322.
[47] S. Yang, M. Zhao, J. Feng, J. Li, C. Liu, Induced-pitting behaviors of MnS inclusions in steel, High Temp. Mater. Process. 37 (9-10) (2018) 1007–1016, https://doi.org/10.1515/htmp-2017-0155.
[48] K.R. Ragnarsdottir, Corrosion Experiments in Dry Superheated Steam From IDDP-1, M.SC. Thesis, University of Iceland, Faculty of Industrial Engineering, Mechanical Engineering and Computer Science, 2013, http://hdl.handle.net/1946/13893.
[49] G.D. Song, S.-H. Jeon, Y.-H. Son, J.G. Kim, D.H. Hur, Galvanic effect of magnetite on the corrosion behavior of carbon steel in deaerated alkaline solutions under flowing conditions, Corros. Sci. 131 (2018) 71–80, https://doi.org/10.1016/j.corsci.2017.10.017.
[50] P. Kritzer, N. Boukis, E. Dinjus, Review of the corrosion of nickel-base alloys and stainless steels in strongly oxidizing pressurized high-temperature solutions at sub- and supercritical temperatures, Corrosion 56 (2000) 1093, https://doi.org/10.5006/1.3294394.

Corrosion Science 174 (2020) 108807

Contents lists available at ScienceDirect

Corrosion Science

journal homepage: www.elsevier.com/locate/corsci

Corrigendum

Corrigendum to "Corrosion testing of materials in simulated superheated geothermal environment" [Corros. Sci. 168 (2020) 10]

Andri Isak Thorhallsson[a,*], Andri Stefansson[b], Danyil Kovalov[a], Sigrun Nanna Karlsdottir[a]

[a] Faculty of Mechanical Eng., Industrial Eng. and Computer Science, University of Iceland, Hjardarhagi 2-6, 107 Reykjavik, Iceland
[b] Institute of Earth Sciences, University of Iceland, Sturlugata 7, 101 Reykjavik, Iceland

The authors regret < incorrect XRD data for corroded S235JRG2 in Figure 14 in manuscript. > .

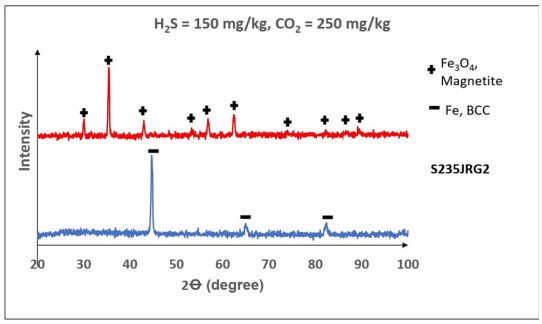

The authors would like to apologise for any inconvenience caused.

DOI of original article: https://doi.org/10.1016/j.corsci.2020.108584
* Corresponding author.
E-mail address: ath196@hi.is (A.I. Thorhallsson).

https://doi.org/10.1016/j.corsci.2020.108807

Available online 23 June 2020

Journal Article 2

A.I. Thorhallsson, I. Csáki, L.E. Geambazu, F. Magnus, S.N. Karlsdottir, Effect of alloying ratios and Cu-addition on corrosion behaviour of CoCrFeNiMo high-entropy alloys in superheated steam containing CO_2, H_2S and HCl, Corros. Sci. 178 (2021) 109083. https://doi.org/10.1016/j.corsci.2020.109083.

Corrosion Science 178 (2021) 109083

Contents lists available at ScienceDirect

Corrosion Science

journal homepage: www.elsevier.com/locate/corsci

Effect of alloying ratios and Cu-addition on corrosion behaviour of CoCrFeNiMo high-entropy alloys in superheated steam containing CO_2, H_2S and HCl

Andri Isak Thorhallsson [a,*], Ioana Csáki [b], Laura Elena Geambazu [b], Fridrik Magnus [c], Sigrun Nanna Karlsdottir [a]

[a] Faculty of Mechanical Eng., Industrial Eng. and Computer Science, University of Iceland, Hjardarhagi 2-6, 107 Reykjavik, Iceland
[b] University Politehnica Bucharest, Splaiul Independentei 313, Bucharest 060042, Romania
[c] Science Institute, University of Iceland, Dunhaga 3, 107 Reykjavik, Iceland

ARTICLE INFO

Keywords:
High-entropy alloys
Copper
Intermetallics
SEM
XRD
High-temperature corrosion

ABSTRACT

This article reports the morphology and corrosion study of CoCrNiFeMo and CoCrNiFeMoCu high-entropy alloys (HEA) tested in a simulated superheated geothermal environment to evaluate whether the alloys are candidate materials for a corrosive high-temperature geothermal environment. The HEA alloys with different alloying ratios were tested in superheated steam at 350 °C and 10 bar gauge containing HCl, H_2S, and CO_2 with acidic condensate (pH = 3). The Cu containing CoCrNiFeMoCu alloys were prone to corrosion damage and corrosion rate was accelerated by intermetallic Cu rich sites but the CoCrNiFeMo alloys were not prone to corrosion in the test environment.

1. Introduction

High-Entropy Alloys (HEAs) have been found to possess many properties that are practical in an erosive and a corrosive geothermal environment, including corrosion resistance and high hardness [1,2]. HEAs are a class of materials with five or more elements mixed in one alloy in equimolar or near equimolar ratios yielding one or a few solid solutions. The four main effects contributing to enhanced properties of HEAs have been summarized by Zhang et al. [3] and are in essence; high-entropy mixing, sluggish diffusion, lattice distortion, and cocktail effect. Due to these various effects, HEAs can be designed to improve mechanical and corrosion resistance properties which can be beneficial in a demanding erosive-corrosive geothermal environment. In terms of alloy composition of HEAs, elements such as Mo and Cu can change morphology, segregation behaviour of elements and phase structure, and thus alter mechanical properties and corrosion resistance of HEAs [4,5].

Geothermal energy is generally utilized by drilling geothermal wells which discharge geothermal fluid (steam/water, dissolved components and other gases) from a geothermal reservoir in the earth's crust or mantle. The hot geothermal fluid is eventually used for electrical power production and district heating as demonstrated in Fig. 1 which shows a simplified geothermal energy production system. The geothermal fluid can be corrosive when it comes in contact with process equipment made of metallic alloys such as well casing, surface piping and equipment such as turbines and separators. In Iceland, the temperature range down-hole in a geothermal well is normally in the range of 230−350 °C and the power production from each well is approximately 3−5 MW [6]. In recent decades, interest has grown in drilling deeper geothermal wells to discharge a higher enthalpy fluid from geothermal systems in Iceland. The geothermal fluid from a deep well is expected to be supercritical or superheated and the potential power production per deep geothermal well has been estimated to be increased tenfold compared to a conventional well [7,8]. Deep geothermal wells are an expensive investment and it is important that deep well materials endure the corrosive high-temperature fluid which can limit the lifetime of the well to reduce the economic aspect of producing geothermal energy. In the first deep geothermal well (IDDP-1) drilled in Iceland in 2008, the geothermal fluid at the wellhead was measured at 440−450 °C with corrosive species such as CO_2, H_2S, HCl, HF, H_2 and other substances [9,10]. In-situ corrosion testing for multiple alloys was conducted in a test chamber connected to the IDDP-1 wellhead where the temperature was

* Corresponding author.
E-mail address: ath196@hi.is (A.I. Thorhallsson).

https://doi.org/10.1016/j.corsci.2020.109083
Received 22 June 2020; Received in revised form 14 October 2020; Accepted 20 October 2020
Available online 23 October 2020

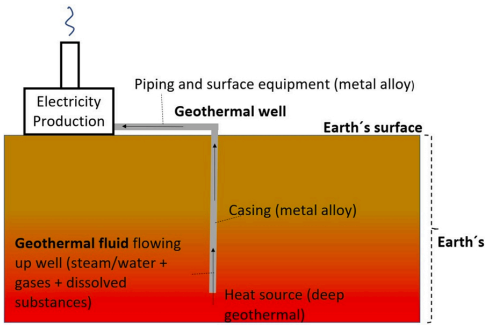

Fig. 1. Simplified geothermal well system.

350 °C and 12–13 bar gauge. The corrosion rate for all the alloys, low alloy carbon steels, stainless steels, nickel-based alloys and titanium alloys was very low (<<0.1 mm/year) but all the alloys suffered localized damage such as cracking or pitting as reported by Karlsdottir et al. [11]. Erosion-corrosion testing at the wellhead showed that the SiO_2 containing fluid from IDDP-1 well was erosive at low (48 m/s) and higher velocities (>98 m/s) [12]. These results imply that future selection of materials in deep geothermal equipment must endure an erosive and corrosive environment. Due to feasible properties of HEAs, they should be considered as a promising candidate for material selection in a corrosive deep geothermal environment, either as a protective coating or structural material.

In this paper, one alloy of CoCrFeNiMo in equimolar ratios, three alloys of CoCrFeNiMo in near equimolar ratios and two alloys of CoCrFeNiMoCu (Cu added CoCrFeNiMo), produced via vacuum arc melting (VAM) method, will be investigated. The available production methods for HEAs are several but Yeh et al. [13] has shown that HEAs produced via VAM method can have many appealing design properties over other production methods. The equimolar VAM fabricated CoCrFeNiMo high-entropy alloy has previously been tested by Csaki et al. [1] in two-phase geothermal steam containing H_2S and CO_2 gases at 200 °C where some sulphur and oxygen corrosion products were detected but very low corrosion rate (<< 0.1 mm/year) was measured. The corrosive geothermal fluid in the in-situ testing did not include HCl as one of the corrosive species whereas it has been observed in deep superheated geothermal fluids in Iceland [9,10]. The bulk CoCrFeNiMo high-entropy alloy has also been tested electrochemically at 25 °C in 3.5 wt% NaCl solution [2]. The measured corrosion rate for the CoCrFeNiMo alloy was low (<<0.1 mm/year) in the electrochemical testing, demonstrating good corrosion resistance of the CoCrFeNiMo alloy. From all the results summarized in the paper discussed it was concluded that the CoCrFeNiMo high-entropy alloy could be a promising candidate for coating in a harsh geothermal environment [2].

In this research, four different CoCrFeNiMo alloys and two additional Cu added CoCrFeNiMoCu alloys are studied in a simulated geothermal environment at 350 °C and 10 bar gauge where the fluid is superheated steam containing H_2S, CO_2 and HCl. Copper (Cu) is an interesting alloying element in terms of high-entropy alloy study. Nene et al. [14] investigated Cu added high-entropy alloys that exhibited good corrosion resistance and mechanical properties due to the formation of a γ phase detected in the microstructural analysis. Ren et al. [15] have reported reduced passivation effect of Cu addition in HEA due to Cr-depleted areas in the alloy. Hsu et al. [5] investigated the effect of Cu addition on corrosion behaviour of a $FeCoNiCr_x$ alloy in a 3.5 % wt. NaCl solution where it was concluded that Cu reduced corrosion resistance and induced localized corrosion damage due to Cu segregation in the high-entropy alloy. The Cu segregation was concluded to be due to lack of binding forces between Cu and other elements (Fe, Co, Ni, Cr). Furthermore, it was concluded that Cu segregation formed galvanic coupling between Cu rich and Cu depleted sites. The same galvanic effect of Cu has been observed by Ren et al. [15] in $CoCrFeNiCu_x$ high-entropy alloys in a 1 M H_2SO_4 solution. The effect of the alloying element Mo in CoCrFeNiTiMo alloys has also been investigated and has been concluded to have a similar effect on corrosion resistance on HEAs as on stainless steels i.e. increases pitting corrosion resistance as reported by Chou et al. [16,17]. From previous research, it has been demonstrated that equimolar CoCrFeNiMo high-entropy alloy has good corrosion resistance in a geothermal environment at intermediate temperatures (≤ 200 °C) [1]. No corrosion testing of HEAs has yet been conducted in a high temperature, superheated deep geothermal environment where HCl is also present in the corrosive medium. Previous studies of corrosion behaviour of a range of alloys in simulated deep geothermal environment have shown low uniform corrosion rates (<0.01 mm/year) for all alloys tested except carbon steel (0.042 mm/year) and no indications of localized corrosion damage in the corrosion-resistant alloys tested except in the carbon steel that was prone to localized damage [18–20].

This research is a continuation of corrosion testing of materials in a simulated superheated geothermal environment at 350 °C and 10 bar gauge in a flow-through corrosion testing facility where the corrosive fluid is steam containing H_2S, CO_2 and HCl [18]. The result presented in this paper will reveal the morphology and corrosion behaviour of six different CoCrFeNiMo high-entropy alloys; four alloys without and two alloys with Cu addition in a simulated high-temperature geothermal environment. The testing conditions are similar to conditions experienced in deep geothermal systems excluding the erosive factors and higher pressure. The aims of this work were to 1) study the corrosion behaviour of CoCrNiFeMo and CoCrNiFeMoCu high-entropy alloys in the simulated superheated geothermal environment and 2) study the effect of different Mo:Cu ratios in CoCrFeNiMo based HEAs on morphology and corrosion resistance in the simulated superheated geothermal environment.

2. Experimental

2.1. Materials and processing

Four high-entropy alloys were prepared by mixing high purity metals of Co, Cr, Cu, Fe, Ni and Mo via vacuum arc remelting (VAR) method in a high-temperature furnace from a Material Research laboratory under a high purity argon gas. Two other compositions of high-entropy alloys were prepared in the same manner with the same elements but with a Cu added as an alloying element. The high purity metals were melted together at 3000 °C with an electrode, melting, solidified and remelted five times for a homogeneous structure. The samples had dimensions of 50 mm length, 7 mm width and 2 mm thickness. Table 1 shows the compositions of the prepared HEAs. The chemical composition for the HEAs was selected in such way that the sample HEA1 was in an equiatomic ratio (of Co, Cr, Fe, Ni and Mo) but the sample alloys HEA2-HEA4 had different ratios where the Mo and Co contents were altered relative to the other elements. In samples HEA5 and HEA6, Cu was added as an alloying element where HEA5 had an equiatomic ratio but HEA6 had more Cu and less Mo in comparison with HEA5.

Table 1
Atomic ratios (at%) of elements in the HEA alloys tested.

Element	HEA1 [at%]	HEA2 [at%]	HEA3 [at%]	HEA4 [at%]	HEA5 [at%]	HEA6 [at%]
Co	20	22.5	17.5	30	16.7	17.8
Cr	20	22.5	17.5	17.5	16.7	17.8
Cu	–	–	–	–	16.7	21.0
Fe	20	22.5	17.5	17.5	16.7	17.8
Ni	20	22.5	17.5	17.5	16.7	17.8
Mo	20	10	30	17.5	16.7	8.0

2.2. Testing medium

The testing fluid was formulized such that the CO_2, H_2S and HCl were the corrosive species in the steam as experienced in the actual geothermal IDDP-1 well fluid [9,10]. Some other corrosive components were excluded in the simulated testing fluid such as HF, H_2 and CH_4 and erosive particles such as SiO_2. The simulated deep geothermal fluid was prepared with two reactant solutions. Reactant solution no.1 contained diluted $HCl_{(aq)}$ solution but the reactant solution no.2 contained dissolved anhydrous $Na_2S_{(aq)}$ and $NaHCO_{3(aq)}$. The molar number of the dissolved species in both aqueous reactant solutions can be seen in Table 2. To determine the concentrations of S^{2-} (and hence H_2S), and CO_2 in the test solutions the reactant solutions were titrated with a method commonly used for simulating geothermal fluids as described by Thorhallsson et al. [18]. The two reactant solutions were mixed at high-pressure before the inlet of a preheater to yield the testing solution which had pH = 3 and concentration of CO_2 = 250 ppm and H_2S = 150 ppm. The chemical composition and physical properties of the testing fluid and conditions can be seen in Table 3.

2.3. Corrosion testing facility

Six different HEA samples were tested for 10 days in two reactors connected in series. The simulated geothermal testing fluid was made by preparation and mixing of the two reactant solutions described previously. At the inlet of the testing facility, the two reactant solutions were stored in flasks connected to Labhut degassers to remove volatiles and dissolved gasses from the testing fluid. Two high-pressure ChromTech pumps were connected between the degassers and the inlet of the preheater. The reactant solutions were mixed under high pressure at a mixing point before the inlet of the preheater where the simulated geothermal fluid was superheated. After the preheating of the testing fluid, it flowed through two reactors connected in series. Three HEA testing samples were accommodated in each reactor unit, a total of 6 samples in both reactors. To exclude possible galvanic corrosion effects from the reactor pipe wall, all the testing samples were electrically insulated from reactor walls by installing alumina insulators between the samples and the reactor pipes. The testing fluid was condensed and cooled after the outlet of the second reactor in a water-cooled condenser. An inline pressure transducer and gauge were connected to the testing facility at the outlet of the second reactor to monitor the pressure during the testing. A back-pressure regulator (BPR), where the process pressure was set by a SITEC hand pump, was connected to the testing equipment after the pressure transducer and pressure gauge. The temperature and pressure were monitored with a Labjack data logging system.

2.4. Microstructural analysis

Microstructural analysis with a Scanning Electron Microscope (SEM) equipped with Energy Dispersive X-ray Spectroscopy (XEDS) and Back-Scattered Electron (BSE) detector of the external surfaces and prepared cross-sections was done for all the samples before and after the corrosion testing. The samples were prepared for the analysis by cross-sectioning with a diamond wafering blade and then mounted in thermosetting phenol formaldehyde resin (bakelite) and cast under pressure. The cross-sectioned samples were ground to 1000 grit with SiC abrasive paper and polished further with 3 μm and 1 μm diamond paste slurry and eventually polished with 0.02−0.06 μm particle size colloidal silica. The SEM equipment used was a Zeiss Supra 25. The XEDS instrument used was from Oxford Instruments with a Si(Li) X-ray detector and AZtec software.

Table 2
Molar concentrations of HCl, Na_2S and $NaHCO_3$ in the aqueous mixing solutions.

Parameter	Value	Unit
Reactant solution 1:		
HCl	31	mmol
Total volume	1000	ml
Reactant solution 2:		
Na_2S	8.8	mmol
$NaHCO_3$	11.4	mmol
Total volume	1000	ml

Table 3
Physical condition, the chemical composition of testing fluid and duration of testing.

Parameter	Value	Unit
pH	3*	
Temperature	350	°C
Fluid pressure	10	bar gauge
Total inlet volumetric flow rate	0.3	ml/min
Testing period	10	days
CO_2	250	ppm
H_2S	150	ppm
HCl	36.5**	ppm

* Measured at 20 °C.
** Unreacted HCl in the reactant solution.

2.5. Crystal structure analysis

X-ray diffraction (XRD) analysis was done with an X'Pert Pro MRD system from PANalytical with a Göbel mirror on the incident side and parallel plate collimator on the diffracted side. The data were collected in a standard θ-2θ geometry and analysed with the HighScore software. Samples were analysed by XRD before and after the corrosion testing.

3. Results

3.1. Microstructural and chemical analysis

Microstructural analysis with SEM and chemical analysis with XEDS was done for all the untested HEA samples on the surface and in cross-section. In general, two apparent phases were observed in all the samples consisting of a dendrite (DR) and interdendrite (ID) microstructure; Mo tends to be enriched in the dendrite phase while Ni-Fe is enriched in the interdendrite phase, as illustrated in Figs. 2–5.

The excess element in a solid solution can be dissolved in a compatible matrix element. Co and Ni could form a continuous solid solution (Co αNi) but can also dissolve Fe in austenite. Stefanoiu et al. [21] reported typical dendrite in a HEA containing Co, Cr, Fe and Ni and acicular and cuboidal compounds in the interdendrite region. The elemental segregation could be explained by the mixing enthalpies of the components [22]. Mo is heavier and larger than the other components and tends to migrate in the interdendrite space. After corrosion testing, negligible corrosion was observed in samples HEA1- HEA4 but the Cu added alloys HEA5 and HEA6 were prone to general corrosion and some localized damage under the corrosion film. Oxide inclusions were observed in all the HEA samples and Mo rich and Ni-Fe rich phases were apparent in all the samples. A thin surface corrosion oxide layer on HEA1 was apparent when compared to the untested HEA1 sample. Corrosion products of oxygen (O) and sulphur (S) formed on sample HEA1 but negligible corrosion effects were observed in samples HEA2 – HEA4, whereas oxide film products were dominant and only minor sulphur corrosion products, were detected on the surface of HEA4, as can be seen in Fig. 3.

On the other hand, sulphur (S) rich corrosion layer was observed in the Cu containing alloys; HEA5 and HEA6. Of all the HEA compositions tested, the densest corrosion layer (sulphur-rich) was observed in sample HEA6 indicating that the alloy was the most susceptible of the alloys tested for general corrosion in the testing environment. The second densest corrosion layer was observed in the other Cu added HEA sample HEA5.

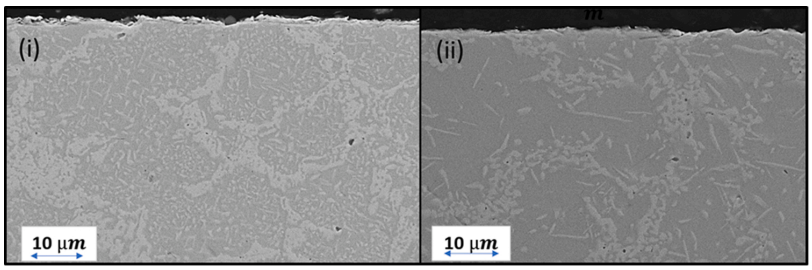

Fig. 2. Untested samples of (i) HEA4 and (ii) HEA5. Mo rich phases (light) and Ni-Fe rich phases (dark) were observed in all six sample types but with different morphology.

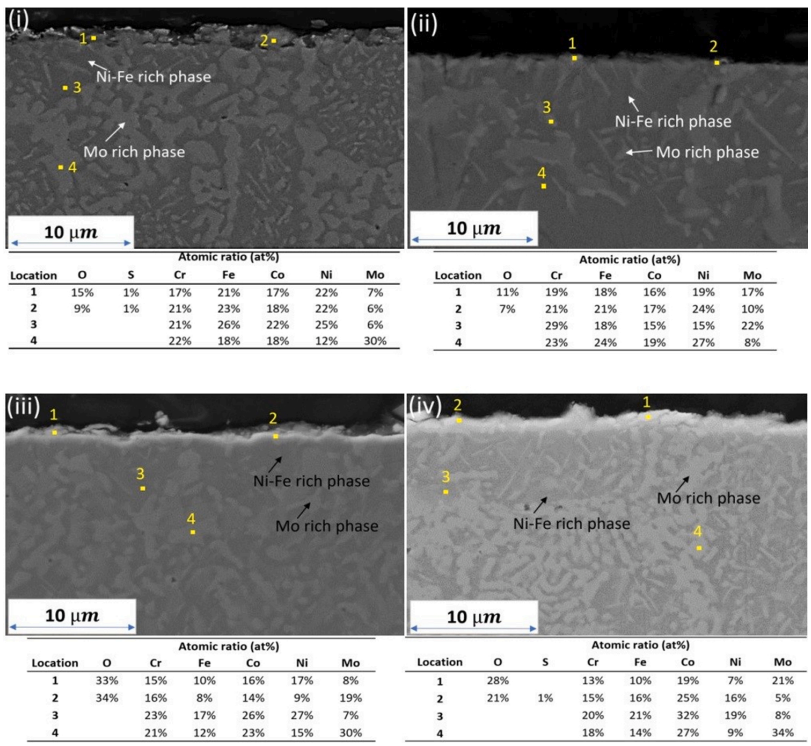

Atomic ratio (at%)

Location	O	S	Cr	Fe	Co	Ni	Mo
1	15%	1%	17%	21%	17%	22%	7%
2	9%	1%	21%	23%	18%	22%	6%
3			21%	26%	22%	25%	6%
4			22%	18%	18%	12%	30%

Atomic ratio (at%)

Location	O	Cr	Fe	Co	Ni	Mo
1	11%	19%	18%	16%	19%	17%
2	7%	21%	21%	17%	24%	10%
3		29%	18%	15%	15%	22%
4		23%	24%	19%	27%	8%

Atomic ratio (at%)

Location	O	Cr	Fe	Co	Ni	Mo
1	33%	15%	10%	16%	17%	8%
2	34%	16%	8%	14%	9%	19%
3		23%	17%	26%	27%	7%
4		21%	12%	23%	15%	30%

Atomic ratio (at%)

Location	O	S	Cr	Fe	Co	Ni	Mo
1	28%		13%	10%	19%	7%	21%
2	21%	1%	15%	16%	25%	16%	5%
3			20%	21%	32%	19%	8%
4			18%	14%	27%	9%	34%

Fig. 3. Cross-section of tested samples of (i) HEA1, (ii) HEA2, (iii) HEA3 and (iv) HEA4.

From the SEM and XEDS analysis of HEA5 and HEA6 seen in Figs. 4 and 5 respectively, it can be observed that localized corrosion damage was observed at the interface of the corrosion film and the bulk alloy. A mixture of oxide and sulphide corrosion products was present in the surface layer of HEA5. In HEA6, mainly copper sulphide corrosion product was formed as an outer layer but with an inner layer which was a mixture of oxide and sulphide as seen in Fig. 6. The sulphide was identified as a Cu_2S phase with the XRD analysis described in the following section. An insignificant concentration of the HEA elements; Co, Cr, Ni, Fe and Mo were analysed in the outer layer of HEA6 but some concentration of the elements was detected in the inner layer with oxygen and sulphide. This result indicated that the porous inner layer consists of mixed sulphides and mixed oxides, and mainly copper-based corrosion products. The inner layer is thus referred to as a complex oxide layer herein in figures and text. The two-layer behaviour was evident as the outer layer was flaking off the inner layer. By analysing HEA6 further at higher magnification it can be observed that the apparent deepest corrosion attack in HEA6 was occurring at the phase boundaries of the Ni-Fe rich phase and the Mo rich phase as can be seen in Fig. 7. This result might indicate that Cu or a Cu rich intermetallic was accommodated preferably in the grain boundaries of Ni-Fe and Mo rich phases, as the main corrosion product was copper sulphide.

To analyse the phase equilibrium, elemental distribution and intermetallic presence in the HEAs, elemental mapping was done in the SEM/XEDS for all the HEAs tested as can be seen in Figs. 8, 9 and 10 . Elemental mapping of the cross-section revealed two main phases present in samples HEA1–HEA6, a Ni-Fe rich phase and Mo-phases. Some unique characteristics were observed for some of the alloys. The passivating oxide film on HEA1 was thicker than the oxide film in all the other HEA samples. Cobalt was more concentrated in the Ni-Fe rich

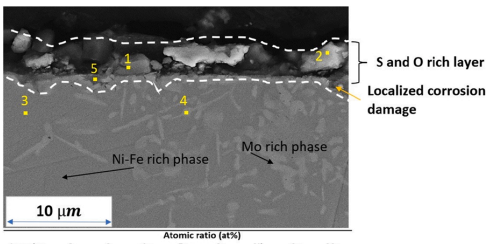

Atomic ratio (at%)

Location	O	S	Cr	Fe	Co	Ni	Cu	Mo
1	7%	32%	2%	4%	5%	23%	24%	2%
2	22%	41%	1%	1%	6%	28%	1%	1%
3			19%	24%	22%	20%	7%	7%
4			22%	19%	20%	13%	3%	23%
5	25%	16%	22%	16%	13%	7%		

Fig. 4. Cross-section of tested HEA5 sample. The surface corrosion layer is rich of S and O and some indications of localized damage at early stages at the bulk alloy surface.

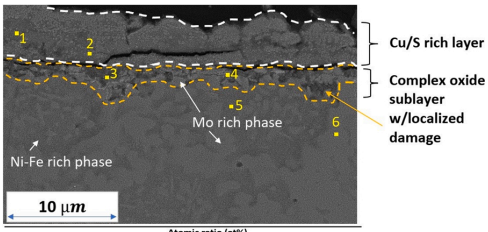

Atomic ratio (at%)

Location	O	S	Cr	Fe	Co	Ni	Cu	Mo
1	5%	31%	2%	1%	1%	1%	60%	
2	2%	33%	1%	1%			64%	
3	21%	19%	8%	5%	3%	2%	35%	7%
4	22%	19%	11%	5%	7%	5%	23%	9%
5			21%	24%	22%	22%	6%	5%
6			28%	18%	19%	10%	1%	25%

Fig. 5. Cross-section of tested HEA6 sample. The outer corrosion layer was rich of S and Cu but the sublayer rich of both S and O. Localized damage occurs at the sublayer in the bulk alloy where the Ni-Fe rich phase corrodes but the Mo rich phase remains coherent with bulk.

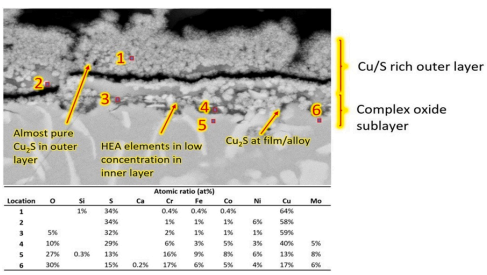

Atomic ratio (at%)

Location	O	Si	S	Ca	Cr	Fe	Co	Ni	Cu	Mo
1		1%	34%		0.4%	0.4%	0.4%		64%	
2			34%		1%	1%	1%	6%	58%	
3	5%		32%		2%	1%	1%	1%	59%	
4	10%		29%		6%	3%	5%	3%	40%	5%
5	27%	0.3%	13%		16%	9%	8%	6%	13%	8%
6	30%		15%	0.2%	17%	6%	5%	4%	17%	6%

Fig. 6. BES image and XEDS analysis of tested HEA6 at high magnification.

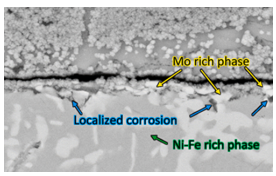

Fig. 7. BES image of tested HEA6. Corrosion attack is observed to be preferential at the Ni-Fe rich phase and Mo rich phase interface.

phase than in the Mo rich phase in all the alloys. Most Mo segregation was observed in HEA2 of HEA1-HEA4 but HEA2 had the lowest Mo content of alloys HEA1-HEA4. This segregation phenomenon in HEA2 could also be explained by low solid solubility of large atomic-size Mo (in comparison with the smaller atomic-sized Ni, Cr, Co and Fe in the HEA lattice), a lattice distortion effect of Mo or some unexpected phase dispersion due to the "cocktail effect" in HEAs. Last but not the least, Cu is homogeneously distributed in HEA5 and HEA6 but some high concentration sites of Cu were observed in HEA6 indicating that the solid solubility of Cu may be exceeded in the Ni-Fe or Mo rich phase lattices or some Cu-rich intermetallic phases have formed in HEA6.

By doing elemental profile scanning through a segment in HEA5 and HEA6 more obvious concentration difference between Cu can be detected as seen in Fig. 11. The Cu concentration in HEA5 was homogeneous whereas concentrated Cu sites were observed in HEA6.

The correlation between Cu and the elements Co, Cr, Fe, Ni and Mo was also examined for HEA6 but the Cu concentration did not correlate with any of the other elements in HEA6 indicating that the Cu concentrated sites were not involved in Ni-Fe or Mo rich phases. However, at phase boundaries, where the concentration of Ni-Fe or Mo was altered significantly, concentration gradients of Cu were observed as can be seen in Figs. 12 and 13 . This observation suggests that the Cu concentrated intermetallic sites occur at the phase boundaries of Ni-Fe and Mo rich phases.

3.2. XRD analysis

X-ray diffractometry analysis of the tested and untested samples showed that some changes in crystal structure had occurred in the HEAs after the testing. The extent of the changes indicated that HEA1-HEA4 were less susceptible to the corrosive environment than the Cu added HEA5 and HEA6 which is in agreement with the SEM/EDS analysis. A reduction in the Ni-Fe phase peaks was observed in the tested samples compared to the untested ones and a new peak appeared at $2\theta = 23^{\circ}$ in HEA1-HEA3, as seen in Fig. 14. This peak could not be identified but most likely corresponds to a crystalline oxide or sulphide compound formed during the corrosion tests, which can aid in protecting the alloy from further corrosion. No new diffraction peaks were seen for the tested HEA4 (the highest Co content of alloys HEA1-HEA4) and the XRD pattern was close to identical to the non-tested specimen. This shows that there was a minimal formation of crystalline corrosion products on HEA4. The high Mo content in HEA3 promotes the formation of a σ phase or (Mo,Cr) rich phase that was identified in the XRD graph in Fig. 14 (iii), which was present both before and after the corrosion testing.

The morphology changes in the Cu added alloys HEA5 and HEA6 are evident from Fig. 15 and 16 respectively. The Fe-Ni phase peaks are significantly reduced, and new peaks emerge, corresponding to hexagonal Cu_2S in alloy HEA5, and hexagonal and tetragonal Cu_2S in alloy HEA6. This is consistent with the presence of a thick copper and sulphide-rich layer analysed on the surface of the samples. The presence of tetragonal Cu_2S on the corroded HEA6 sample might be due to increased Cu content in HEA6 in comparison with HEA5. The extent of the morphology changes was more exaggerated in HEA6 due to the higher Cu content and increased corrosion effect as previously mentioned in the description of the microstructural and chemical analysis results.

4. Discussion

In general, the CoCrNiFeMo alloys, HEA1-HEA4, showed good corrosion resistance in the testing environment. From the results of our testing and assuming linear extrapolation of the corrosion film thickness growth rate, it can be concluded that the general corrosion rate is low (<0.1 mm/year) for alloys HEA1-HEA5 but up to 0.2 mm/year for HEA6, a significantly higher corrosion rate than for corrosion-resistant

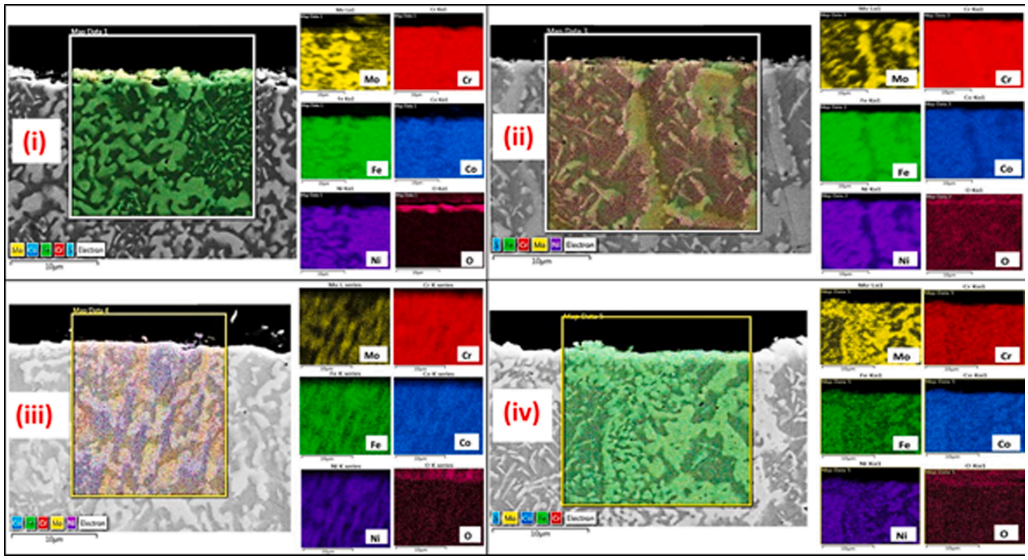

Fig. 8. Elemental mapping of the cross-section of the tested samples (i) HEA1, (ii) HEA2, (iii) HEA3 and (iv) HEA4. More oxide was observed on the surface of HEA1 in comparison with the other alloys.

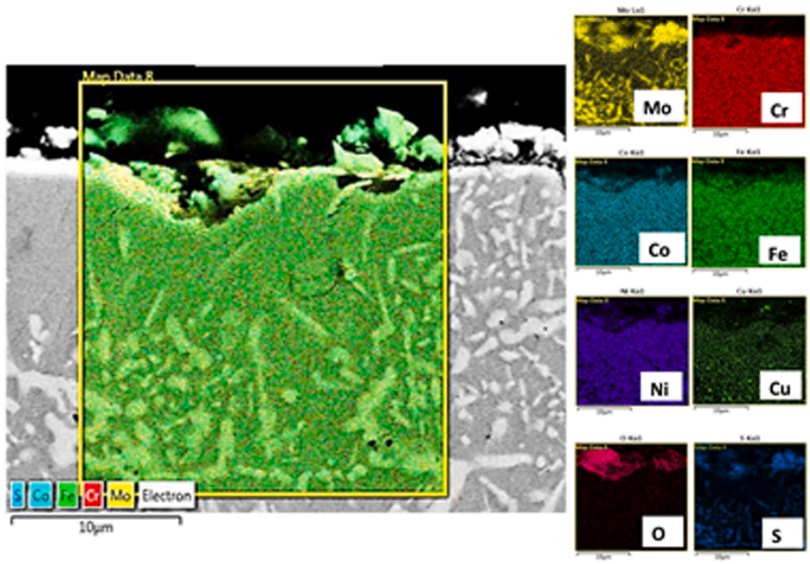

Fig. 9. Elemental mapping of the tested HEA5.

alloys tested in the same simulated superheated geothermal environment [18]. In terms of surface and morphology stability, the XRD patterns for the CoCrNiFeMo alloys were different from un-tested samples indicating the formation of crystalline corrosion products. Equimolar or close equimolar ratios of CoCrFeNiMo alloys produced via arc melting process have face-centred cubic (FCC) solid solutions according to the XRD results which are compliant with results shown by Shun et al. [4]. In the study by Shun et al. it was also concluded that with increasing Mo concentration in HEAs, a σ or (Mo,Cr) rich phase forms and is incorporated in the FCC solid solution of the CoCrFeNiMo alloy. Chou et al. [16] reported that formation of σ phase would reduce the Cr concentration in other phases in a HEA. The Cr-depletion in other phases was concluded to result in lower corrosion resistance in other phases as it is well known that Cr increases corrosion resistance. Due to the high Mo content in the HEA3 alloy, the alloy contained σ phases according to the XRD pattern before and after testing. Increased Mo in $CoCrNiFeMo_x$ alloys has been reported to stabilize and harden the FCC structure due to increased formation of the σ phase [4]. However, studies of equimolar CoCrNiFeMo film coated on a substrate with electro-spark deposition (ESD) have shown that Mo stabilizes the formation of a body centred cubic (BCC) structure in the equimolar CoCrNiFeMo alloy coated with ESD [2]. In the same paper, the bulk material of as-cast equimolar

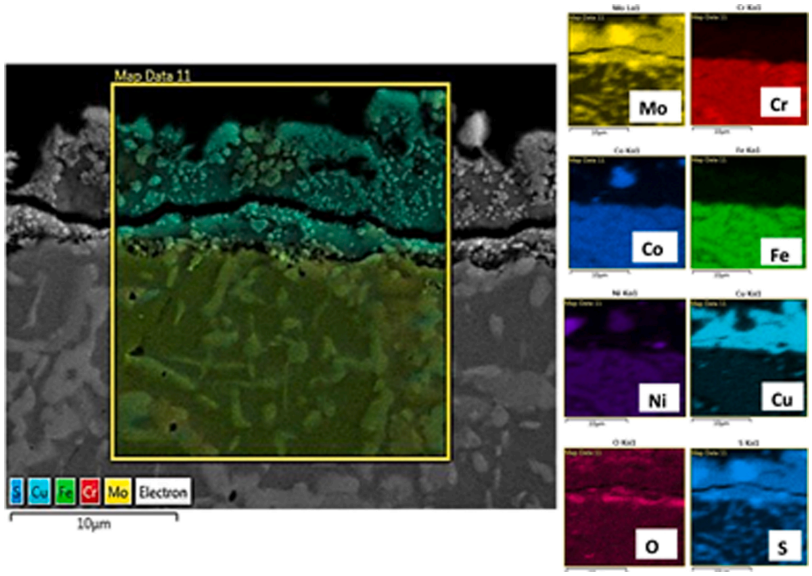

Fig. 10. Elemental mapping of the tested HEA6. The more concentrated and denser sulphur outer layer and concentrated oxide sublayer were observed in the Cu added HEA6 in comparison with the Cu added alloy HEA5.

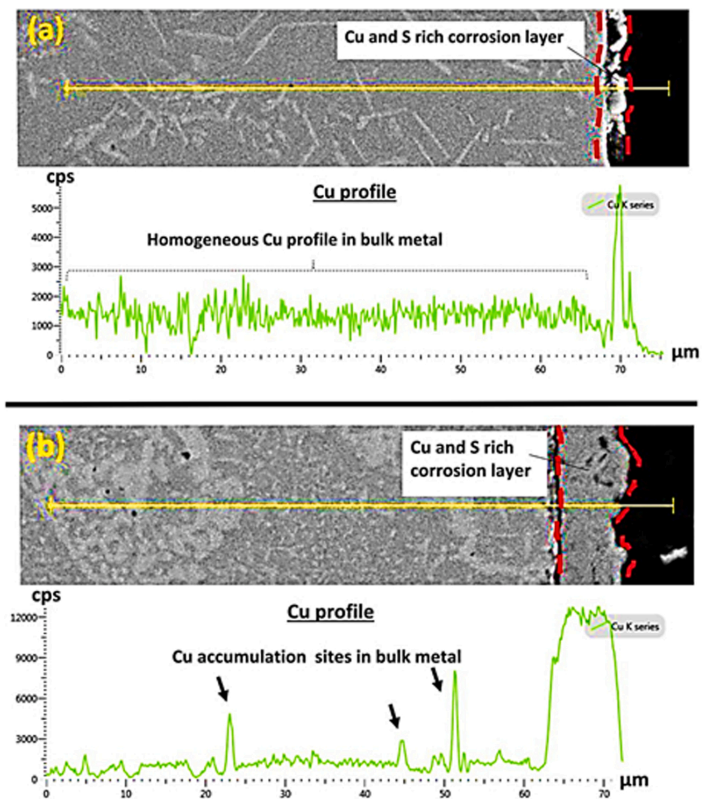

Fig. 11. Cu profile in a) HEA5 and b) HEA6. More segregation of Cu was observed in the higher Cu content HEA6 in comparison with HEA5.

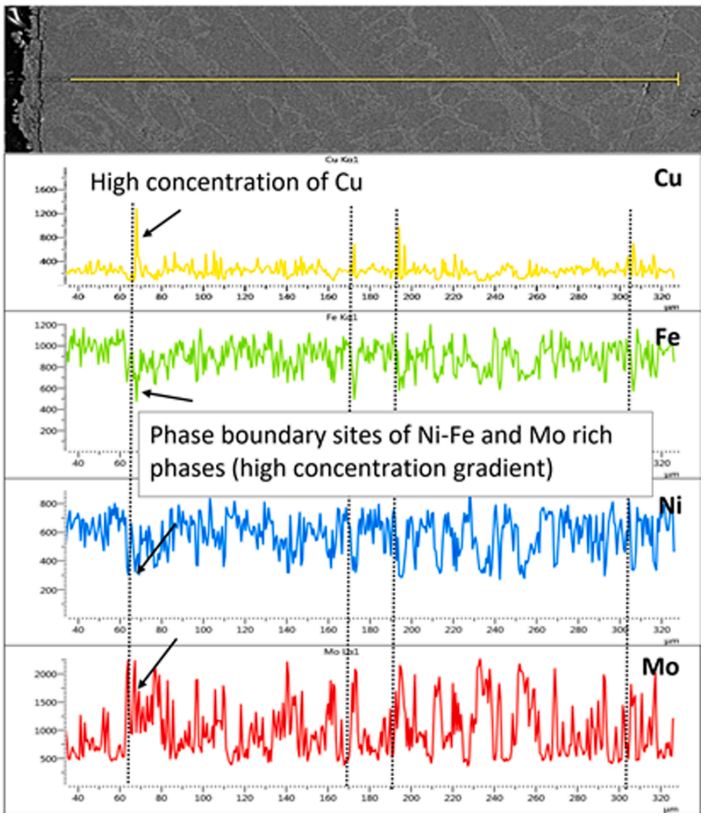

Fig. 12. Correlation between Cu concentrated sites in HEA6 and Ni-Fe and Mo concentration via elemental scanning along the yellow line (top). Cu concentration was high at apparent phase boundaries of Ni-Fe and Mo rich phases. (For interpretation of the references to colour in this figure legend, the reader is referred to the web version of this article.)

CoCrNiFeMo alloy is reported to have no σ phase present which agrees with the results in our testing of the equimolar HEA1 alloy. The effect of the corrosion tests on the surface morphology of alloys HEA1-HEA3 was similar according to the XRD patterns obtained after the corrosion test. In our tests, the crystal structure pattern of the alloy that was most identical before and after testing was HEA4 which was the alloy with the highest Co content of all the alloys tested but equimolar content of Cr, Ni, Fe and Mo. Cobalt, a common alloying element gives an improvement of mechanical properties rather than corrosion resistance properties. Furthermore, in some material production technologies, Co enhances the mechanical properties of HEAs [23]. In HEAs however, Co has been found to enhance the formation of FCC structure in alloys able to form FCC, BCC or FCC + BCC structures at various atomic ratios [24]. With increasing FCC structure and reducing BCC structure, the hardness of the HEA decreases. A lower hardness of HEAs with added Co may limit their application in an environment where hardness of the material and erosion-corrosion is required. However, an increase in Co concentration in HEAs will reduce the concentration of other elements that may increase the corrosion resistance properties such as Cr, Ni and Mo. A study by Niu et al. [25] on electrochemical testing of $CoCrNiFeMo_x$ alloys in seawater where the ratio of Mo was varied has shown that adding Mo increased the corrosion resistance. Furthermore, within the Mo ratio interval x = [0–1], the $CoCrNiFeMo_{0.5}$ alloy had the densest oxide layer and the highest corrosion resistance of the alloys tested. In our testing and observations, it was found that the CoCrNiFeMo alloys were not susceptible to significant corrosion in our testing environment at different alloying ratios. The corrosion rate in a low-density superheated fluid has previously been concluded to be low [18–20,26,27] while another testing has shown that alloys can be susceptible to localized corrosion damage in a superheated fluid [11]. In the previous testing with carbon steel and corrosion-resistant superalloys, only carbon steel was found to be prone to localized damage in superheated steam containing HCl, H_2S and CO_2 according to Thorhallsson et.al [18] but other in-situ testing reported by Karlsdottir et al. [11], with more complex corrosive fluid containing among other species HCl, H_2S, CO_2, H_2 and HF, has shown localized corrosion damage in carbon steels and all the corrosion-resistant superalloys tested.

The CoCrNiFeMoCu alloys (Cu added HEAs; HEA5 and HEA6) were found to be more susceptible to corrosion than the Cu free HEAs (HEA1-HEA4). The Mo-rich phase segregation was apparent and was enhanced in the Cu added HEA5 and HEA6 alloys that might be explained by additional segregation effect of Cu as concluded by Hsu et al. [5]. Several papers have reported some segregation tendency or corrosion susceptibility of Cu added HEAs. Copper rich interdendrite phases in Cu added CoCrFeNi alloys have been reported to be prone to galvanic attack by Cr rich dendrite sites according to Hsu et al. [5] and Lin et al. [28] where also the ageing effect of CoCrFeNiCu HEA was demonstrated at 350 °C. In our testing, the corrosive fluid was a low-density fluid with low electrical conductivity where electrochemical corrosion reactions are expected negligible as discussed by Kritzer [26] and Thorhallson et al. [18]. As a result, a galvanic attack between Cu and other more noble phases was unlikely to occur in our testing conditions. Some

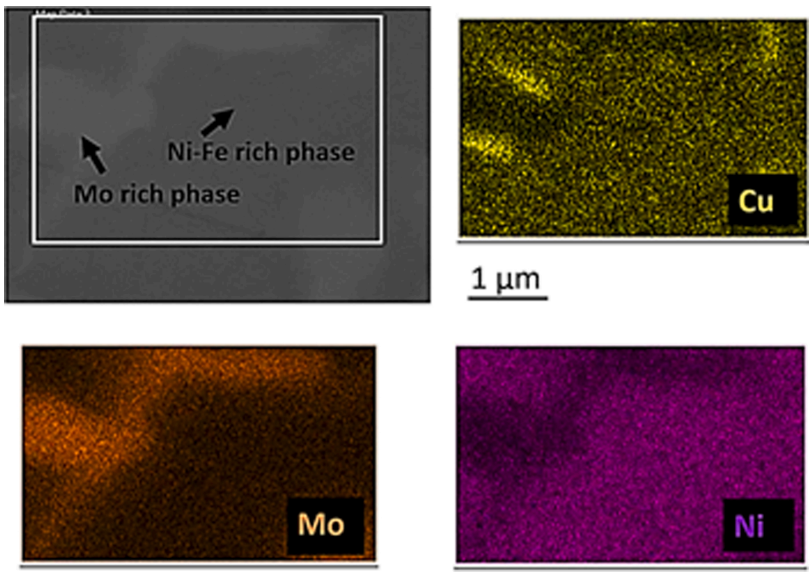

Fig. 13. Magnification of 20.000x in HEA6. Cu concentrated sites (strong yellow) were always observed at the phase boundaries of Ni-Fe and Mo rich phases. (For interpretation of the references to colour in this figure legend, the reader is referred to the web version of this article.)

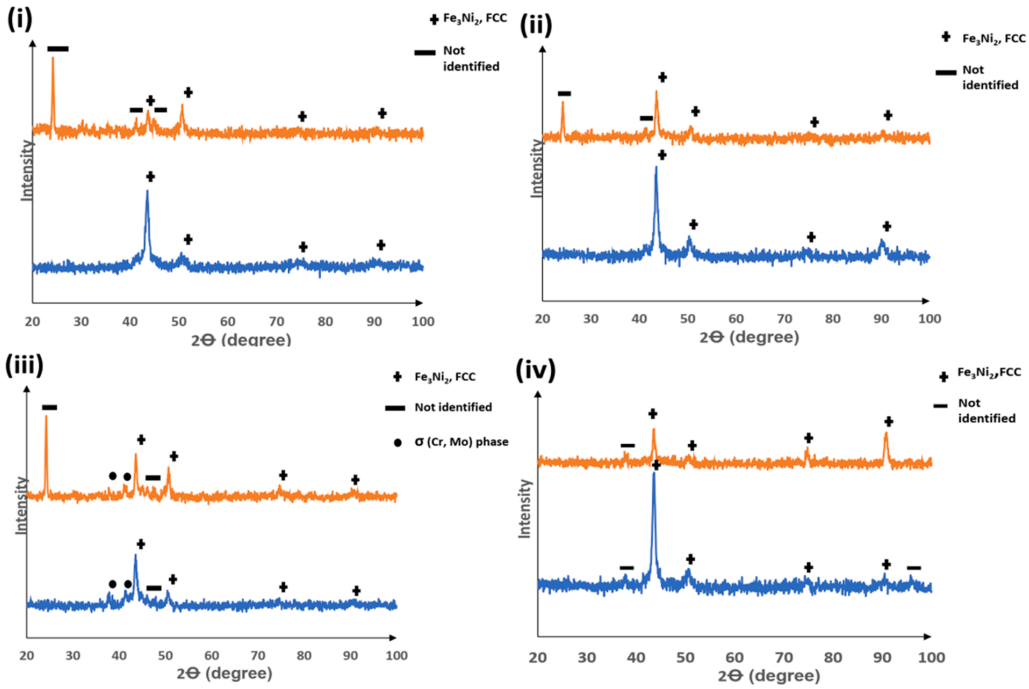

Fig. 14. XRD of tested (orange) and untested (blue) samples of (i) HEA1, (ii) HEA2, (iii) HEA3 and (iv) HEA4. (For interpretation of the references to colour in this figure legend, the reader is referred to the web version of this article.)

ageing effect of the Cu added HEAs during our testing at 350 °C cannot be excluded though. Increased Cu content from HEA5 to HEA6 has the effect that concentrated Cu rich intermetallic sites are forming in the bulk metal of HEA6 which were not observed in HEA5. Increased Cu content enhances Cu segregation that can induce localized corrosion susceptibility in Cu added HEAs as concluded by Hsu et al. [5] and Ren et al. [15]. As a result, increased Cu segregation may be the cause for increased Cu diffusion supply for the corrosive species to react with at or

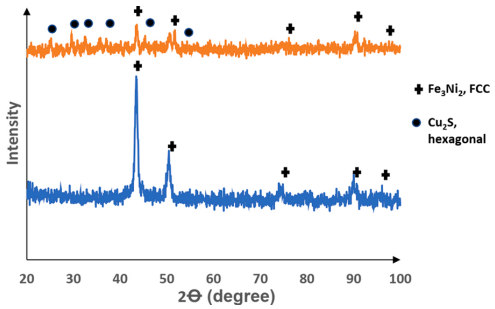

Fig. 15. XRD from tested (orange) and untested (blue) HEA5 samples. (For interpretation of the references to colour in this figure legend, the reader is referred to the web version of this article.)

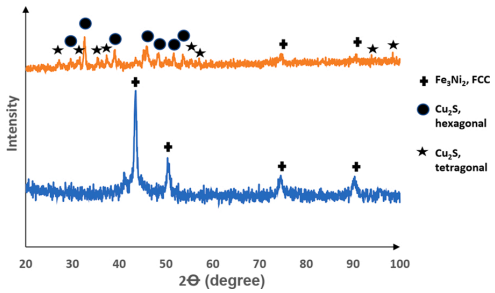

Fig. 16. XRD from tested (orange) and untested (blue) HEA6 samples. (For interpretation of the references to colour in this figure legend, the reader is referred to the web version of this article.)

in the complex oxide surface and hence increased corrosion rate experienced in HEA6 in comparison with HEA5, which was in agreement with the study by Smith et al. [29]. On the other hand, pure Cu has been reported to be susceptible to corrosion in a dry mixed gas environment containing H_2S and H_2O [30]. Tomio et al. [31] and Baba et al. [32] have reported improved corrosion resistance of Cu added corrosion-resistant alloys but no literature was found were Cu addition to HEAs improves corrosion resistance except were γ phases have been formed as described by Nene et al. [14]. Demirkan et al. [30] conducted corrosion testing of pure Cu in a mixed flowing gas at 40 °C. The gases included H_2S, H_2O and other gases. Their result showed rapid corrosion of Cu and formation of porous Cu_2S outer layer and a thin porous Cu_2O inner layer formed in the test. They concluded that Cu diffused from the bulk metal through the porous Cu_2O layer and reacted with the H_2S at the Cu_2O and Cu_2S boundaries. This was explained as a result of the higher diffusion coefficient of Cu in comparison with H_2S through the corrosion film. No conclusion was made on the reaction mechanism of Cu_2O formation. Furthermore, the Cu_2S outer layer tended to flake off from the Cu_2O inner layer in a study conducted by Demirkan et al. [30]. This is consistent with our results; where a copper sulphide outer layer and a complex oxide inner layer were formed on the Cu added HEAs. In addition, the copper sulphide outer layer also tended to flake off the complex oxide layer. The complex oxide film in the HEA6 is likely established partially before the corrosion tests because of the passive behaviour of the HEA alloy. The diffusion of Cu from the bulk HEA alloy, from the Cu rich intermetallic sites and the bulk alloy likely occurs during the corrosion test. The Cu diffuses through the complex oxide layer and reacts with the H_2S at the surface of the complex oxide layer. However, the complex oxide layer is porous which makes the diffusion of gaseous H_2S through the complex oxide layer capable, permitting the reaction of H_2S and Cu also inside the complex oxide layer. The low adhesion or flaking phenomenon can be viewed in SEM and BES images shown previously.

As a result, we conclude that the increased corrosion reactions experienced in the HEA5 and HEA6 during the tests were mainly attributed to the detrimental effects of the Cu in the HEAs. In our testing, the main identified corrosion product of the Cu added HEAs was Cu_2S and complex oxide film between the Cu_2S outer layer and the HEA bulk sample in HEA6. The reaction of gaseous $H_2S_{(g)}$ and solid $Cu_{(s)}$ is thermodynamically feasible at 350 °C and 10 bar gauge. Hence, we conclude that Cu in the CoCrNiFeMoCu is prone to dry gas corrosion with gaseous $H_2S_{(g)}$. The total reaction of Cu and H_2S is following:

$$2Cu_{(s)} + H_2S_{(g)} \rightarrow Cu_2S_{(S)} + H_{2(g)} \quad (1)$$

The oxide layer is likely to have formed partially before the testing due to passivating behaviour of the HEA samples and/or due to oxidation by H_2O reacting with the metallic elements in the HEA sample in the testing as found in a previous study for other metal alloys in similiar testing environment by Thorhallson et al. [18]. As the oxide film is thin and at the surface of the bulk sample of HEA6 we conclude that the oxide film formed first before H_2S corrosion of Cu starts. The oxide film could also destruct and form again during the corrosion process until the oxide formation/destruction reaches equilibrium and as the Cu_2S film grows and the complex oxide have grown to some thicknesses. From the above discussion, we suggest that the mechanism for the corrosion of CoCrNiFeMoCu at high Cu concentration was as follows: oxide formation was initially very fast and occurred before the sulphide scale was formed. The gaseous H_2S diffuses from the corrosive fluid (or through the porous Cu_2S layer formed) towards the HEA alloy or towards the complex oxide film. The H_2S reacts with Cu which diffused rapidly through the oxide or in some cases H_2S might react directly with the Cu in the bulk alloy where the complex oxide layer has defects or due to porosity. The diffusion of Cu from the intermetallic sites through the oxide or direct reaction with Cu in the intermetallic sites was faster than diffusion from the bulk matrix. This increased Cu diffusion rate from intermetallic sites explains higher corrosion rate of HEA6 in comparison with HEA5. The corrosion of the base HEA provides Cu for the Cu_2S or copper sulphide film growth from the junction of the porous complex oxide and the copper sulphide layer as long as H_2S diffusion through the outer copper sulphide layer is not restrained. The proposed mechanism is summarized in Fig. 17.

The concentration of the other HEA elements (Co, Cr, Ni, Fe and Mo) in the Cu added HEAs within the copper sulphide outer corrosion layer is low but is more present in the inner complex oxide layer. This may be explained by the formation of Cu_2S externally on the complex surface oxide and due to sluggish diffusion of the other elements. The sluggish diffusion of elements within HEAs has been reported by Beke and Erdelyi [33] showing slow diffusion in HEAs in comparison with FCC structures on average. Due to slow diffusion within HEAs, it must be assumed that diffusion of elements within the CoCrNiFeMo and CoCrNiFeMoCu alloys in our testing is extremely slow, except for Cu as previously discussed. Negligible chloride-based corrosion products from gaseous HCl was observed on all the HEA samples. In another testing with corrosion-resistant alloys in superheated steam containing HCl, the passive corrosion-resistant alloys tested were not prone to HCl attack [18] but carbon steel was however prone to HCl attack. This result indicates that the HEAs are passive in our testing environment for HCl attack. The diffusion rate of H_2S through the porous complex oxide could also be more rapid than HCl diffusion rate or H_2S reaction rate with copper could also be faster than the reaction rate of HCl with the HEA elements.

5. Conclusions

The corrosion susceptibility of the CoCrNiFeMo alloys, HEA1-HEA4,

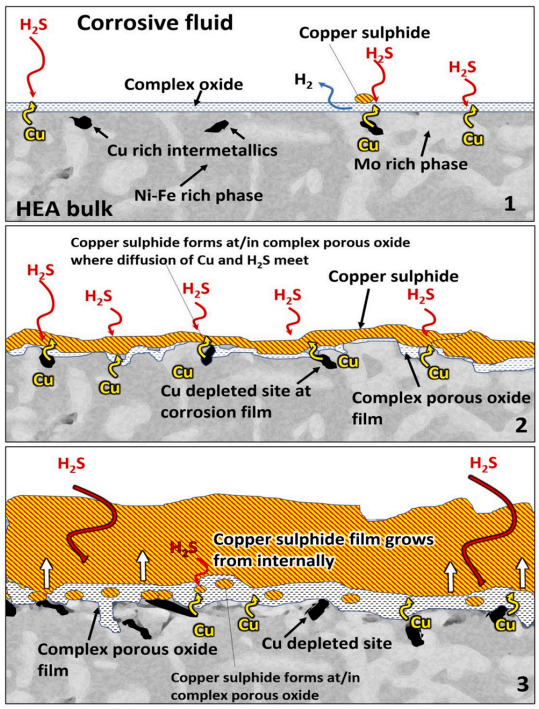

Fig. 17. 1) Cu diffuses through the preformed complex oxide layer. 2) Copper sulphide outer layer forms. 3) Copper sulphide film grows from the complex oxide layer.

was independent of different molar ratios for the alloys tested in our corrosion testing environment. The thickness of the analysed oxide layer differed for the four alloys and the surface crystal structure changed to some extent for all the CoCrNiFeMo alloys tested. Literature review and the results obtained indicate that the HEA2, where the alloy ratio of Mo is close to x = 0.5, might be the most corrosion-resistant HEA of the CoCrNiFeMo alloys tested (HEA1-HEA4). The corrosion rate of the Cu added HEAs, CoCrNiFeMoCu, increases with increasing Cu concentration when exposed to the simulated superheated geothermal environment, where the main corrosion product is Cu_2S. The corrosion is dominated by the reaction between H_2S and Cu. The Cu rich intermetallic phases (at boundaries of Ni-Fe and Mo rich phases) in the Cu added HEAs are the rate-determining factor for the corrosion rate in the tests, due to availability and diffusion of Cu from Cu rich intermetallic phases. In conclusion, the CoCrNiFeMo high-entropy alloys are corrosion resistant in the testing environment and are a candidate for a corrosive geothermal environment, but Cu added HEAs, CoCrNiFeMoCu are not a feasible material in superheated steam containing H_2S. To understand the corrosion resistance of CoCrNiFeMo alloys in more complex superheated or supercritical geothermal fluid, in-situ testing in a fluid containing H_2S, CO_2, HCl and additionally HF, H_2 and SiO_2 is of interest to see if any localized corrosion damage will be observed as observed in corrosion-resistant alloys in previous in-situ testing.

Data availability

The raw/processed data required to reproduce these findings cannot be shared at this time as the data also forms part of an ongoing study.

CRediT authorship contribution statement

Andri Isak Thorhallsson: Conceptualization, Data curation, Formal analysis, Investigation, Methodology, Validation, Visualization, Writing - original draft, Writing - review & editing. **Ioana Csáki:** Conceptualization, Methodology, Writing - review & editing. **Laura Elena Geambazu:** Writing - review & editing. **Fridrik Magnus:** Formal analysis, Writing - review & editing. **Sigrun Nanna Karlsdottir:** Conceptualization, Methodology, Funding acquisition, Supervision, Writing - review & editing.

Declaration of Competing Interest

The authors report no declarations of interest.

Acknowledgements

We want to thank the Icelandic Research Fund (RANNÍS) grants no. 163108-051, 163108-052 and 163108-053 and Geothermal Research Group (GEORG)for funding this project. In addition, we would like to thank employees at Innovation Center of Iceland (ICI) for their technical assistance.

References

[1] I. Csáki, S. Independentei, S.N. Karlsdottir, Corrosion behavior in geothermal steam of CoCrFeNiMo high entropy alloy, (n.d.) 8.
[2] S.N. Karlsdottir, L.E. Geambazu, I. Csaki, A.I. Thorhallsson, R. Stefanoiu, F. Magnus, C. Cotrut, Phase evolution and microstructure analysis of CoCrFeNiMo high-entropy alloy for electro-spark-deposited coatings for geothermal environment, Coatings 9 (2019), https://doi.org/10.3390/coatings9060406.
[3] Y. Zhang, T.T. Zuo, Z. Tang, M.C. Gao, K.A. Dahmen, P.K. Liaw, Z.P. Lu, Microstructures and properties of high-entropy alloys, Prog. Mater. Sci. 61 (2014) 1–93, https://doi.org/10.1016/j.pmatsci.2013.10.001.
[4] T.-T. Shun, L.-Y. Chang, M.-H. Shiu, Microstructure and mechanical properties of multiprincipal component CoCrFeNiMox alloys, Mater. Charact. 70 (2012) 63–67, https://doi.org/10.1016/j.matchar.2012.05.005.
[5] Y. Hsu, W. Chiang, J. Wu, Corrosion behavior of FeCoNiCrCux high-entropy alloys in 3.5% sodium chloride solution, Mater. Chem. Phys. 92 (2005) 112–117, https://doi.org/10.1016/j.matchemphys.2005.01.001.
[6] S.K. Sanyal, J.W. Morrow, Success and the Learning Curve Effect in Geothermal Well Drilling – A Worldwide Survey, (n.d.) 8.
[7] T. Reinsch, P. Dobson, H. Asanuma, E. Huenges, F. Poletto, B. Sanjuan, Utilizing supercritical geothermal systems: a review of past ventures and ongoing research activities, Geotherm. Energy 5 (2017), https://doi.org/10.1186/s40517-017-0075-y.
[8] G. Fridleifsson, W. Elders, The Iceland Deep Drilling Project: a search for deep unconventional geothermal resources, Geothermics 34 (2005) 269–285, https://doi.org/10.1016/j.geothermics.2004.11.004.
[9] T. Hauksson, S. Markusson, K. Einarsson, S.N. Karlsdottir, A. Einarssond, A. Moller, P. Sigmarsson, Pilot testing of handling the fluids from the IDDP-1 exploratory geothermal well, Krafla, NE Iceland, Geothermics 49 (2014) 76–82, https://doi.org/10.1016/j.geothermics.2013.07.003.
[10] H. Armannsson, T. Fridriksson, G.H. Gudfinnsson, M. Olafsson, F. Oskarsson, D. Thorbjornsson, IDDP-The chemistry of the IDDP-01 well fluids in relation to the geochemistry of the Krafla geothermal system, Geothermics 49 (2014) 66–75, https://doi.org/10.1016/j.geothermics.2013.08.005.
[11] S.N. Karlsdottir, K.R. Ragnarsdottir, I.O. Thorbjornsson, A. Einarsson, Corrosion testing in superheated geothermal steam in Iceland, Geothermics 53 (2015) 281–290, https://doi.org/10.1016/j.geothermics.2014.06.007.
[12] S.N. Karlsdottir, K.R. Ragnarsdottir, A. Moller, I.O. Thorbjornsson, A. Einarsson, On-site erosion-corrosion testing in superheated geothermal steam, Geothermics 51 (2014) 170–181, https://doi.org/10.1016/j.geothermics.2014.01.007.
[13] J. Yeh, S. Chen, S. Lin, J. Gan, T. Chin, T. Shun, C. Tsau, S. Chang, Nanostructured high-entropy alloys with multiple principal elements: novel alloy design concepts and outcomes, Adv. Eng. Mater. 6 (2004) 299–303, https://doi.org/10.1002/adem.200300567.
[14] S.S. Nene, M. Frank, K. Liu, S. Sinha, R.S. Mishra, B.A. McWilliams, K.C. Cho, Corrosion-resistant high entropy alloy with high strength and ductility, Scr. Mater. 166 (2019) 168–172, https://doi.org/10.1016/j.scriptamat.2019.03.028.
[15] B. Ren, Z.X. Liu, D.M. Li, L. Shi, B. Cai, M.X. Wang, Corrosion behavior of CuCrFeNiMn high entropy alloy system in 1M sulfuric acid solution, Mater. Corros.-Werkst. Korros. 63 (2012) 828–834, https://doi.org/10.1002/maco.201106072.
[16] Y.L. Chou, J.W. Yeh, H.C. Shih, Effect of molybdenum on the pitting resistance of Co1.5CrFeNi1.5Ti0.5Mox alloys in chloride solutions, Corrosion 67 (2011).
[17] Y.L. Chou, J.W. Yeh, H.C. Shih, The effect of molybdenum on the corrosion behaviour of the high-entropy alloys Co1.5CrFeNi1.5Ti0.5Mox in aqueous

environments, Corros. Sci. 52 (2010) 2571–2581, https://doi.org/10.1016/j.corsci.2010.04.004.
[18] A.I. Thorhallsson, A. Stefansson, D. Kovalov, S.N. Karlsdottir, Corrosion testing of materials in simulated superheated geothermal environment, Corros. Sci. 168 (2020) 108584, https://doi.org/10.1016/j.corsci.2020.108584.
[19] Thorhallsson et al._Corrosion testing of UNS N06625 in simulated HT_C2018-11058.pdf, (n.d.).
[20] Thorhallsson et al._Corrosion testing of UNS S31603 in simulated HT_C2019-13195.pdf, (n.d.).
[21] R. Stefanoiu, V. Geanta, I. Voiculescu, I. Csaki, N. Ghiban, Researches regarding the influence of chemical composition on the properties of AlxCrFeCoNi alloys, Rev. Chim. 65 (2014) 819–821.
[22] T.-T. Shun, C.-H. Hung, C.-F. Lee, Formation of ordered/disordered nanoparticles in FCC high entropy alloys, J. Alloys. Compd. 493 (2010) 105–109, https://doi.org/10.1016/j.jallcom.2009.12.071.
[23] Z.W. Wu, Y.P. Lei, Y. Wang, H.G. Fu, Effect of cobalt content on microstructure and property of electroplated nickel-cobalt alloy coatings, Mater. Werkst. 44 (2013) 593–600, https://doi.org/10.1002/mawe.201300069.
[24] V. Kukshal, A. Patnaik, I.K. Bhat, Effect of cobalt on microstructure and properties of AlCr1.5CuFeNi2Cox high-entropy alloys, Mater. Res. Express 5 (2018), https://doi.org/10.1088/2053-1591/aaba5f.
[25] Z. Niu, Y. Wang, C. Geng, J. Xu, Y. Wang, Microstructural evolution, mechanical and corrosion behaviors of as-annealed CoCrFeNiMox (x=0, 0.2, 0.5, 0.8, 1) high entropy alloys, J. Alloys. Compd. 820 (2020), https://doi.org/10.1016/j.jallcom.2019.153273.
[26] P. Kritzer, Corrosion in high-temperature and supercritical water and aqueous solutions: a review, J. Supercrit. Fluids 29 (2004) 1–29, https://doi.org/10.1016/S0896-8446(03)00031-7.
[27] Morten Tjelta_Corrosion and scaling in DGW_NACE2019_C2019-13299.pdf, (n.d.).
[28] C.-M. Lin, H.-L. Tsai, H.-Y. Bor, Effect of aging treatment on microstructure and properties of high-entropy Cu0.5CoCrFeNi alloy, Intermetallics 18 (2010) 1244–1250, https://doi.org/10.1016/j.intermet.2010.03.030.
[29] J. Smith, Z. Qin, F. King, L. Werme, D.W. Shoesmith, Sulfide film formation on copper under electrochemical and natural corrosion conditions, Corrosion 63 (2007) 135–144, https://doi.org/10.5006/1.3278338.
[30] K. Demirkan, G.E. Derkits Jr., D.A. Fleming, J.P. Franey, K. Hannigan, R.L. Opila, J. Punch, W.D. Reents Jr., M. Reid, B. Wright, C. Xu, Corrosion of Cu under highly corrosive environments, J. Electrochem. Soc. 157 (2010) C30–C35, https://doi.org/10.1149/1.3258288.
[31] A. Tomio, M. Sagara, T. Doi, H. Amaya, N. Otsuka, T. Kudo, Role of alloyed copper on corrosion resistance of austenitic stainless steel in H2S-Cl- environment, Corros. Sci. 81 (2014) 144–151, https://doi.org/10.1016/j.corsci.2013.12.013.
[32] K. Baba, D. Mizuno, K. Yasuda, H. Nakamichi, N. Ishikawa, Effect of Cu addition in pipeline steels on prevention of hydrogen permeation in mildly sour environments, Corrosion 72 (2016) 1107–1115, https://doi.org/10.5006/2013.
[33] D.L. Beke, G. Erdelyi, On the diffusion in high-entropy alloys, Mater. Lett. 164 (2016) 111–113, https://doi.org/10.1016/j.matlet.2015.09.028.

Journal Article 3

A.I. Thorhallsson, S.N. Karlsdottir, Corrosion Behaviour of Titanium Alloy and Carbon Steel in a High-Temperature, Single and Mixed-Phase, Simulated Geothermal Environment Containing H_2S, CO_2 and HCl, Corros. Mater. Degrad. 2 (2021) 190–209. https://doi.org/10.3390/cmd2020011.

corrosion and materials degradation

MDPI

Article

Corrosion Behaviour of Titanium Alloy and Carbon Steel in a High-Temperature, Single and Mixed-Phase, Simulated Geothermal Environment Containing H_2S, CO_2 and HCl

Andri Isak Thorhallsson * and Sigrun Nanna Karlsdottir

Faculty of Mechanical Engineering, Industrial Engineering and Computer Science, University of Iceland, Hjardarhagi 2-6, 107 Reykjavik, Iceland; snk@hi.is

* Correspondence: ath196@hi.is; Tel.: +354-8423144

Abstract: The corrosion behaviour of a new titanium-based alloy, with nickel, molybdenum and zirconium as the main alloying elements, was studied in a simulated geothermal environment at various phase conditions of a corrosive fluid. Corrosion testing of carbon steel was also conducted for comparison. Both materials were tested at an elevated temperature between 180 and 350 °C and at a 10 bar gauge pressure in H_2O containing HCl, H_2S, and CO_2 gases with an acidic condensate of pH = 3. The study found that the titanium alloy demonstrated good corrosion resistance in a single- and multiphase geothermal environment. In the testing volume, where the boiling of testing fluid occurred, the carbon steel was prone to localized damage of oxide, sulphide and chloride corrosion products. In the superheated testing volume, a homogeneous oxide corrosion layer was observed on the carbon steel. In the testing volume where condensation of the testing fluid occurred, a sulphide layer with an oxide sublayer was formed on the carbon steel.

Keywords: titanium alloy; carbon steel; H_2S; CO_2; HCl; multiphase; corrosion; high-temperature; geothermal

Citation: Thorhallsson, A.I.; Karlsdottir, S.N. Corrosion Behaviour of Titanium Alloy and Carbon Steel in a High-Temperature, Single and Mixed-Phase, Simulated Geothermal Environment Containing H_2S, CO_2 and HCl. *Corros. Mater. Degrad.* **2021**, 2, 190–209. https://doi.org/10.3390/cmd2020011

Academic Editor: Angeliki G. Lekatou

Received: 25 March 2021
Accepted: 26 April 2021
Published: 29 April 2021

1. Introduction

The application of titanium and titanium-based alloys as a structural and process equipment material in the geothermal industry has received growing attention in the last few decades due to its excellent corrosion resistance, which exceeds that of the more conventional steels and stainless steels [1]. Titanium alloy corrosion resistance is due to the protectiveness of a passive TiO_2 surface film that forms in various corrosive environments [2–5]. The main limitation to titanium application in the geothermal industry is considered to be its high cost and the de-rating of mechanical properties at high temperatures [6]. Nogara and Zarrouk have summarized results from different corrosion tests of various titanium alloys for geothermal energy application, but none of the tests included titanium alloys with nickel, molybdenum and zirconium as the main alloying elements. Schutz et al. [7] reported that nickel and molybdenum are thought to enhance the corrosion resistance of the TiO_2 passive film and increase the mechanical strength of the titanium alloy at high temperatures. Zirconium has been reported to enhance the mechanical stability of β-phase (body centred cubic (BCC)) titanium in a Nb- and Zr-based alloy [8–10] and enhance the passivity and corrosion resistance [11] (up to 50 wt.% Zr) of titanium alloys for biomedical applications. Increased corrosion resistance and mechanical strength at high temperatures are required if a titanium alloy is to be used in a geothermal environment. In this paper, the corrosion behaviour of a new titanium-based alloy (with nickel, molybdenum and zirconium as the main alloying elements), will be studied in a simulated geothermal environment at various phase conditions of the corrosive fluid from 180 to 350 °C at 10 bar gauge.

In the geothermal power production industry, material in a down-hole geothermal well and surface equipment can be subjected to critical corrosion damage, which increases maintenance costs and limits the lifetime of the well, thus affecting power production efficiency. The degree of corrosion damage depends on several factors, including the corrosion resistance of the materials, and the chemical composition and phase state of the geothermal fluid as summarized by Nogara and Zarrouk [12–14]. The corrosive geothermal fluid consists mainly of H_2O as steam with other corrosive species such as H_2S and CO_2 (aqueous, gas or mixed-phase state) depending on the chemical composition of the fluid, the pressure and the temperature. The chemical composition and the phase state of the corrosive geothermal fluid affect the corrosion rate and behaviour of the material exposed to the corrosive geothermal fluid [15–18]. The phase state of the corrosive fluid affects its ionic activity, which strongly depends on the density of the fluid at high-temperature or in aqueous solutions [19,20]. As a result, for a fluid with a fixed chemical composition and containing H_2O with corrosive species, dissimilar corrosion rates and behaviours can be expected for materials exposed to the fluid in a liquid state under high pressure (due to the high ionic activity of an aqueous solution) and corrosion in superheated steam under low pressure (due to the low ionic activity of the gas phase). Different corrosive behaviours can also be expected in saturated-liquid and saturated-vapour conditions since, as discussed by Liu et al., corrosion is more likely to occur in the saturated liquid state [21]. For liquid solutions containing salts, boiling the liquid can leave concentrated salt residuals on the surface that can induce under-deposit corrosion, as discussed by Yang et al., for Ni-based alloys and stainless steels tested in supercritical water [22].

To simulate the corrosion behaviour of materials in different phase state scenarios (i.e., corrosive environments), in the geothermal energy production field, a corrosion testing flow-through reactor setup was used in this study. Previous trials and tests were conducted using a single corrosion testing reactor setup. The results indicated that condensation and boiling occurred in a scheduled gas-phase fluid environment [23], affecting the corrosion rate and corrosion forms in the testing samples in the single reactor. In a further attempt to homogenize the testing conditions, three flow-through reactors were connected in series where the first reactor was applied as a preheater. Several corrosion trials were conducted in this new setup, but results still indicated inhomogeneous conditions in the testing volume [24]. This was concluded from different corrosion behaviours in the samples in different locations in the testing volume. Thorhallsson et al. reported that further adjustments and modifications eventually led to homogeneous corrosion behaviour in the second and third reactor since the first reactor was only used as a preheater [15].

The objective of this study was to map the phase state of the corrosive fluid in three reactor-based testing volumes and investigate the corrosion behaviour of a titanium alloy (Ti-0.4Ni-3.6Mo-0.75Zr) and carbon steel in a single and multiphase corrosive fluid during a simulated geothermal testing environment. The corrosion testing was conducted in boiling, superheated and condensation conditions, and the three-reactors were connected in series. The first and the second reactors were set at 350 °C and the third reactor at 180 °C. All were under 10 bar gauge pressure. The corrosive fluid used in the simulated high-temperature geothermal environment was water containing HCl, H_2S and CO_2 gasses with a pH of 3 at room temperature.

2. Materials and Methods

2.1. Simulated Geothermal Test Fluid

The testing fluid was formed by the reaction of two aqueous reactant solutions in the mixing point. One solution contained $HCl_{(aq)}$ and the other contained anhydrous $Na_2S_{(aq)}$ and $NaHCO_{3(aq)}$. The solution was prepared by titrating sulphide with mercury acetate with a dithizone indicator and back titrating CO_2 according to Arnorsson [25]. When the reactant solutions were mixed, hydrochloric acid reacted with the two species in the other reactant solution to form H_2S and CO_2 with NaCl and H_2O as by-products. After mixing, the concentration of H_2S and CO_2 was 150 ppm and 250 ppm, respectively with a pH of

3. The flow rate and pH were measured after the outlet of the third reactor (cold volume). The H_2S and CO_2 were collected regularly at the outlet and inlet to verify the chemical composition of the fluid, which was eventually neutralized in an alkaline (NaOH) solution containing zinc acetate. The concentration of the reactants in each solution can be seen in Table 1.

Table 1. Concentration of the reactant species in the reactant solutions.

Parameter	Value	Unit
Reactant Solution 1		
HCl	31	mmol
Total volume	1000	mL
Reactant Solution 2		
Na_2S	8.8	mmol
$NaHCO_3$	11.4	mmol
Total volume	1000	mL

2.2. Testing Facility and Conditions

The two reactant solutions in separate mixing flasks were connected by PVC tubes to Labhut degassers and from there to Chromtech Series I high-pressure pumps, which injected the two fluids at the mixing junction before the inlet of the testing volume where the testing fluid was formed. The expected scenario of the testing fluid condition and phase transition inside the testing volume was as follows: The testing fluid flowed into the first reactor with a set temperature of 350 °C where the fluid was heated from room temperature to the saturation point of the testing solution, where it is completely evaporated to vapour-phase state. As the fluid was almost pure H_2O, the expected saturation point was near 184 °C at 10 bar gauge [26]. The density of pure H_2O vs. temperature at 10 bar gauge can be seen in Figure 1 [27].

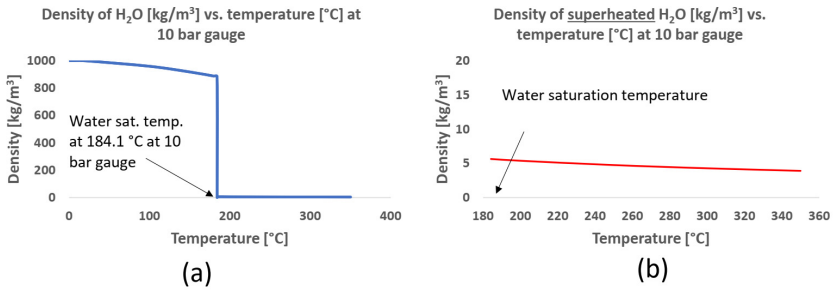

Figure 1. Density of pure H_2O at 10 bar gauge from (**a**) 0 to 350 °C and (**b**) at superheated conditions (>184.1 °C).

In the rest of the testing volume in the first reactor, the solution was heated past the saturation point to the superheated state. When the testing fluid entered the second reactor at 350 °C, the fluid maintained the superheated condition. Piping without insulation connected the second and third reactor allowing the testing fluid to lose heat to the environment, cooling down to lower temperatures. The third reactor had a set temperature of 180 °C, where condensation of the testing fluid was expected. The first and second reactor were insulated externally with glass wool, and to ensure efficient heat loss from the third reactor no external insulation was applied from the outlet of the second reactor to the outlet of the third reactor. A water cooling jacket was connected to the outlet pipe of the third reactor which condensed and cooled all the testing fluid. The heating tape that had been applied in earlier setups to ensure superheated conditions at the outlet of the third reactor was now excluded. After the condenser, the back-pressure regulator was

connected to the test flow line. The cold and condensed testing fluid was then inserted into a chemical waste bin where the toxic H_2S was neutralized with alkaline zinc acetate. The tubing between reactors and the tubing in the hot temperature volume in the testing facility was made of UNS N10276 (American Special Metals, Pompano Beach, FL, USA), the same material used in the reactor tubes. The sample holder and fasteners were made of Inconel UNS N06625 (Velvik, Reykjavik, Iceland). Ceramic alumina (Ortech, Sacramento, CA, USA) washers were inserted between the testing samples and the fasteners to prevent a galvanic coupling effect. The hot-part assembly (heaters, reactors and insulation surrounding the reactor pipes and heating elements) were custom made at the University of Iceland. Electrical parts for the heater were provided by Rafhitun ehf (Hafnarfjordur, Iceland). The temperature in the system was monitored with K-type thermocouples connected to a U6 datalogger (Labjack, Lakewood, CA, USA). The pressure in the test flow line was measured at the outlet of the condenser with S-20 digital pressure transducer (WIKA, Klingenberg, Germany) which was connected to the U6 datalogger. An analog pressure gauge meter was also connected at the outlet of the condenser. The pressure in the testing volume was regulated by a custom made back pressure regulator provided by Prologo (Kopavogur, Iceland) and the pressure set value was controlled with a SITEC 750 hand pump (SITEC, Maur, Switzerland). The testing facility design can be seen in Figure 2.

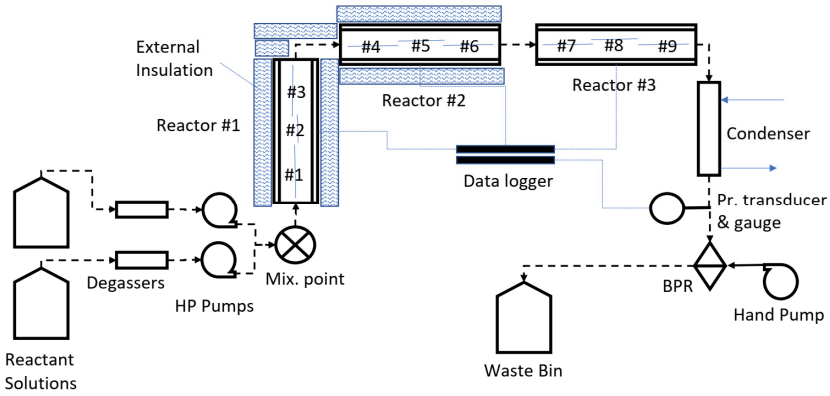

Figure 2. Flow diagram of the three reactors, flow-through testing facility. Three samples were accommodated in each reactor.

The physical and chemical composition of the testing fluid is summarized in Table 2:

Table 2. Physical conditions and chemical composition of testing fluid.

Parameter	Value	Unit
pH	3	-
Temperature—Reactor 1	350	°C
Temperature—Reactor 2	350	°C
Temperature—Reactor 3	180	°C
Fluid pressure	10	bar
Cl	35.5 *	mg/kg
CO_2	250	mg/kg
H_2S	150	mg/kg

* Calculated at pH = 3.

A more detailed description of the testing facility and pre and post-testing procedures is described by Thorhallsson et al. [15], the main differences in this study being the set temperature and insulation of the third reactor as described earlier.

2.3. Testing Materials and Testing Period

The materials tested in this study were carbon steel S235JRG2 (Salzgitter, Salzgitter, Germany) and the titanium alloy (TIMET, Warrensville Heights, OH, USA); Ti-0.4Ni-3.6Mo-0.75Zr or TIMETAL® 475 (Ti-475). A UNS number has not yet been assigned to this alloy. The alloy was tested in the annealed condition. The carbon steel and titanium alloy were tested in separate batches. In each material testing batch, three flat coupons were accommodated in all the three reactors. In each one, two coupons had dimensions 100 mm × 7 mm × 1–2 mm and one shorter coupon was placed between the two longer samples with a dimension of 50 mm × 7 mm × 1–2 mm. To summarize, in each testing batch, 9 samples of each material were tested with the sample number designated according to Figure 2: samples 1–3 were tested in reactor 1; samples 4–6 in reactor 2; and samples 7–9 in reactor 3. In light of the experience by Jonsson [23] where the carbon steel was prone to a high corrosion rate, it was decided to test it for only 3 days in this study. The testing period of the titanium alloy, summarized in Table 3, was 10 days. The chemical composition of the carbon steel and titanium-based alloy is given in Table 4.

Table 3. The testing periods for the two testing materials.

Material Type	Alloy	Test Period (Days)
Carbon steel	S235JRG2	3
Ti-based alloy	Ti-0.4Ni-3.6Mo-0.75Zr	10

Table 4. Chemical composition of the testing materials.

Material	UNS Number	Other Designation	Nominal Composition (% wt)											
			C	Si	Mn	Cr	Ni	Mo	Cu	Al	O	Ti	Zr	Fe
Carbon steel	N/A	NS-EN S235JRG2 (ASTM A 284C)	0.04	0.02	0.2	0.04	0.02	-	0.04	0.04	-	-	-	balance
Titanium-based alloy	N/A	Ti-0.4Ni-3.6Mo-0.75Zr	-	-	-	-	0.44	3.43	-	-	0.16	bal.	0.74	0.18

The titanium alloy has potential application in the field of geothermal power production as a downhole, casing material. The geothermal application of titanium casing is well known to be limited due to the low mechanical strength of titanium alloys at elevated temperatures. However, the mechanical properties of the titanium alloy Ti-0.4Ni-3.6Mo-0.75Zr fulfil the requirements for minimum casing strength for a corrosion-resistant alloy (CRA) according to the API 5CRA standard [28] as seen in Table 5.

Table 5. Mechanical properties of Ti-0.4Ni-3.6Mo-0.75Zr.

Mechanical Properties *	Annealed	Heat-Treated	Unit
Yield Strength (YS, 0.2%)	552	758	MPa
Ultimate Tensile Strength (UTS)	758	896	MPa
Ductility EL (%)	29	10	%
Ductility RA (%)	57	30	%

* Minimum values.

2.4. Sample Preparation and Weight Loss Analysis

All the samples were ground to 600 grit with SiC abrasive paper, cleaned in ethanol with an ultrasound bath then weighed and measured. The measured corrosion rate (CR) of the material tested in mm/year was calculated via the weight loss method and according to the ASTM G1-90 standard [29]

$$CR = \frac{K \cdot W}{A \cdot t \cdot \rho} \quad (1)$$

where K is the corrosion rate constant equal to $8.76 \cdot 10^4$ mm/year; W is the mass loss in grams of the tested material with a precision of ± 0.00005 grams; A is the exposed surface area in cm^2 of a tested sample; t is the exposure time in hours; and ρ is the material density of the material in g/cm^3. The density of the materials was 7.85 and 4.68 g/cm^3 for carbon steel and the titanium alloy, respectively. The alloy was not cleaned due to the unavailability of standard cleaning procedure for titanium alloys in ASTM G1-90.

2.5. Post Exposure Measurements and Analysis

Microstructural analysis was done on the sample surfaces and several cross-sections. Samples 2, 3, 4, 6, and 7 were selected for surface analysis and then used in weight loss analysis. Samples 1, 5, 8 and 9 were selected for cross-sectional analysis for the carbon-steel samples. The same procedure was done for the titanium alloy except for sample 8, which was applied to the weight loss analysis but not the cross-sectional analysis. As boiling of the testing fluid was expected in the first few centimetres in reactor 1 and condensation was expected in the last few centimetres at the outlet of reactor 3, these samples were selected for cross-sectional analysis under a Supra 25, Scanning Electron Microscope (Zeiss, Oberkochen, Germany). For elemental analysis under X-ray Electron Dispersive Spectroscopy (XEDS) from Oxford Instruments (Abingdon, UK), samples were sectioned, ground and polished with colloidal silica to a final 0.02–0.06 µm particle size. Pre- and post-analysis of the samples were conducted. The XEDS instrument had a Si(Li) X-ray detector and AZtec software (version 3.3). Surface and cross-sectional analysis of samples were also analysed with Meiji Techno´s MT7530OH optical microscope (Somerset, UK) with Infinity Analyze software (version 6.5.7). The crystal structure of the materials and corrosion products were analysed in situ by an X-ray Diffractometer before and after corrosion tests with an XPert Pro XRD diffractometer (Malvern Panalytical, Malvern, UK) with Data Collector software (version 1.3).

3. Results and Discussion

3.1. Visual Inspection, Microstructural and Chemical Analysis

The carbon-steel samples had turned from shiny metal to black in appearance after the corrosion test as seen in Figure 3, but the titanium alloy samples showed only small discolourization after the testing.

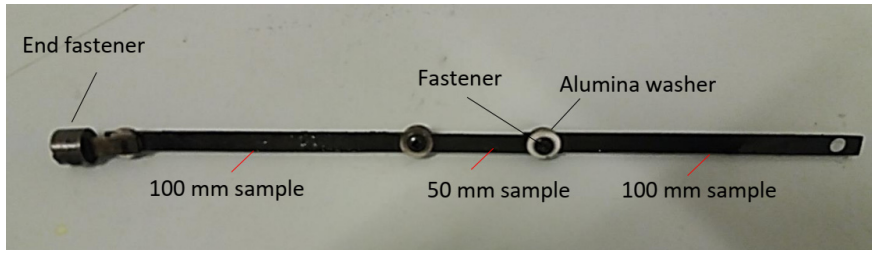

Figure 3. The carbon-steel samples in reactor 2 after the testing. All the carbon-steel samples in all three reactors had turned from shiny metal appearance to black appearance after the corrosion test.

Further visual inspection of the carbon-steel samples after the corrosion testing indicated that some corrosion had occurred on sample 1 at the inlet of the first reactor and sample 9 at the outlet of the third reactor. This observation was evident from the bulk mass removal effect and pitting on the surface; a lower corrosion effect was observed on the samples between these two samples. This observation was strengthened under an optical microscope where the thickness reduction was apparent in a cross-sectional view of the first and last sample in comparison with other samples tested as can be seen in Figure 4.

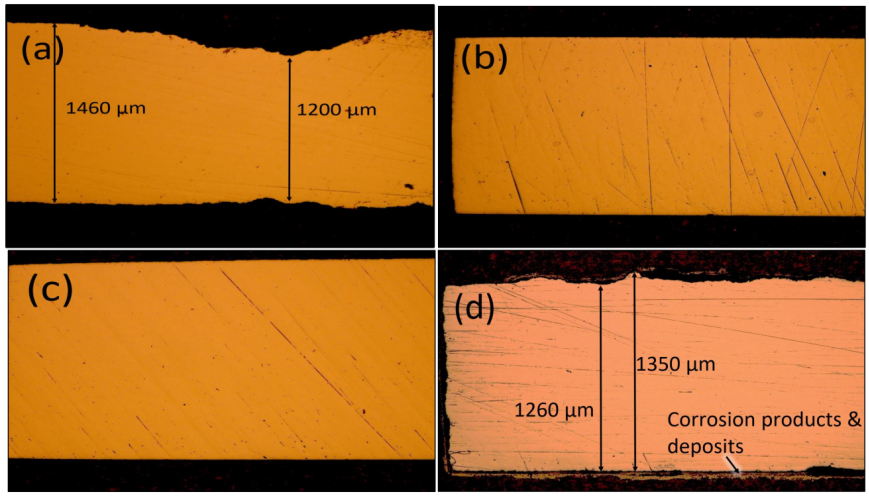

Figure 4. Optical microscope (5× magnification) of a carbon-steel sample cross-section (**a**) 1 cm from the inlet end of sample 1, (**b**) 3 cm from the inlet end of sample 1 in the first reactor, (**c**) In the middle of sample 5 in the second reactor and (**d**) one cm from the outlet end of sample 9 in the third reactor.

A surface analysis of all the carbon-steel samples showed that corrosion to some extent had occurred on the first few centimetres of sample 1 and sample 9. The first 1 to 2 cm of sample 1 had been prone to apparent corrosion, where part of the samples had been corroded away during the test. The corrosion observed on sample 9 had more micropitting texture rather than bulk mass removal. The samples in between had, to a large extent, surface texture similar to the surface texture characterized by the presence of magnetite (see Figure 5 and Table 6). This had been observed in other corrosion tests performed in the same testing equipment (but with different setup) in a superheated environment done by Thorhallsson et al. [15]. A broad range of corrosion forms was observed on the carbon-steel sample in the first few centimetres of sample 1: some locations had negligible oxide film observed on the surface; other locations had a dense oxide film present.

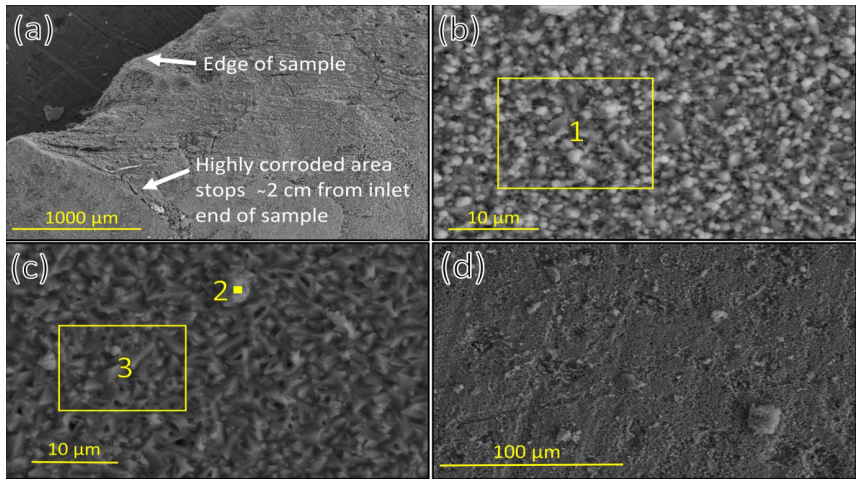

Figure 5. (**a**) Tested carbon-steel sample 1 only one cm from inlet end in the first reactor, (**b**) tested carbon-steel sample 1 now three cm from inlet end in reactor 1, (**c**) tested carbon-steel sample 5 in middle of the second reactor and (**d**) tested carbon-steel sample 9 at the outlet of the last reactor.

Table 6. Elemental analysis from locations in Figure 5.

Location	Element (wt.%)						
	O	**Na**	**Si**	**S**	**Cl**	**Fe**	**Ni**
1	23.8	1.0	0.3	0.3	0.6	73.1	0.9
2	23.4	1.7	0.4	0.3	0.7	73.6	
3	31.6	1.2	0.2	0.7	0.4	65.3	0.6

These findings might indicate that wet (aqueous) corrosion could have occurred at the first few centimetres and at the last centimetre in the testing volume because of boiling at the inlet and condensation at the outlet. Elemental analysis of carbon-steel samples indicated that some corrosion products from the fasteners or the reactor pipes (nickel-based alloy) had likely been transported to the surface of the corroded carbon-steel samples because Ni and Mo were sometimes observed on the corroded samples as seen in Figure 5 and Table 7 (and in Figure 4 and Table 6). When the cross-section of the samples in the three reactors was studied, some corrosion behaviour variability was observed: the first few centimetres of sample 1 had an incident of corrosion damage both where carbon-steel material residuals inside the corrosion film were observed on the sample (Figure 6 and Table 7), and another incident where the thicker corrosion product (oxide film) was observed on the sample (Figure 7 and Table 8). The surface profile indicated in both cases that severe corrosion damage had occurred.

Table 7. Elemental analysis from locations in Figure 6.

Location	Element (wt.%)						
	O	**Al**	**Si**	**S**	**Ca**	**Fe**	**Mo**
1	39.8	0.3	0.4	0.1	-	59.2	0.3
2	-	0.8	0.9	-	-	98.3	-
3	21.2	0.3	0.6	0.3	0.4	77.2	-
4	31.0	-	0.6	0.5	0.6	67.3	-

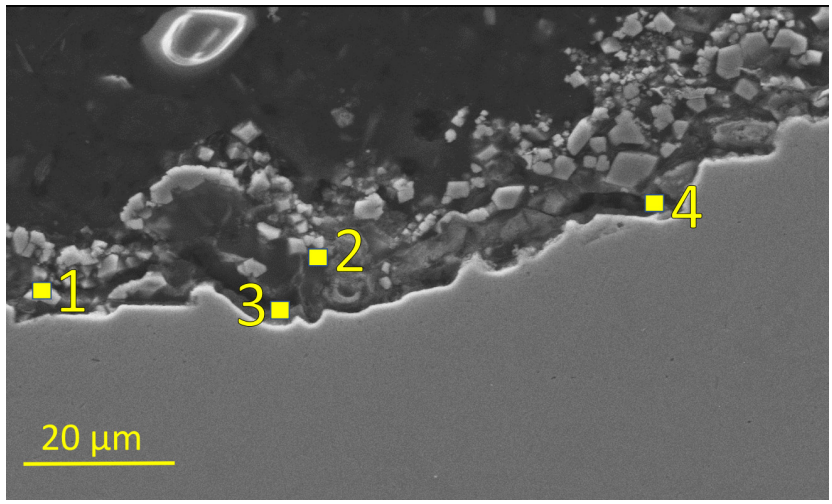

Figure 6. Cross-section of tested carbon-steel sample 1 one cm from the inlet of the first reactor.

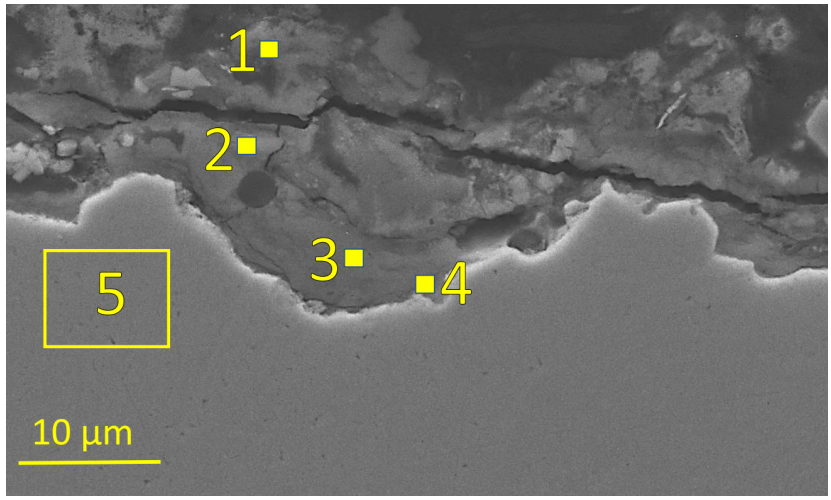

Figure 7. Cross-section of tested carbon-steel sample 1 one cm from the inlet of the first reactor. A continuous oxide layer was observed.

Table 8. Elemental analysis from locations in Figure 7.

Location	Element (wt.%)							
	O	Na	Al	Si	S	Cl	Ca	Fe
1	34.9	1.2	-	0.5	0.4	1.1	0.6	61.3
2	43.1	1.4	0.2	0.2	0.3	0.4	0.5	53.9
3	36.5	1.0	-	0.3	0.2	0.4	0.3	61.3
4	15.9	-	0.5	0.3	-	-	0.3	83.1
5	-	-	-	-	-	-	-	100.0

Further into the testing volume or 3 cm from the inlet of the first reactor, the form of the corrosion products changed to a more consistent or homogeneous texture, i.e., chloride rich pits under oxide film were observed more consistently than in the first 1 to 2 cm of sample 1 as can be seen in Figure 8.

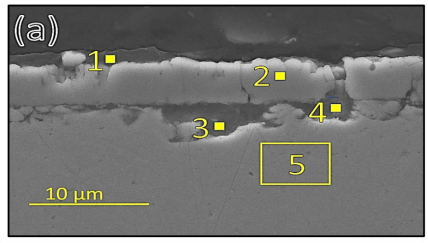

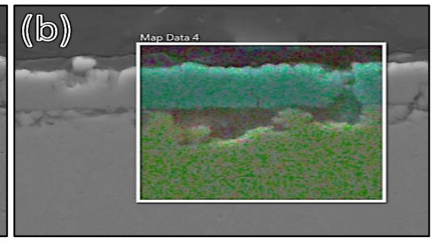

Location	Element (wt.%)				
	O	Si	S	Cl	Fe
1	34.2				65.8
2	21.4	0.2	0.3	3.2	75.0
3	21.4	0.2	0.3	3.2	75.0
4	28.7		0.2	0.8	70.3
5					100.0

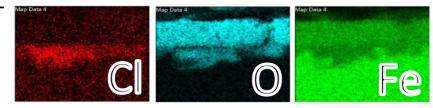

Figure 8. Cross-section of tested carbon-steel sample 1, three cm from the inlet of the first reactor with (**a**) localized chemical analysis and (**b**) elemental scanning.

These findings might indicate that the transition from acidic aqueous solution to vapour phase fluid occurred at the first few centimetres of sample 1. The corrosion of carbon steel in an acidic H_2S environment at low and high temperatures showed that the carbon steel was prone to general and localized corrosion damage with an inner magnetite (Fe_3O_4) layer and outer iron sulphide layer in the corrosion film as reported by Gao et al. [30–32] in an aqueous environment. A study by Choi et al. showed that H_2S can have an inhibiting effect on the corrosion of carbon steel in an acidic CO_2/H_2S environment at 25 °C [33], and Mursalov addressed the multifactor dependence and complexity of corrosion of H_2S in an acidic environment [34]. The lack of an observed sulphide layer in our testing in the first few centimetres of carbon-steel sample 1 might have been due to the very high acidity of the testing fluid, which dissolved the sulphide layer, or to the high concentration of sodium chloride deposits on the corrosion samples that prevented sulphide formation by forming a mass transfer barrier at the surface when the testing fluid boiled in the first few centimetres of the first reactor. Furthermore, the kinetics of iron sulphide layer formation is slow in comparison to those of magnetite formation as concluded by Gao et al. [31]. In the sulphide layer formation process, magnetite layer forms first and iron sulphide then forms gradually in an acidic H_2S environment at 120 °C. The lack of sulphide film in the first few centimetres of sample 1 could, therefore, have been due to the synergistic effect of slow sulphide-formation kinetics, or to the effect of an enriched concentration of corrosive species and salt deposits on the surface due to boiling of the testing fluid in the first few centimetres of sample 1. The stability of iron sulphide layers, summarized by Gao et al. [31], showed that the stability of the sulphides was reduced significantly below pH = 4 and was dependent on the reduction potential of the environment. In light of our testing results, low pH = 3 in our testing environment, and the lack of an iron sulphide layer in the corrosion product film, it was likely that the iron sulphide(s) corrosion products were not stable in the aqueous testing environment in the first few centimetres in the first reactor. A low concentration of sodium chloride was, however, detected in the corrosion products in the first few centimetres of sample 1. It likely occurred after the testing period because of the flushing of deionized water through the testing volume after the testing period (to prevent acidic condensation at high temperatures) and before the samples were removed from the reactor. The sodium chloride deposited due to boiling likely dissolved in the flushing water after the testing period and was flushed away with the deionized water through the testing volume at the end of the experiment. The loss of material and the lack of corrosion film on the surface in the first few centimetres of sample 1 indicated that the acidic aqueous solution at high temperature caused the removal of the corrosion products at a rapid rate. The results also indicate that, further into the first reactor, the fluid became less corrosive and the corrosion behaviour trended towards a more localized corrosion attack, as observed in previous study by Thorhallsson et al., for materials tested in superheated conditions [15]. The corrosion behaviour observed for carbon-steel sample 5 in the second reactor resembled the corrosion behaviour observed for sample 1 after the first few centimetres. The exception was that less chloride was detected in the pits in sample 5 in the second reactor and in sample 8 in middle of the third reactor, as seen in Figure 9, Table 9 and Figure 10 and Table 10, respectively.

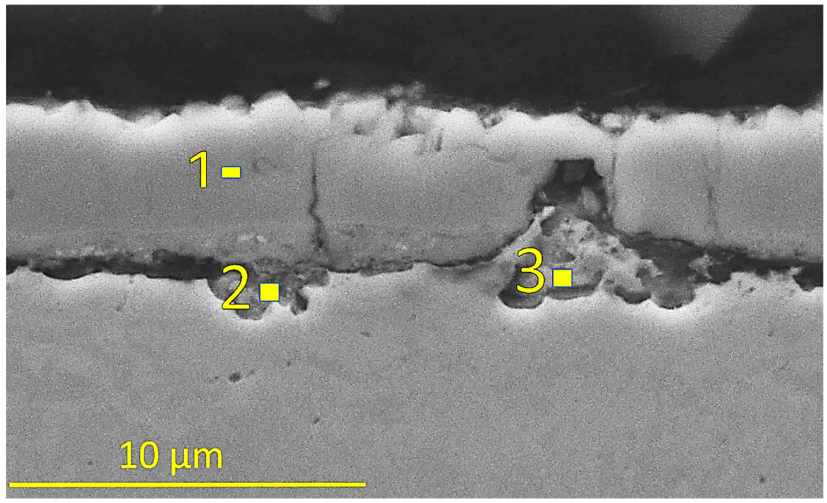

Figure 9. Cross-section in the centre of the tested carbon-steel sample 5 in the middle of the second reactor.

Table 9. Elemental analysis from locations in Figure 9.

Location	Element (wt.%)				
	O	Si	S	Ca	Fe
1	29.9	0.4			69.8
2	25.0		0.2	0.3	74.5
3	23.4		0.2	0.2	76.2

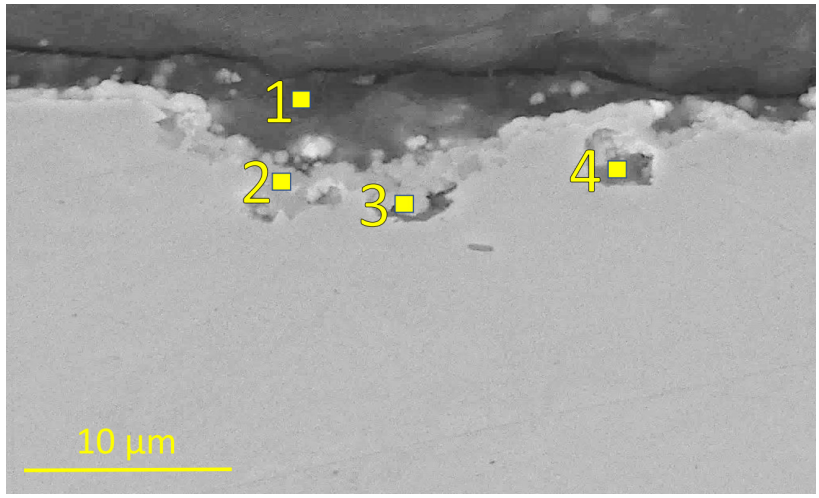

Figure 10. Cross-section in the centre of the tested carbon-steel sample 8 in the middle of the last reactor (condenser).

Table 10. Elemental analysis from locations in Figure 10.

Location	Element (wt.%)				
	O	Ca	Cl	Fe	Ni
1	18.4	0.2	-	81.4	-
2	25.4	-	-	72.1	2.5
3	30.8	-	0.6	68.5	-
4	13.7	-	2.1	84.3	-

This might also have indicated that the less non-volatile NaCl by-products were transported further into the testing volume. The corrosion products in the superheated testing volume (second reactor) did have a small concentration of sulphide corrosion products or a sulphide-rich layer which Thorhallsson et al. saw to a greater extent in the previous test [15]. This difference in the extent of sulphide formation could have been attributed to a shorter test period of the carbon steel, i.e., three days of testing in this study compared to 10 days in the previous testing. This observed difference in corrosion behaviour might indicate that the formation of the sulphide layer is a slow process in the superheated fluid containing H_2S.

The corrosion behaviour of the carbon steel started to change again in the last sample in the third reactor where the set temperature was 180 °C. The corrosion in sample 9, three centimetres from the outlet, had a corrosion film with multiple layers. In comparison with samples 2–8, some sulphur was detected in the corrosion layers of sample 9, three centimetres from the outlet as seen in Figure 11 and Table 11.

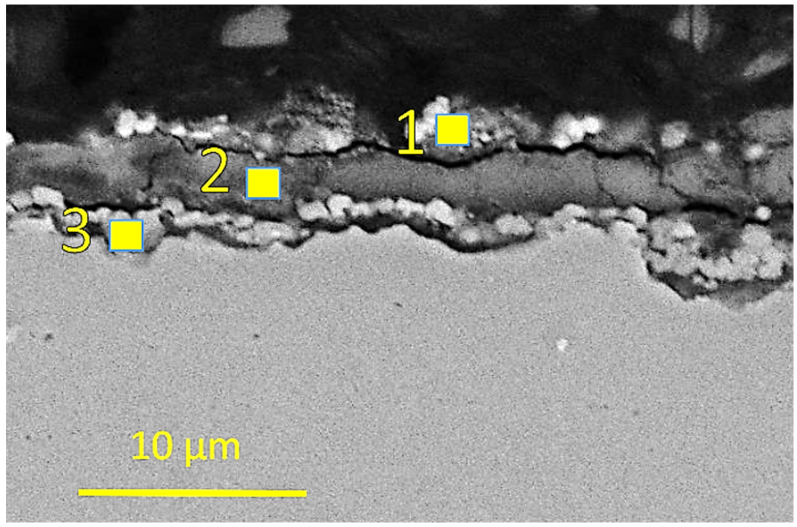

Figure 11. Cross-section 3 cm from the outlet end of tested carbon-steel sample 9 at the end of the last reactor (condenser).

Table 11. Elemental analysis from locations in Figure 11.

Location	Element (wt.%)							
	O	Si	S	Cl	Ca	Fe	Mo	Ni
1	23	0.7	-	0.5	0.5	73.6	1.9	-
2	23.3	0.8	0.6	0.5	0.9	72.8	-	1.1
3	22.6	0.3	0.2	0.2	0.2	76.4	-	-

The transition to multiple-layer corrosion film behaviour became more apparent in the last centimetre of sample 9 in the third reactor. A sulphide-rich outer layer and an oxygen-rich sublayer formed, which was in an agreement with other study results of H_2S corrosion of carbon steel in an aqueous environment at high temperatures [30,31] (See Figure 12).

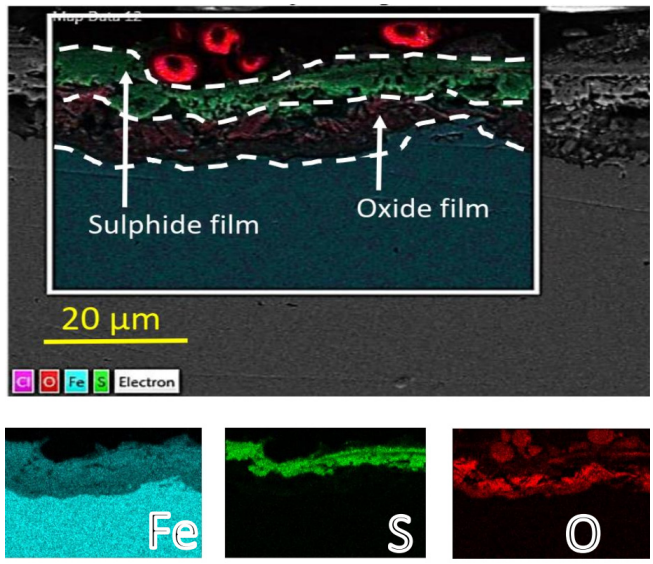

Figure 12. Elemental scanning of cross-section 1 cm from the outlet end of tested carbon-steel sample 9 at the end of the last reactor (condenser).

The difference between the corrosion products observed on the carbon steel in the first few centimetres of sample 1 in the first reactor (where the boiling of the testing fluid likely occurred) and those of sample 9 in the last reactor (where condensation of the testing fluid occurred) could be due to different pH conditions and the concentration of the corrosive species (HCl, H_2S and CO_2) in the testing fluid. The effect of the deposited NaCl by-product in the boiling and NaCl enrichment in the testing fluid in the first few centimetres of the first reactor was also another factor that likely affected the corrosion mechanism, which led to different corrosion behaviour in the testing volume, where boiling and condensation presumably occurred.

The same test setup was applied to testing the titanium-alloy samples. The appearance of the cross-section of the titanium-alloy samples after testing indicated that no corrosion damage was experienced as seen in Figure 13.

Microstructural and chemical analysis in the SEM with XEDS confirmed the optical microscopy result: no corrosion damage was observed in any of the titanium-based samples tested. Some sulphur deposits were analysed on the surface of the samples and some corrosion products from the washers and the fastener/tubing in the testing equipment, but no indication of localized corrosion damage or general corrosion was observed. A denser oxide layer was observed in sample 5 in the superheated testing volume, indicating that the kinetics of TiO_2 film growth on the surface could be a temperature-dependent mechanism even though the titanium oxide growth rate was constant at high temperatures as reported by Kumagai et al. [35]. Microstructural and elemental analysis of both surface and the cross-section of the titanium alloy samples can be seen in Figure 14 (with Table 12), Figure 15 (with Table 13), Figure 16 (with Table 14) and Figure 17. Titanium and titanium alloys are known to perform well in various corrosive environments [36,37], which is consistent with results observed in this study.

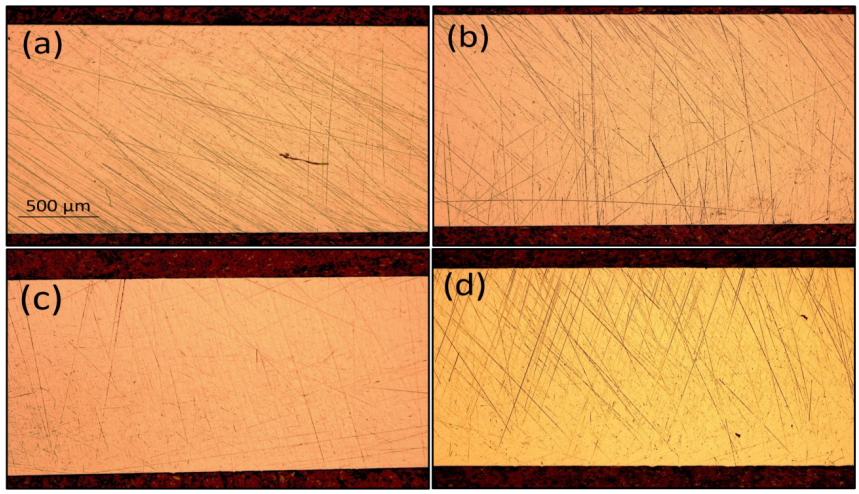

Figure 13. Optical microscope images of the cross-section of the titanium alloy sample (5× magnification); (**a**) 1 cm from the inlet end of sample 1, (**b**) 3 cm from the inlet end of sample 1 in the first reactor, (**c**) In the middle of sample 5 in the second reactor and (**d**) 1 cm from the outlet end of sample 9 in the third reactor.

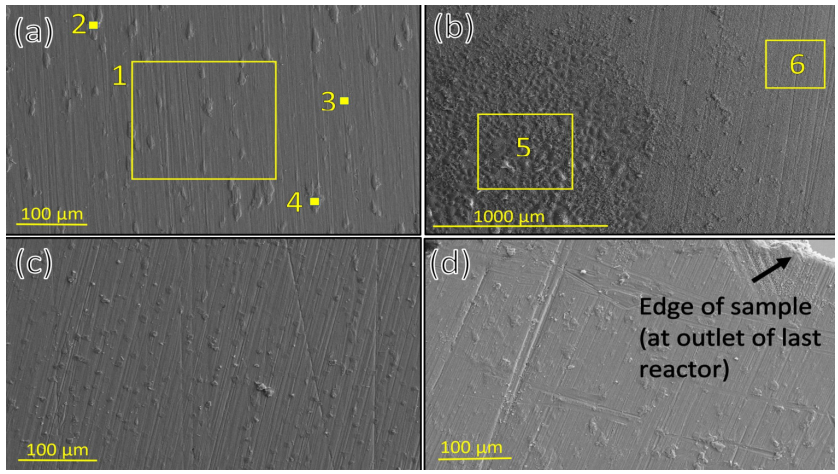

Figure 14. SEM images of the surface of; (**a**) the untested titanium-based alloy, (**b**) the tested titanium alloy sample 1, 1 cm from the inlet end in the first reactor, (**c**) tested titanium alloy sample 1 3 cm from the inlet end of the first reactor and (**d**) tested titanium alloy sample 9 at the end of the last reactor.

Table 12. Elemental analysis from locations in Figure 14.

Location	Element (wt.%)								
	O	S	Si	Ti	Cr	Fe	Ni	Zr	Mo
1	4.9	-	0.2	90.4	-	-	0.4	0.6	3.5
2	12.9	-	0.3	82.6	-	-	0.3	0.7	3.2
3	-	-	-	95.0	-	-	0.3	0.6	4.0
4	15.7	-	3.4	76.7	-	-	0.4	0.8	3.1
5	4.5	65.1	-	15.6	0.9	12.7	1.3	-	-
6	-	36.3	-	23.8	1.3	31.3	2.3	-	5.0

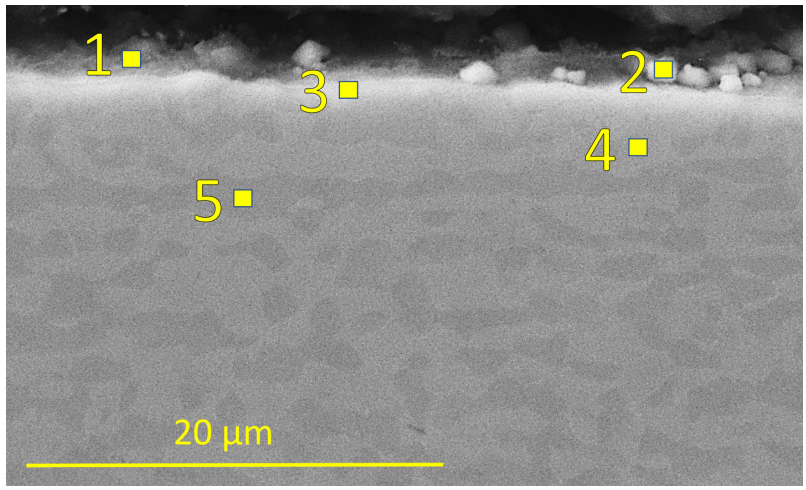

Figure 15. SEM and XEDS analysis of the cross-section of tested titanium alloy sample 1 at 1 cm from the inlet end of the first reactor.

Table 13. Elemental analysis from locations in Figure 15.

Location	Element (wt.%)													
	O	Na	Mg	Al	Si	S	K	Ca	Ti	Cr	Fe	Ni	Zr	Mo
1	31.6	2.2	0.4	0.5	1.2	6.3	0.2	2.0	53.2	0.6	1.3	0.5	-	-
2	-	1.1	-	0.2	0.4	41.1	-	0.3	21.9	-	34.9	-	-	-
3	7.4	-	-	-	-	0.9	-	0.2	91.5	-	-	-	-	-
4	5.4	-	-	-	-	-	-	-	88.4	-	-	0.6	0.8	4.9
5	4.8	-	-	-	-	-	-	-	-	-	-	93.6	0.7	0.9

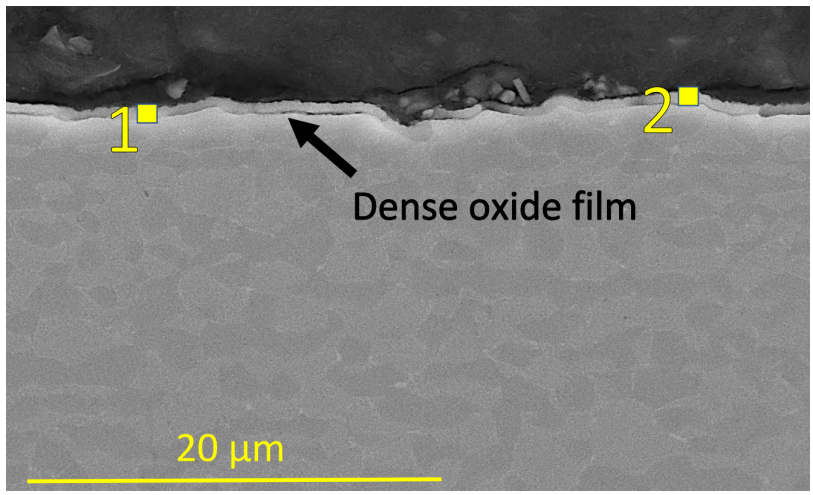

Figure 16. SEM image and XEDS analysis of a cross-section of the middle part of the tested titanium alloy sample 5 in the middle of the second reactor (superheated fluid).

Table 14. Elemental analysis from locations in Figure 16.

Location	Element (wt.%)							
	O	**Al**	**Si**	**Ca**	**Ti**	**Zr**	**Fe**	**Mo**
1	34.8	0.4	0.6	0.4	59.2	0.7	-	3.8
2	34.6	0.5	0.6	0.5	60.5	-	0.5	3.0

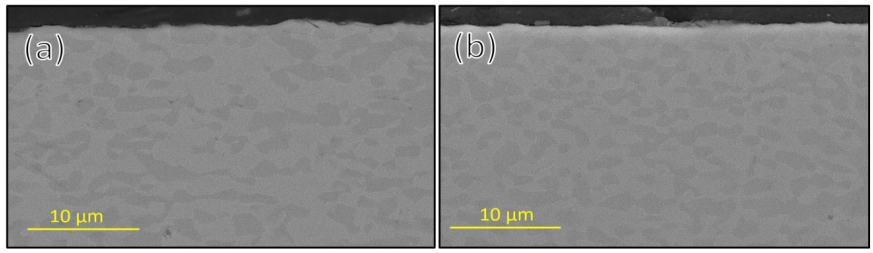

Figure 17. SEM and XEDS analysis of the cross-section of tested titanium alloy sample 9 (**a**) middle of sample 9 and (**b**) one cm from outlet end in the last reactor.

3.2. Weight Loss Analysis

Samples 2, 3, 4, 6, and 7 were used for weight-loss analysis for the tested carbon-steel material. The weight loss, and hence the calculated corrosion rate in the samples accommodated in the first and second reactors, had a corrosion rate of the same order of magnitude as the carbon steel tested in a superheated environment in a study by Thorhallsson et al. [15]. The first sample in the third reactor had a corrosion rate an order of magnitude higher than all other weight loss samples in the first and second reactor as can be seen in Figure 18. The increased corrosion rate of sample 7 in the third reactor might indicate that condensation of the testing fluid started at the inlet of the 3rd reactor, resulting in rapid electrochemical corrosion.

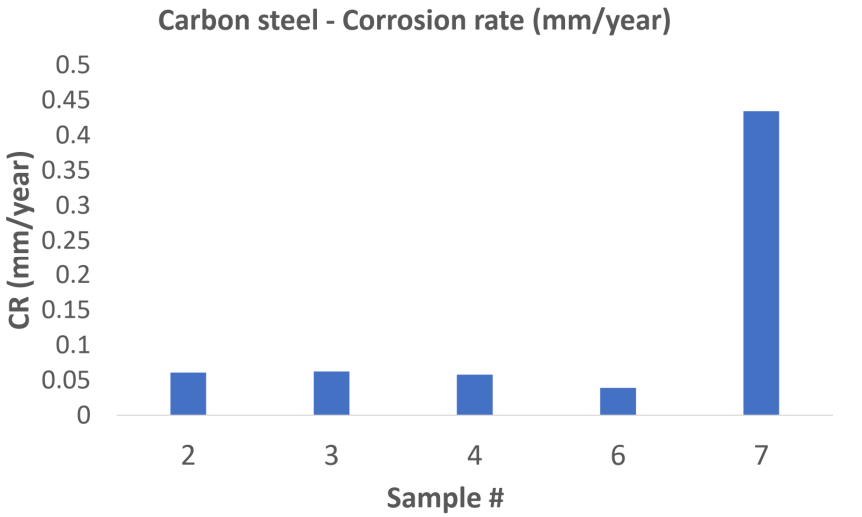

Figure 18. Weight loss analysis of carbon-steel samples. Samples 2 and 3 were accommodated in the 1st reactor, samples 4 and 6 in the 2nd reactor and sample 7 in the 3rd reactor.

As described earlier, the titanium-alloy samples were only cleaned by ethanol in an ultrasonic bath due to the extremely adherent titanium oxide film that formed. Samples

2 and 3 in the first reactor, sample 4 and 6 in the second reactor and samples 7 and 8 in the third reactor were used for weight-loss analysis. Only a negligible weight gain was observed for all the titanium samples except for sample 8, which had a weight loss of 0.001 mm/year, which was insignificant. The weight gain of titanium alloys, however, was well known due to the growth of the titanium dioxide film during exposure.

3.3. XRD Analysis

It was necessary to evaluate the XRD results of the untested and corrosion-tested carbon steel in connection with the state of the fluid and with the SEM and XEDS results, which showed that the liquid state or condensation of the testing fluid occurred at the inlet of the first reactor (sample 1) and in all the volume of the third reactor (sample 9). From the XRD pattern of the surface of sample 1, the crystalline phases detected were the body-centred cubic (BCC) system with iron (Fe) and the cubic crystal system with iron oxide in the form of magnetite (Fe_3O_4). The samples in the proposed superheated testing volume, samples 2–5, had magnetite detected on the surface, but in sample 8 the transition from magnetite as a surface covering to an exposed BCC–Fe bulk material likely occurred. Sample 9 then had peaks of BCC–Fe crystal structure identified. From the Pourbaix diagram of iron at high temperatures [38], it was concluded that magnetite is not stable or present in an acidic (pH < 4) aqueous solution. Since the peaks for magnetite were not present in the XRD pattern for samples 1 and 9, it further strengthened the conclusion that acidic, aqueous conditions were present in the testing volume where sample 1 and sample 9 were located. Weak magnetite scattering from sample 8 indicated that the extent of acidic condensation (condensate) was likely less on sample 8 in comparison with sample 9. The XRD patterns of the untested and tested carbon-steel samples are shown in Figure 19.

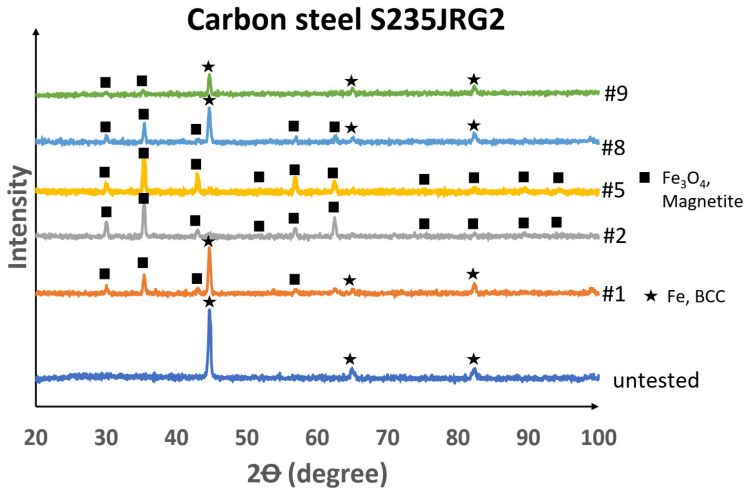

Figure 19. XRD scatters from carbon-steel samples from bottom to top: (untested) Unexposed sample, (1) tested sample at the inlet in the first reactor, (2) tested sample in the middle of the first reactor, (5) tested sample in the middle of the second reactor, (8) tested sample in the middle of the third reactor and (9) tested sample at the outlet of the third reactor.

From the microstructural, weight-loss and XRD analysis of the carbon steel, it was concluded that the testing fluid was likely in a two-phase state at the first few centimetres in the inlet of the first reactor and in a two-phase state or condensing condition in the third reactor. The results indicated that the testing fluid was in a superheated state in the testing volume between the two-phase volumes as illustrated in Figure 20.

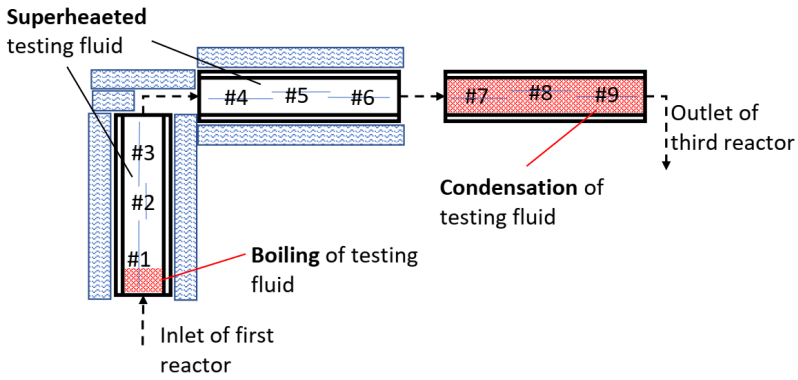

Figure 20. Boiling was thought to have occurred in the volume in the first few centimetres in the first reactor and condensation of testing fluid was thought to have occurred in the third reactor.

The XRD results of the surface of the titanium alloy samples showed little difference in crystal structure for the tested sample in comparison with the untested sample. Some changes were observed for sample 1 (a zirconium oxide crystal structure), which was not detected in other samples. Alumina oxide–BCC phase was detected on samples 2 and 5, which was likely due to corroded alumina oxide washers' being transported to the samples. The XRD result for the tested titanium alloy samples was in good agreement with the results from the SEM and XEDS analysis, i.e., an insignificant corrosion effect as illustrated in Figure 21.

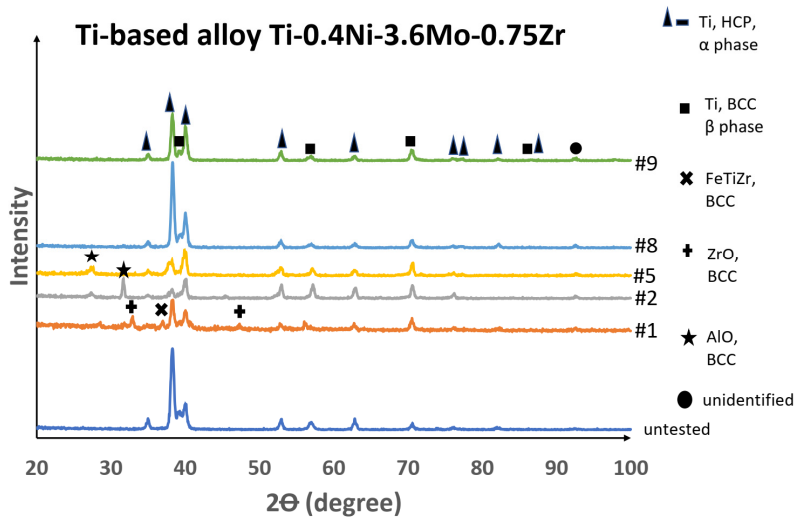

Figure 21. XRD scatters from the titanium alloy from bottom to top: (untested) Unexposed sample, (1) tested sample at the inlet in the first reactor, (2) tested sample in the middle of the first reactor, (5) tested sample in the middle of the second reactor, (8) tested sample in the middle of the third reactor and (9) tested sample at the outlet of the third reactor.

4. Conclusions

Carbon steel and titanium-alloy were tested in a simulated, high-temperature geothermal environment. From the corrosion testing of the carbon steel, it was concluded that the testing fluid was at boiling conditions (two-phase) at the first few centimetres of reactor

1 where sample 1 was situated, at superheated (single-phase) conditions in the testing volume accommodating samples 2–6 and at condensation (two-phase) conditions at samples 7–9. The low carbon steel, S235JRG2, was prone to general and localized corrosion damage in the testing volume where boiling and condensation occurred, i.e., the two-phase state of the testing fluid. Mixed corrosion products (oxides, sulphides and chlorides) were observed in the sample at boiling locations. The oxide corrosion layer was dominant on the samples in the superheated testing volume, and sulphides with an oxide sublayer were observed on the samples in the testing volume where condensation occurred. A dissimilar corrosion behaviour of carbon steel in the testing volume where boiling and condensation occurred could have been attributed to the effect of sodium chloride brine deposits that formed in the boiling process, or to different mass-removal transport phenomena due to availability of aqueous testing fluid and the barrier effect of the sodium chloride brine. The lack of sulphide layer formation on the oxide layer on the surface of the sample in the superheated testing volume could have been due to the slow kinetics of sulphide formation. The titanium alloy, Ti-0.4Ni-3.6Mo-0.75Zr (Ti-475) was not prone to corrosion where the testing fluid was in a single superheated or two-phase testing volume. This alloy could therefore be a promising candidate as a geothermal casing material in a high-temperature, corrosive, geothermal environment where single- or double-phase conditions with high brine and acidic concentrated conditions are expected.

Author Contributions: Conceptualization, A.I.T. and S.N.K.; methodology, A.I.T. and S.N.K.; software, A.I.T.; formal analysis, A.I.T.; investigation, A.I.T.; resources, A.I.T.; data curation, A.I.T.; writing-original draft preparation, A.I.T.; writing—review and editing, A.I.T. and S.N.K.; visualization A.I.T. and S.N.K.; supervision, S.N.K.; project administration, S.N.K.; funding acquisition, S.N.K.; All authors have read and agreed to the published version of the manuscript.

Funding: The authors would like to thank the Icelandic Research Fund (RANNÍS) grants No. 163108-051, 163108-052 and 163108-053, Geothermal Research Group (GEORG) and Energy Research Fund (Landsvirkjun) for funding this project.

Data Availability Statement: The raw/processed data required to reproduce these findings cannot be shared at this time as the data also forms part of an ongoing study.

Acknowledgments: The authors would like to give gratitude to employees at Innovation Center of Iceland (ICI) and employees at Grein Research for their technical assistance. The authors would also like to give gratitude to Titanium Metals Corporation (TIMET) for collaboration and providing titanium samples for the testing.

Conflicts of Interest: The authors declare no conflict of interest.

References

1. Thomas, R. Titanium in the geothermal industry. *Geothermics* **2003**, *32*, 679–687. [CrossRef]
2. Syrett, B.C.; Macdonald, D.D.; Shih, H. Pitting resistance of engineering materials in geothermal brines—I. Low salinity brine. *Corrosion* **1980**, *36*, 130–139. [CrossRef]
3. MacDonald, W.D.; Grauman, J.S. Exposure testing of UNS R53400, R56404 and N06625 in simulated salton sea geothermal brine. In Proceedings of the NACE-2018-11547, Phoenix, AZ, USA, 15–19 April 2018; p. 9.
4. Faes, W.; Lecompte, S.; Ahmed, Z.Y.; Van Bael, J.; Salenbien, R.; Verbeken, K.; De Paepe, M. Corrosion and corrosion prevention in heat exchangers. *Corros. Rev.* **2019**, *37*, 131–155. [CrossRef]
5. Carter, J.P.; McCawley, F.X. Corrosion tests in brine and steam from the Salton Sea KGRA. *J. Mater. Energy Syst.* **1982**, *3*, 30–38. [CrossRef]
6. Grauman, J.S. Titanium—Properties and applications for the chemical process industries. *Encycl. Chem. Process. Des.* **1998**, *58*, 123–147.
7. Schutz, R.W.; Wardlaw, T.L.; Hall, J.A. Ti-CODE 12—An improved industrial alloy. In Proceedings of the Anniversary Conference of the Japan Titanium Society, Kobe, Japan, 15–18 November 1982.
8. Abdel-Hady, M.; Fuwa, H.; Hinoshita, K.; Kimura, H.; Shinzato, Y.; Morinaga, M. Phase stability change with Zr content in β-Type Ti-Nb alloys. *Scr. Mater.* **2007**, *57*, 1000–1003. [CrossRef]
9. Zhou, Y.; Li, Y.; Yang, X.; Cui, Z.; Zhu, S. Influence of Zr content on phase transformation, microstructure and mechanical properties of Ti75-XNb25Zrx (x = 0–6) Alloys. *J. Alloy. Compd.* **2009**, *486*, 628–632. [CrossRef]

10. Oliveira, N.T.C.; Ferreira, E.A.; Duarte, L.T.; Biaggio, S.R.; Rocha-Filho, R.C.; Bocchi, N. Corrosion resistance of anodic oxides on the Ti-50Zr and Ti-13Nb-13Zr alloys. *Electrochim. Acta* **2006**, *51*, 2068–2075. [CrossRef]
11. Zhang, Y.; Davenport, A.J.; Burke, B.; Vyas, N.; Addison, O. Effect of Zr addition on the corrosion of Ti in acidic and Reactive Oxygen Species (ROS)-Containing environments. *ACS Biomater. Sci. Eng.* **2018**, *4*, 1103–1111. [CrossRef]
12. Nogara, J.; Zarrouk, S.J. Corrosion in geothermal environment: Part 1: Fluids and their impact. *Renew. Sustain. Energy Rev.* **2018**, *82*, 1333–1346. [CrossRef]
13. Nogara, J.; Zarrouk, S.J. Corrosion in geothermal environment: Part 2: Metals and alloys. *Renew. Sustain. Energy Rev.* **2018**, *82*, 1347–1363. [CrossRef]
14. Karlsdottir, S.N. Corrosion, Scaling and Material Selection in Geothermal Energy Production. In *Comprehensive Renewable Energy*; Elsevier: Amsterdam, The Netherlands, 2012; pp. 239–256, ISBN 978-0-08-087872-0.
15. Thorhallsson, A.I.; Stefansson, A.; Kovalov, D.; Karlsdottir, S.N. Corrosion testing of materials in simulated superheated geothermal environment. *Corros. Sci.* **2020**, *168*, 108584. [CrossRef]
16. Ikeuchi, J.; Sanada, N.; Asano, O.; Kurata, Y.; Sata, N.; Nanjo, N.; Ikeshoji, T.; Okahara, Y. Corrosion behavior of materials in various geothermal environments. *J. Electrochem. Soc.* **1987**, *134*, C423.
17. Culivicchi, G.; Palmerini, C.G.; Scolari, V. Behaviour of materials in geothermal environments. *Geothermics* **1985**, *14*, 73–90. [CrossRef]
18. Karlsdottir, S.N.; Ragnarsdottir, K.R.; Thorbjornsson, I.O.; Einarsson, A. Corrosion testing in superheated geothermal steam in Iceland. *Geothermics* **2015**, *53*, 281–290. [CrossRef]
19. Kritzer, P. Corrosion in high-temperature and supercritical water and aqueous solutions: A review. *J. Supercrit. Fluids* **2004**, *29*, 1–29. [CrossRef]
20. Sarrade, S.; Feron, D.; Rouillard, F.; Perrin, S.; Robin, R.; Ruiz, J.-C.; Turc, H.-A. Overview on corrosion in supercritical fluids. *J. Supercrit. Fluids* **2017**, *120*, 335–344. [CrossRef]
21. Liu, Z.; Gao, X.; Du, L.; Li, J.; Zheng, C.; Wang, X. Corrosion Mechanism of Low-Alloy Steel Used for Flexible Pipe in Vapor-Saturated H_2S/CO_2 and H_2S/CO_2-Saturated Brine Conditions. *Mater. Corros. Werkst. Korros.* **2018**, *69*, 1180–1195. [CrossRef]
22. Yang, J.; Wang, S.; Li, Y.; Tang, X.; Wang, Y.; Xu, D.; Guo, Y. Effect of salt deposit on corrosion behavior of Ni-based alloys and stainless steels in supercritical water. *J. Supercrit. Fluids* **2019**, *152*, 104570. [CrossRef]
23. Jonsson, T. Corrosion Testing in a Simulated High Temperature Geothermal Environment. Master's Thesis, University of Iceland, Reykjavik, Iceland, 2015.
24. Thorhallsson, A.I.; Karlsdottir, S.N.; Stefansson, A. Corrosion testing of uns n06625 in a simulated high temperature geothermal environment. In Proceedings of the NACE Corrosion Conference & Expo 2018, Phoenix, AZ, USA, 15 April 2018.
25. Arnórsson, S. *Isotopic and Chemical Techniques in Geothermal Exploration, Development and Use: Sampling Methods, Data Handling, Interpretation*; Non-Serial Publications; International Atomic Energy Agency: Vienna, Austria, 2001; ISBN 92-0-101600-X.
26. Felder, R.M.; Rousseau, R.W.; Bullard, L.G. *Felder´s Elementary Principles of Chemical Processes*; Wiley and Sons: Hoboken, NJ, USA, 2016.
27. Wolfram. *Wolfram Alpha Widgets*; Wolfram Alpha LLC: Champaign, IL, USA, 2020.
28. American Petroleoum Institute. *API 5CRA—Specification for Corrosion Resistant Alloy Seamless Tubes for Use as Casing, Tubing and Coupling Stock*; American Petroleoum Institute: Washington, DC, USA, 2015.
29. ASTM. *ASTM G1-90 Standard Practice for Preparing, Cleaning, and Evaluating Corrosion Test Specimens*; ASTM: West Conshohocken, PA, USA, 1999.
30. Gao, S.; Jin, P.; Brown, B.; Young, D.; Nesic, S.; Singer, M. Corrosion behavior of mild steel in sour environments at elevated temperatures. *Corrosion* **2017**, *73*, 915–926. [CrossRef]
31. Gao, S.; Brown, B.; Young, D.; Singer, M. Formation of iron oxide and iron sulfide at high temperature and their effects on corrosion. *Corros. Sci.* **2018**, *135*, 167–176. [CrossRef]
32. Gao, S.; Jin, P.; Brown, B.; Young, D.; Nešić, S.; Singer, M. Effect of high temperature on the aqueous H_2S corrosion of mild steel. *Corrosion* **2017**, *73*, 1188–1191. [CrossRef]
33. Choi, Y.-S.; Nesic, S.; Ling, S. Effect of H_2S on the CO_2 corrosion of carbon steel in acidic solutions. *Electrochim. Acta* **2011**, *56*, 1752–1760. [CrossRef]
34. Mursalov, N.I. Characteristic and mechanism of hydrogen sulfide corrosion of steel. *Process. Petrochem. Oil Refin.* **2017**, *18*, 215–228.
35. Kumagai, H.; Matsumoto, M.; Toyoda, K.; Obara, M.; Suzuki, M. Fabrication of titanium oxide thin films by controlled growth with sequential surface chemical reactions. *Thin Solid Film.* **1995**, *263*, 47–53. [CrossRef]
36. MacDonald, W. The service history and performance of titanium in geothermal systems. In Proceedings of the NACE Corrosion Conference & Expo 2014, San Antonio, TX, USA, 9 March 2014.
37. Schutz, R.W.; Watkins, H.B. Recent developments in titanium alloy application in the energy industry. *Mater. Sci. Eng. A* **1998**, *243*, 305–315. [CrossRef]
38. Beverskog, B.; Puigdomenech, I. Revised pourbaix diagrams for iron at 25–300 Degrees C. *Corros. Sci.* **1996**, *38*, 2121–2135. [CrossRef]

5.5 Journal Article 4

A.I. Thorhallsson, A. Stefansson, S.N. Karlsdottir, Silica scaling and boiling effect on corrosion behaviour of nickel-based alloys associated with superheated hydrothermal fluids containing HCl, H_2S and CO_2, Geothermics 101 (2022) 102384. https://doi.org/10.1016/j.geothermics.2022.102384

Geothermics 101 (2022) 102384

Contents lists available at ScienceDirect

Geothermics

journal homepage: www.elsevier.com/locate/geothermics

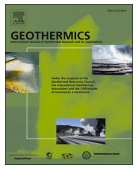

Silica scaling and boiling effect on corrosion behaviour of nickel-based alloys associated with superheated hydrothermal fluids containing HCl, H_2S and CO_2

Andri Isak Thorhallsson [a,*], Andri Stefansson [b], Sigrun Nanna Karlsdottir [a]

[a] Faculty of Mechanical Eng., Industrial Eng. and Computer Science, University of Iceland, Hjardarhagi 2-6, Reykjavik 107, Iceland
[b] Institute of Earth Sciences, University of Iceland, Sturlugata 7, Reykjavik 101, Iceland

ARTICLE INFO

Keywords:
UNS N06845
UNS N06255
SiO2 scale
high-temperature
geothermal
corrosion

ABSTRACT

The effect of amorphous silica (AM-silica) surface deposits on the corrosion behaviour of two nickel-based alloys associated with superheated hydrothermal fluid containing sour gases (HCl, H_2S and CO_2) was investigated experimentally at 350 °C at 10 barG. The results demonstrate that the AM-silica scales do not promote localized corrosion damage whereas some corrosion products were detected in non-scale samples due to fluid boiling from sub- to superheated conditions. This study contributes to more understanding of the effect of amorphous silica scaling and boiling on corrosion behaviour and the selection of materials for future application in superheated geothermal systems.

1. Introduction

Silica precipitation and scaling is commonly observed and associated with hydrothermal fluid utilization in geothermal power production. High-temperature hydrothermal fluids (>200 °C) are characterized by elevated dissolved silica concentrations, commonly between ~400 and 1000 ppm SiO_2 (e.g., Hauksson et al., 2014 Meier et al., 2014;). The concentration of aqueous silica is controlled by equilibrium with silicon dioxide minerals (SiO_2) like quartz, chalcedony or amorphous silica (AM-silica), and their solubility decreases with decreasing temperature (Hauksson et al., 2014, 2014 Meier et al., 2014;). Hydrothermal fluid utilization typically involves fluid discharged from deep boreholes sunk into the geothermal systems, followed by fluid flow at the surface through processing equipment where the temperatures and pressures are lowered to generate steam that is separated from the liquid brine. Subsequently, the steam is used for electrical power production whereas the brine is reinjected back into the geothermal system (Hammons, 2004 Michaelides, 2012;). Due to hydrothermal fluid temperature decrease and generation of steam during the process, the brine generally becomes supersaturated with respect to AM-silica resulting in a silica polymerization and scaling accumulation inside the geothermal equipment (Gunnarsson and Arnorsson, 2005). The scales can lower the power production efficiency (Gunnarsson and Arnorsson, 2005 Meier et al., 2014; Reyes et al., 2003;) and flow restrictions within the geothermal power system. In terms of corrosion, the silica scales may act as a corrosion barrier when deposited on the materials but may also result in induced localized corrosion damage (Mundhenk et al., 2013). Other under deposit corrosion phenomena have also been reported in that perspective e.g. corrosion of carbon steel in CO_2 concentrated solution under silica deposit (Barker et al., 2014 Huang et al., 2013;).

Massive silica scaling deposits have also been observed associated with superheated steam, for example, associated with material tests performed at the IDDP-1 geothermal well (Krafla in Iceland), upon the depressurization of the superheated steam from ~140 bar to <15 bars and temperatures of 450 °C to 350 °C (Karlsdottir et al., 2015). In-situ corrosion test at the IDDP-1 wellhead indicated localized, under deposit corrosion damage in materials that might have been promoted by massive silica scaling deposits (Karlsdottir et al., 2015). Further laboratory corrosion tests have been conducted for selected materials in a simulated superheated hydrothermal fluid containing H_2S, CO_2 and HCl without the presence of surface deposits like AM-silica (Thorhallsson et al., 2020a, 2020b). The results showed that only carbon steel was prone to localized corrosion damage where corrosion-resistant alloys such as nickel-based alloys were not corroded. As a result, it was concluded that silica scaling and/or other chemical components in the fluids like H_2 and/or HF were likely factors contributing to the localized

* Corresponding author.
E-mail address: ath196@hi.is (A.I. Thorhallsson).

https://doi.org/10.1016/j.geothermics.2022.102384
Received 5 October 2021; Received in revised form 8 December 2021; Accepted 20 February 2022
Available online 27 February 2022

corrosion damage observed for the in-situ corrosion tests of the nickel-based alloys observed at the IDDP-1 well (Karlsdottir et al., 2015).

To study the contribution of the AM-silica scaling on the localized corrosion behaviour of two nickel-based alloys (UNS N06255 and UNS N06845) in a superheated geothermal environment, laboratory experiments were conducted at 350 °C and 10 bar, using simulated superheated hydrothermal (H_2O) fluid containing H_2S, CO_2 and HCl. The test environment was selected to resemble the conditions in the in-situ corrosion test conducted at the IDDP-1 deep geothermal well in Krafla Iceland (Karlsdottir et al., 2015). The two nickel-based alloys were tested with AM-silica scaling prepared from geothermal brine scaling. Moreover, the corrosion behaviour of a recently developed nickel-based alloy UNS N06845, not coated with AM-silica scaling, was also tested in the simulated superheated steam at the same temperature and pressure conditions. These conditions can be expected in the geothermal energy production from high temperature deep geothermal wells. The corrosion behaviour of the various materials was investigated using Scanning Electron Microscope (SEM), X-ray Electron Dispersive Spectroscopy (XEDS) and X-ray diffraction (XRD).

2. Methods

2.1. Experimental setup

The corrosion tests were performed using a custom made flow-through apparatus consisting of three reactors connected in series. A detailed description of the setup and function of the corrosion testing facility is described in (Thorhallsson et al., 2021, 2020a). The three reactors were insulated with ceramics and glass wool. Each reactor accommodated three flat coupon samples. The corrosion tests were conducted at 350 °C and 10 bar pressure for 10 days and a constant flow rate of ~0.3 ml/min. The duration of the tests was selected by the results obtained with other pretests (Jónsson, 2015) made in similar equipment at UoI and the flow rate of 0.3 ml/min was selected because it was the lowest flow rate obtained with pumps with high accuracy. The low flow rate of fluid was selected to make more time for heat transfer between heaters and fluid (i.e. guarantee superhot condition of fluid was obtained). The solutions were pumped through a degasser using two HPCL pumps (Series I, Chromtech, Apple Valley, USA), mixed in-line before injection into the reactors, flowed through the reactors, and were cooled and depressurized at the end of the line using a cooling jacket and a back-pressure regulator (BPR). The BPR was also used to regulate and maintain the pressure in the system. The temperature and pressure of the experimental solutions were monitored during the experiments using K-type thermocouples and pressure gauges (S-20 digital pressure transducer, WIKA, Klingenberg, Germany). A schematic of the experimental setup is shown in Fig. 1.

2.2. Materials

Two types of nickel-based alloys were tested in this study, UNS N06845 and UNS N06255. The nominal chemical composition of the two alloys can be seen in Table 1. The samples were tested with and without AM-silica surface depositions or scales. Each reactor accommodated three flat coupon samples. Two samples with 100 mm length; 7 mm width; and1 mm thick and one sample with 50 mm length; 7 mm width; and 1 mm thick were prepared. All the samples had 5 mm diameter holes for fasteners, centred 5 mm from both flat ends. Three samples of the nickel-based alloy UNS N06845 with no silica surface scales were tested in the first reactor where boiling and heating of the simulated hydrothermal fluid to superheated conditions occurred (see Fig. 1 for the figuration of the samples in the reactors during the tests). The other three UNS N06845 samples with silica surface scales were tested in the third reactor where the simulated hydrothermal fluid was superheated. Three samples of the other nickel-based alloy type, grade UNS N06255, with silica scale were tested in the second reactor. In each reactor, one sample was assigned for microstructural and chemical analysis in the cross-section of the sample but the other two samples were assigned for weight loss analysis for corrosion rate calculations. The first sample at the inlet of the first reactor was used for microstructural and chemical analysis of the UNS N06845 samples but the centre samples in the second and third reactor were used for microstructural and chemical analysis of the silica-coated UNS N06255 and UNS N06845 respectively. Other samples in all the reactors were used for weight loss analysis. The first sample in the first reactor was selected for microstructural and chemical analysis due to the two-phase presence in that particular section of the testing volume.

All the samples were ground to 600 grit with SiC abrasive paper before the silica scales were deposited on the surface. As mentioned previously, the samples accommodated in reactors two and three (see Fig. 1) were coated with a geothermal silica scale by the precipitation of AM-silica from 100 °C hot aqueous liquid brine, sourced from a silencer at Svartsengi geothermal site in Iceland. The chemical composition of the brine water, from five wells contributing to the fluid in the silencer, is given in Table 2. The CO_2 and H_2S were analysed with titration, the

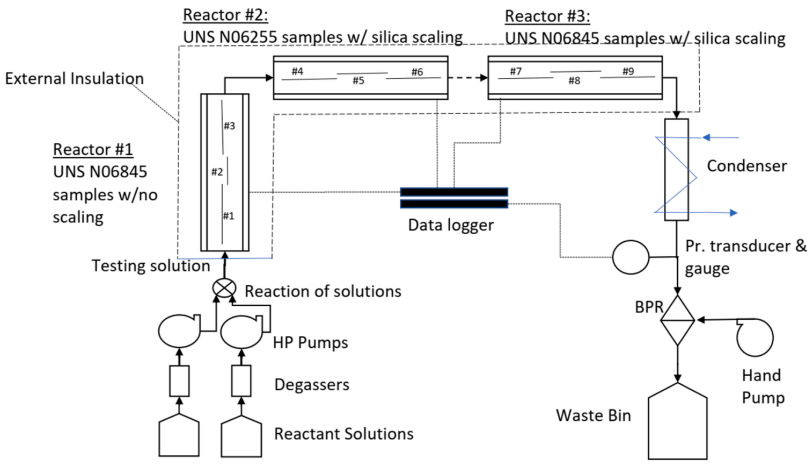

Fig. 1. A schematic diagram of the experimental apparatus used for the corrosion testing.

Table 1
Chemical composition of UNS N06255 and UNS N06845. All values are maximum values except iron (Fe).

	Composition ranges [% wt]								
	C	**Si**	**Mn**	**Cr**	**Ni**	**Mo**	**Cu**	**W**	**Fe**
N06255	≥0.03	≥1	≥1	23–26	47.0–52.0	6.0–9.0	≥1.2	≥3	bal.[a)]
N06845	≥0.05	≥0.5	≥0.5	20–25	44.0–50.0	5.0–7.0	2.0–4.0	2.0–5.0	bal. [a)]

[a)] Balanced value.

Table 2
Chemical analysis from the brine water in the five wells contributing to the fluid in silencer.

Parameter	Brine composition*	Unit
pH	7.4	
CO_2	6.36	mg/kg
H_2S	0.18	mg/kg
NH_3	0.73	mg/kg
B	7.99	mg/kg
SiO_2	486.6	mg/kg
Na	7196	mg/kg
K	1057	mg/kg
Mg	0.44	mg/kg
Ca	1074	mg/kg
F	0.2	mg/kg
Cl	13,906	mg/kg
Br	42.9	mg/kg
SO_4	27.1	mg/kg
Al	0.14	mg/kg
As	0.07	mg/kg
Ba	2.04	mg/kg
Cd	<0.00005	mg/kg
Co	0.0001	mg/kg
Cr	<0.0001	mg/kg
Cu	<0.0005	mg/kg
Fe	0.024	mg/kg
Hg	0.00001	mg/kg
Li	3.27	mg/kg
Mn	0.17	mg/kg
Mo	0.05	mg/kg
Ni	0.004	mg/kg
Pb	<0.0003	mg/kg
Sr	7.9	mg/kg
Zn	0.008	mg/kg
TDS**	24,798	mg/kg
H_2O	bal.	

*Average composition from wells SV-18, SV-19,SV-21, SV-25 and SV-26.
**Total Dissolved Solids.

anions analysed with ion chromatography (IC) and the cations with Inductively coupled plasma - optical emission spectrometry (ICP-OES). For the deposition of the silica scale, the samples were placed in a porous polypropylene container (non-conductive) and submerged in a brine pond at the outlet of the silencer. The AM-silica deposition time in the hydrothermal brine was one month. Following, the samples with the scales were dried, and the scale thickness was reduced down to 1 mm with a gauge before testing. Other samples of the UNS N06255 and UNS N06845 that were not intended for the corrosion testing were also coated with geothermal scaling for comparative analysis i.e. to see if any significant corrosion occurred in the samples after the scaling procedure. The chemical composition of the scaling material was analysed by X-ray Energy Dispersive Spectroscopy (XEDS).

2.3. Post-exposure measurements and analysis

The samples assigned for weight loss analysis were weighed and measured according to ASTM G1–03 (*ASTM G1-03(2017)e1 Standard Practice for Preparing, Cleaning, and Evaluating Corrosion Test Specimens*, 2017) before the scaling procedure and the corrosion testing. After the corrosion test, the weight loss samples were cleaned according to the same standard. The same cleaning agent was applied to remove the silica scaling from the samples in the second and third reactors. However, this approach was not always found effective and hence, a concentrated NaOH(aq) solution at 60 °C was also applied in an attempt to remove the silica scaling from the samples.

The measured corrosion rate (CR) of the material tested in mm/year was calculated via the weight loss method and according to the same standard:

$$CR = K \bullet W/A \bullet t \bullet \rho \quad (1)$$

where K is the corrosion rate constant equal to $8.76 \bullet 10^4$ mm/year, W is the mass loss in grams of the tested material with $a \pm 0.00005$ gram precision, A is the exposed surface area in cm^2 of the tested sample, t is the exposure time in hours, and ρ is the material density in g/cm^3.

For microstructural analysis, Scanning Electron Microscope (SEM) (Zeiss, Oberkochen, Germany) was applied. For the chemical analysis of the samples, corrosion products and scaling products, X-ray Electron Dispersive Spectroscopy (XEDS) (Abingdon, England) with Si(Li) X-ray detector and AZtec software (version 3.3) was applied. SEM and XEDS were also used to analyse untested samples for comparison. The samples were cut with a diamond blade and mounted in phenol-formaldehyde under elevated temperature and pressure. Mounted samples were then ground to 1000 grit with SiC abrasive paper and polished down in a few steps with 0.02 – 0.06 μm colloidal silica in the final polishing step. The solid-state structure of the materials was analysed in-situ by X-Ray Diffractometer (XRD) before and after corrosion tests with XPert Pro-XRD metre (Malvern Panalytical, Malvern, UK) from PANalytical with Data Collector software. The structural identification (amorphous and crystal) of the geothermal scaling material present on the samples in the second and third reactor was done in A Bruker AXS D8 Focus X-Ray Diffractometer (Bruker, Bilerica, USA) was used, with Ni-filtered Cu ka radiation at 1.54 Å wavelength at 40 mA and 40 kV with fixed 1° slit and NaI oscillation counter. Validation/calibration of the Bruker D8 Focus X-ray diffractometer was performed using NIST (SRM-1976) standard sample.

3. Results and discussion

3.1. XRD analysis

Powder X-ray diffraction was conducted on the finely ground scaling material after the scaling deposition of the samples. Only amorphous structures and crystalline NaCl were detected (Fig. 2). X-ray diffraction (XRD) analysis was also conducted on part of the samples that were used for microstructural and chemical analysis i.e. the first sample in the first reactor but centre samples in the second and third reactor. In short, the morphology of the surface was not significantly affected by the exposure to the corrosive test environment. The X-ray scatter from the tested samples were like the X-ray scatter from the untested samples, except for one distinction seen for the uncoated, first sample of UNS N06845 (in the first reactor, one cm away from the inlet) where one peak was detected at $2\Theta = 36°$ which was not seen for the untested sample. From the microstructural analysis of the same sample (Section 3.2.1), it can be seen that some crystal deposits were observed on the sample which was likely the reason for the peak at $2\Theta = 36°$ observed in the X-ray scatter from the tested sample. XRD peaks from the untested and tested UNS N06845 samples can be seen in Fig. 3a. The results of the XRD analysis of

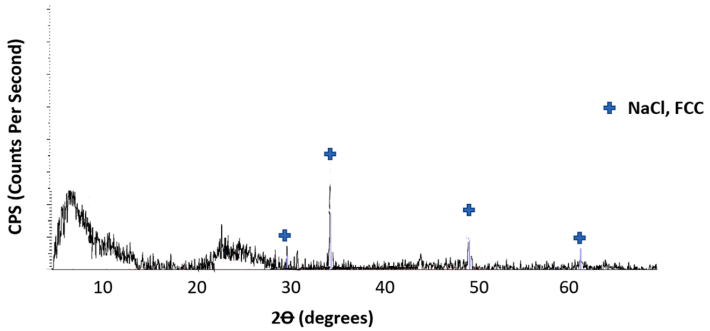

Fig. 2. Filtered XRD scatter from the finely ground geothermal scaling powder.

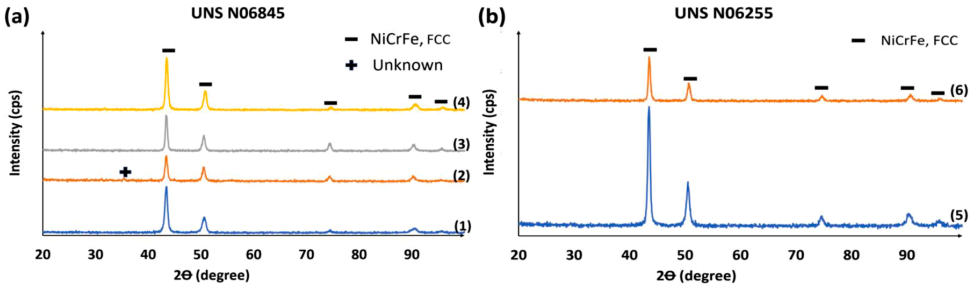

Fig. 3. (a) UNS N06845; (1) Untested UNS N06845, (2) tested UNS N06845 with no silica scaling one cm away from the inlet of the first reactor (sample #1), (3) tested UNS N06845 with no silica scaling five cm away from the inlet of the first reactor (sample #1) and (4) tested UNS N06845 with silica scaling in middle of the third reactor (sample #8). (b) UNS N06255; (5) untested UNS N06255 and (6) tested silica-coated UNS N06255 in the second reactor (sample #5).

tested silica-coated UNS N06255 in the second reactor showed also a negligible effect of the corrosive testing environment on the surface morphology of the alloy (Fig. 3b).

3.2. Microstructural and chemical analysis

3.2.1. UNS N06845 samples with no AM-silica scale

Three samples of UNS N06845 with no silica scale were tested in reactor 1. Sample #1 was analysed with microstructural and chemical compositional analysis at different locations on the sample; at the end of the sample 1 cm away from the inlet and in the middle of the sample which is approximately 5 cm and as well as 10 cm away from the reactor inlet. The location of the microstructural analysis in sample #1 in the reactor was chosen on the basis that it is located where boiling of the testing fluid occurs as described previously (Thorhallsson and Karlsdottir, 2021).

No evidence of general or localized corrosion damage was observed in the microstructural analysis of the cross-sections of sample #1. No corrosion film or corrosion pits or cracks were observed in the cross-section of the sample 1 cm away from the inlet but some iron-rich oxides and sulphide deposits were though detected at this location (Fig. 4 and Table 3). The deposits are likely mostly originated from corrosion products from the reactor pipe and fittings (materials UNS N10276 and UNS N06625 respectively) that was found to react and corrode in the first few cm of the internal surface of the reactor pipe (and fittings). The presence of copper-rich sulphides on the surface of sample #1 may though indicate possible corrosion of the UNS N06845 in the harsh boiling regime in the reactor which is an interesting topic for future studies. In the cross-section in the middle of sample #1, there was also no corrosion damage observed, i.e. general corrosion or localized corrosion damage. Some aluminium was though detected on the surface

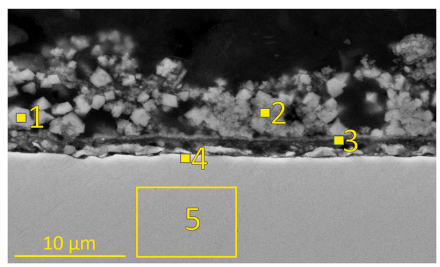

Fig. 4. Cross-section of sample #1, UNS N06845 without silica scaling, 1 cm away from the inlet of the first reactor.

in the middle of sample #1, which was concluded to be originated from the alumina washer used between the sample and fastener (Fig. 5 and Table 4). Similar results were obtained in the cross-section at the end (ca. 10 cm away from the inlet), i.e. negligible corrosion damage was observed. However, on the external surface of sample #1, some corrosion indicators were observed that were not detected in the cross-sectional analysis. At the inlet, discrete Cu-S rich corrosion products were observed on the surface indicating that the UNS N06845 sample likely corroded at the inlet and Cu-S rich corrosion products were transported to the surface (Fig. 6a and Table 5). In the middle of the sample, some surface deposits including S and O-rich were observed that likely formed in the boiling regime (Fig. 6b and Table 5). Further away from the inlet (ca. 10 cm away) no corrosion indicators were observed but some deposits were though detected (Fig. 6c and Table 5).

Other corrosion studies have reported corrosion damage of corrosion-resistant nickel-based alloys in testing volumes where the

Table 3
Chemical composition from selected locations in Fig. 4.

	Element (wt%)									
Location	**O**	**Na**	**S**	**Ca**	**Cr**	**Fe**	**Ni**	**Cu**	**Mo**	**W**
1	10.9		44.3		7.9	35.3	1.7			
2	8.7		45.8		8.0	36.4	1.2			
3	10.7	0.7	29.4	1.3	12.7	22.8	22.4			
4			1.3		23.3	16.3	44.1	3.1	6.7	5.1
5					23.8	16.2	45.5	3.2	6.3	5.0

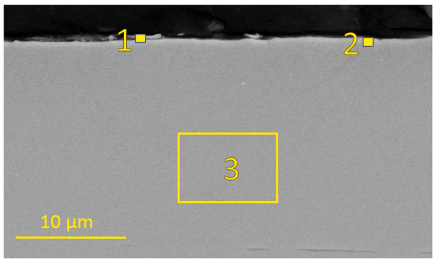

Fig. 5. Cross-section of sample #1, UNS N06845, in the middle of the sample in the first reactor (boiler).

phase transition of corrosive geothermal fluid occurred. Corrosion susceptibility was also reported for a UNS N06625 material used to scrub acidic gases from geothermal superheated steam with geothermal separator water at 10 barG and 180 °C. The N06625 scrubbing pipe material was reported to have localized corrosion damage (Karlsdóttir et al., 2013) but the fluid contacting the UNS N06625 material in the wet scrubbing chamber at 180 °C and 10 barG was considered to be in a two-phase state (i.e., gas and liquid). The result of the wet scrubbing testing indicated that UNS N06625 was prone to corrosion damage in a two-phase geothermal fluid at 180 °C and 10 barG. In our study, Cu and W alloying elements in the two nickel-based alloys tested are the most significant difference from the alloy composition of UNS N06625. The W element has been reported to enhance the pitting resistance of the alloys and the increased Cu content in UNS N06845 has been reported to enhance the general corrosion resistance of the alloy in sour environments (Sagara et al., 2018). In addition, the nickel-based alloy N06845 has shown good corrosion and pitting resistance in strong NH_4Cl solutions (Toba et al., 2012) but no corrosion studies have been reported for the UNS N06845 in a mixed-phase state or boiling state of the geothermal fluid at high temperatures. Corrosion tests of the alloy have only been conducted and reported in a simulated superheated geothermal environment by (Thorhallsson et al., 2020a, 2020b) where no indication of corrosion damage was observed. Due to the boiling of the fluid at the inlet of the first reactor, it can be concluded that the salinity of the residual liquid is very high which will induce the susceptibility for corrosion in the volume where boiling occurred in the test. Due to high pitting and transpassive potentials and high pitting resistance equivalent (PRE) number, good localized corrosion resistance of nickel-based alloys tested in a high salinity geothermal fluid in the North German Basin has been reported (Klapper et al., 2012). In this study, an indication of localized corrosion damage and Cu-S rich corrosion products were observed to some extent at the external surface in the tested sample in the boiling regime at the inlet. These findings suggest that Cu in the nickel-based alloy is reacting with H_2S in the test fluid. Previous studies of Cu-rich high-entropy alloys in the same testing facility in a superheated test fluid have reported poor corrosion resistance where the main corrosion products observed were also Cu-S rich corrosion products (Thorhallsson et al., 2021). This might indicate that Cu added alloys or Cu rich phases in materials are in general, more susceptible to corrosion in a corrosive environment containing H_2S, than similar, non-Cu containing corrosion-resistant alloys.

3.2.2. Silica coated UNS N06255 samples

Amorphous silica-coated UNS N06255 samples were tested in the second reactor where the testing fluid had been concluded to be superheated i.e. where the temperature is higher than saturation

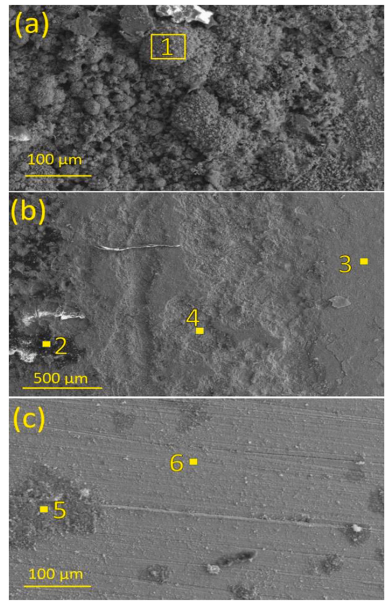

Fig. 6. The surface appearance of sample #1, UNS N06845 without silica scaling, (a) one cm from the inlet, (b) five cm from the inlet, and (c) ten cm from the inlet in the first reactor.

Table 4
Chemical composition from locations in Fig. 5.

	Element (wt%)									
Location	**Al**	**Si**	**Ca**	**Cr**	**Fe**	**Ni**	**Cu**	**Sr**	**Mo**	**W**
1		1.5		22.6	16.0	47.8	3.7	2.8	5.6	
2	0.4	0.8	0.4	23.2	15.7	45.1	3.2		6.2	5.1
3				23.2	16.3	46.9	3.4		5.4	4.9

Table 5
Chemical composition from locations in Fig. 6.

	Element (wt%)											
Location	**O**	**Na**	**Si**	**S**	**Cl**	**Cr**	**Mn**	**Fe**	**Ni**	**Cu**	**Mo**	**W**
1	5.4			25.8		0.8		5.0	50.4	12.6		
2	22.7	1.2	0.7	17.0	0.9	13.4	0.5	11.3	26.7	1.2	3.3	1.1
3	55.3	7.8		13.2		5.4		13.2	5.1			
4	22.0		0.8	0.8	0.2	11.2	1.6	41.7	12.2	0.8	5.5	3.2
5	25.6	2.2		4.5	2.1	4.6	1.4	43.7	7.4	0.5	5.6	2.3
6	16.7	0.5		2.1		16.6	0.8	23.6	29.8	1.6	4.8	3.7

temperature for pure H_2O at 10 barG with T_{sat} = 184.1 °C (Richard M. Felder and Ronald W. Rousseau, 2000). The centre sample #5 in the second reactor, was cross-sectioned at two locations for microstructural and chemical analysis. Visual inspection of the samples revealed that they were only partially coated with silica scale and the scaling had various forms (Fig. 7). As deionized water and superheated steam were used to flush the testing volume before and after the corrosion testing, some of the silica coating on the samples were potentially removed. It is well known that surface roughness can affect the adhesion of materials to the surface, for instance, the adhesion of silica film on glass substrate was reported by Abchi et al. (Abchi et al., 2021). In our study, the low adhesion of silica scale to the finely polished samples, with low surface roughness, was a likely reason for the loose scaling behaviour. Some of the AM-silica scalings may also have been removed during the cross-sectional cutting of the sample. The remaining AM-silica scaling coated sites on the surface were analysed and no localized corrosion damages were observed under the scales.

Unexpectedly, some Cr was observed in the scaling in the cross-sectional site (Fig. 7b and Table 6) but Cr was not detected in the hydrothermal brine fluid during the scaling process. Furthermore, voids likely due to entrapped gas or volatile species were also observed within the silica scales as seen in Fig. 7c. This observation might indicate that some corrosion products might have been carried over to the sample from the first reactor pipe or fittings during the flushing process (or during the corrosion testing) with some dissolved or loose silica travelling in the flushing deionized water during the flushing process. During the cooling of the testing volume or the flushing period at end of the testing period, some re-precipitation of the silica may also have occurred on the sample. In another study with UNS N06255 tested in-situ in a superheated geothermal fluid with H_2S, CO_2, HF, H_2, and long exposure period resulting in the samples being covered with AM-silica scale during the test, very low corrosion rate was measured but some localized corrosion damage or pit was observed in nickel-based alloys (Karlsdottir et al., 2015). In a recently published study, no localized corrosion damage was detected in a UNS N06255 material tested in simulated superheated geothermal fluid without silica scale and HF, H_2 gasses (Thorhallsson et al., 2020a, 2020b). In this study, neither HF nor H_2 was included in the test fluid and the testing period was only 10 days i.e. short in comparison with the in-situ test. This might indicate that HF, H_2 or longer exposure periods could contribute to localized corrosion damage of the nickel-based alloys in the geothermal environment.

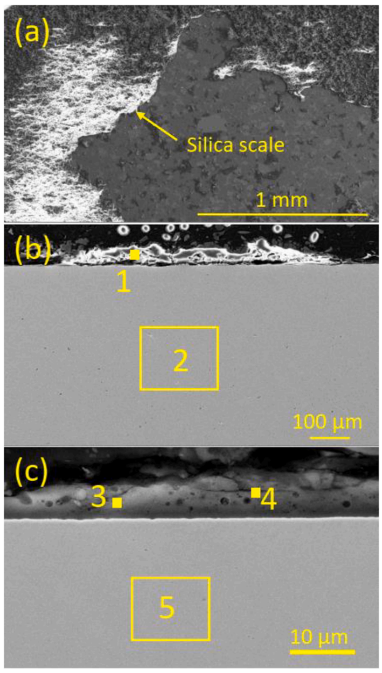

Fig. 7. a) Silica coverage of the surface of UNS N06255 samples in the second reactor, (a) part of the external surface on sample #4; and (b)-(c) cross-sections of sample #5.

3.2.3. *Silica coated UNS N06845 samples*

Most of the silica scale was also detached from the UNS N06845 samples in the third reactor during the test or flushing periods as seen in Fig. 8. The amount of remaining silica scaling adhering on the UNS N06845 samples after the corrosion testing was observed to a lesser extent than on the UNS N06255 samples in the second reactor. This might indicate that the adhesion of silica on the UNS N06845 samples is lower than on the UNS N06255 samples. The different adhesion abilities could be due to different surface properties in the two alloys or due to different roughness profiles.

No general corrosion or localized damage was observed in the cross-section of silica covered UNS N06845 after the corrosion testing in the simulated superheated geothermal fluid which is in an agreement with the results of the same uncoated (with AM-silica) alloy tested in the superheated conditions in the same test environment by Thorhallsson et al. (Thorhallsson et al., 2021, 2020a). As before, this indicates that the AM-silica scaling doesn't have a significant contribution to localized corrosion damage in the material.

Few studies with UNS N06845 or similar nickel-based alloys in superheated geothermal fluid have been published yet but some studies, for other nickel-based alloys, in oil or H_2S, CO_2 or HCl environment have though been published where the corrosion of the nickel-based alloy has been addressed in some specific environments; corrosion testing of UNS N07718 in simulated oil drilling environments was concluded to be susceptible for pitting corrosion at 150 °C and saline geothermal environment (Klapper and Stevens, 2014). High-stress corrosion cracking susceptibility of UNS N06625 in pure supercritical water has been reported between 400 and 550 °C likely due to internal oxidation along the grain boundaries (Teysseyre and Was, 2006).

As a general assumption for our study for both alloys, the AM-silica scales formed in this test was likely to have different properties (adhesion, porosity etc.) than the AM-silica scales experienced in the in-situ testing in the superheated hydrothermal fluid reported by Karlsdóttir

Table 6
Chemical composition from locations in Fig. 7.

	Element (wt%)								
Location	**O**	**Na**	**Si**	**Cl**	**Ca**	**Cr**	**Fe**	**Ni**	**Mo**
1	53.9		46.1						
2			0.4			25.3	19.4	48.8	6.1
3	47.7	0.6	48.2	0.5	0.5	0.7	0.5	1.3	
4	52.1	0.4	45.0	0.5	0.3	0.5	0.5	0.8	
5						25.2	19.7	48.7	6.4

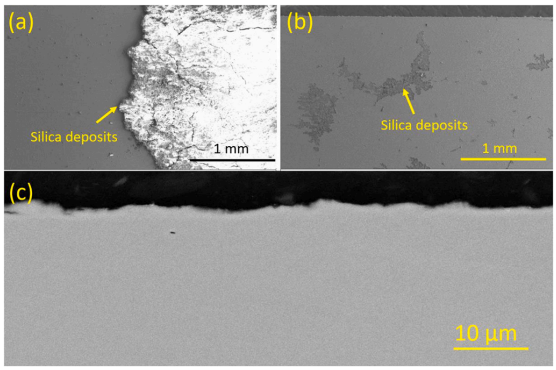

Fig. 8. a) Silica scaling remained on only part of the surface of UNS N06845; part of external surface of (a) sample #7 and (b) sample #8 and (c) cross-section in sample #8.

et al. (2015). The reason for this difference in the AM-silica scale structure might be due to that in the in-situ testing, the AM-silica was precipitated when superheated hydrothermal steam was throttled from 120 barG and 450 °C down to 12–13 barG and 360 °C; i.e. silica precipitated from the state change of high-density superheated fluid to lower temperature, low-density superheated fluid. In our testing, however, the AM-silica precipitated from liquid separator water at 100 °C, resulting in different precipitation behaviour. Silica scaling from aqueous hydrothermal fluid was studied by Heuvel et al. (van den Heuvel et al., 2018) where it was shown that the amorphous silica scaling density and porosity depends on several factors, including fluid flow and other chemical and physicochemical factors. Silica scaling in geothermal systems are well known to have various protective and adhering properties (Gunnarsson and Arnorsson, 2005 Mroczek et al., 2017; Reyes et al., 2003; Rodgers et al., 2004;). As a result, the difference in the properties of the silica scale in our tests such as porosity, density etc., compared to the silica scaling experienced in the in-situ tests is acknowledged here. The potential different scaling properties might hence affect the access or diffusion of a corrosive species to the material or have some other synergistic effect with the test fluid and might therefore affect the corrosion behaviour in the test environment. This is an area for further studies but not within the scope of this study.

3.3. Weight loss analysis

Weight loss analysis was conducted on UNS N06845 samples #2 and #3 that were not scaled with silica and tested in the first reactor. The weight loss measured was insignificant after the testing and corrosion rate was hence low or 0.0005 mm/year and 0.0008 mm/year for samples #2 and #3 respectively. The UNS N06255 samples #4 and #6 with silica scaling from the second reactor and UNS N06845 samples #7 and #9 with silica scaling from the third reactor were cleaned in the suggested cleaning cycle from the standard ASTM G1–03 i.e. with an acidic cleaning agent to estimate the weight loss due to the corrosion testing. The cleaning cycle was used to remove the corrosion products from the samples but also to remove the scaling material from the samples. It was though found after a dozen of cleaning cycles with ASTM G1–03 etchant, that it was an inefficient medium to remove the scaling from the samples which had silica scaling. In a further attempt to remove the silica scaling from the samples and to estimate the weight loss of the samples and hence the corrosion rate, the samples with silica scaling were also brushed with bristles which though resulted only in insignificant silica removal. As no efficient cleaning agent for nickel-based alloys from ASTM standard G1–03 could remove the scaling material from the samples completely, the corrosion rate estimation with the weight loss method was not the focus of this study. Due to this lack of silica scaling removal with the acidic cleaning agent from ASTM G1–03, it was decided with yet another attempt to remove the silica scaling material with another cleaning agent; hot caustic soda i.e. saturated NaOH solution at 60 °C. This additional cleaning procedure was in short not successful and negligible silica scaling material was removed additionally after a few cleaning cycles. From the overall cleaning procedure, significant weight gain was always measured in all the samples tested with silica scaling. Mechanical cleaning with harder bristles or other surface cleaning material would involve to some extent, scratching of the surface of the nickel-based alloys and hence, biasing the weight loss results. More aggressive mechanical cleaning was therefore not executed. Consequently, the corrosion rate for the samples with the silica scaling in the 2nd and 3rd reactors could not be determined.

4. Conclusions

Based on the results in this study it is concluded that amorphous silica scaling does not induce localized corrosion damage on the nickel-based alloys UNS N06255 and UNS N06845 when tested in the simulated superheated geothermal fluid at 350 °C and 10 barG. No localized (or general) corrosion was observed in the AM-silica coated samples in this study. The geothermal scaling that was prepared for the corrosion testing is though likely to have some different properties than silica scale precipitated from a high density, superheated geothermal fluid. The recently developed nickel-based alloy, UNS N06845, was also tested without AM-silica scaling at a boiling and superheated state of the simulated geothermal fluid. The alloy was tested in highly corrosive conditions where phase transition from liquid to vapour occurred and was concluded to be prone to some corrosion, concluded from the Cu-S rich compounds observed on the surface. No significant localized corrosion damage was observed in the cross-sections analysed but some surface deposits were observed on the external surface of the sample. These results show that corrosion of the nickel-based alloys did not occur in the superheated geothermal fluid but further studies are needed regarding corrosion of the nickel-based alloys in a boiling, high-temperature geothermal fluid containing H_2S, CO_2 and HCl.

Data availability

The raw/processed data required to reproduce these findings cannot be shared at this time as the data also forms part of an ongoing study.

CRediT authorship contribution statement

Andri Isak Thorhallsson: Conceptualization, Data curation, Formal analysis, Investigation, Methodology, Writing – original draft. **Andri Stefansson:** Conceptualization, Methodology, Writing – review & editing. **Sigrun Nanna Karlsdottir:** Conceptualization, Funding acquisition, Methodology, Supervision, Writing – review & editing.

Declaration of Competing Interest

The authors declare that they have no known competing financial interests or personal relationships that could have appeared to influence the work reported in this paper.

Acknowledgements

The authors would like to thank the Icelandic Research Fund (RANNÍS), Geothermal Research Group (GEORG) and Energy Research Fund (Landsvirkjun) for funding this project. Employees at Innovation center of Iceland (ICI), employees at Grein Research and Icelandic Geosurvey (ISOR) for their technical assistance. The authors would also like to give gratitude to Nippon Steel for collaboration and for providing samples for testing.

References

Abchi, A., Belkhir, N., Alonso, J., 2021. Effect of storage and surface roughness on the SiO2 thin films adhesion behavior. J. Adhes. Sci. Technol. https://doi.org/10.1080/01694243.2021.1916259.

ASTM G1-03, 2017. e1 Standard Practice For Preparing, Cleaning, and Evaluating Corrosion Test Specimens, 2017. ASTM International.

Barker, R., Pickles, B., Neville, A., 2014. General corrosion of X65 mild steel under silica sand deposits in CO2-saturated environments in the presence of corrosion inhibitor compounds. In: Proceedings of the NACE Corrosion Conference & Expo 2014. Presented at the NACE Corrosion Conference & Expo 2014, San Antonio, Texas, USA.

Gunnarsson, I., Arnorsson, S., 2005. Impact of silica scaling on the efficiency of heat extraction from high-temperature geothermal fluids. Geothermics. https://doi.org/10.1016/j.geothermics.2005.02.002.

HAMMONS, T.J., 2004. Geothermal power generation worldwide: global perspective, technology, field experience, and research and development. Electr. Power Compon. Syst. 32, 529–553. https://doi.org/10.1080/15325000490224076.

Hauksson, T., Markusson, S., Einarsson, K., Karlsdottir, S.N., Einarssond, A., Moller, A., Sigmarsson, P., 2014. Pilot testing of handling the fluids from the IDDP-1 exploratory geothermal well, Krafla, NE Iceland. Geothermics. https://doi.org/10.1016/j.geothermics.2013.07.003.

Huang, J., Brown, B., Nesic, S., 2013. Localized corrosion of mild steel under silica deposits in inhibited aqueous CO2 solutions. In: Proceedings of the NACE Corrosion Conference & Expo 2013. Presented at the NACE Corrosion Conference & Expo 2013. NACE International, Orlando, FL, USA.

Jónsson, T., 2015. Corrosion Testing in a Simulated High Temperature Geothermal Environment (M.Sc. Thesis). University of Iceland, Reykjavik, Iceland.

Karlsdottir, S.N., Ragnarsdottir, K.R., Thorbjornsson, I.O., Einarsson, A., 2015. Corrosion testing in superheated geothermal steam in Iceland. Geothermics 53, 281–290. https://doi.org/10.1016/j.geothermics.2014.06.007.

Karlsdottir, S.N., Thorbjornsson, I., Sigmarsson, T., 2013. Corrosion and scaling in wet scrubbing equipment of the superheated geothermal well IDDP-1 in Iceland. In: Proceedings of the NACE Corrosion Conference & Expo 2013. Presented at the NACE Corrosion Conference & Expo 2013. NACE International.

Klapper, H.S., Baessler, R., Weidauer, K., Stuerzbecher, D., 2012. Evaluation of suitability of high-alloyed materials for geothermal applications in the North German basin. Corrosion 68. https://doi.org/10.5006/1.3676631, 016001-1-016001–9.

Klapper, H.S., Stevens, J., 2014. Susceptibility to pitting corrosion of nickel-based alloy 718 exposed to simulated drilling environments. Corrosion 70, 899–906. https://doi.org/10.5006/1154.

Meier, D.B., Gunnlaugsson, E., Gunnarsson, I., Jamtveit, B., Peacock, C.L., Benning, L.G., 2014. Microstructural and chemical variation in silica-rich precipitates at the Hellisheidi geothermal power plant. Mineral. Mag. https://doi.org/10.1180/minmag.2014.078.6.04.

Michaelides, E.E., 2012. Entropy production and optimization of geothermal power plants. J. Non-Equilib. Thermodyn. https://doi.org/10.1515/jnetdy-2011-0024.

Mroczek, E., Graham, D., Siega, C., Bacon, L., 2017. Silica scaling in cooled silica saturated geothermal water: comparison between Wairakei and Ohaaki geothermal fields, New Zealand. Geothermics 69, 145–152. https://doi.org/10.1016/j.geothermics.2017.05.006.

Mundhenk, N., Huttenloch, P., Sanjuan, B., Kohl, T., Steger, H., Zorn, R., 2013. Corrosion and scaling as interrelated phenomena in an operating geothermal power plant. Corros. Sci. https://doi.org/10.1016/j.corsci.2013.01.003.

Reyes, A.G., Trompetter, W.J., Britten, K., Searle, J., 2003. Mineral deposits in the Rotokawa geothermal pipelines, New Zealand. J. Volcanol. Geotherm. Res. 119, 215–239. https://doi.org/10.1016/S0377-0273(02)00355-4.

Felder, Richard M., Rousseau, Ronald W., 2000. Elementary Principles of Chemical Processes, 3rd ed. john Wiley & Sons, Inc., USA.

Rodgers, K., Browne, P., Buddle, T., Cook, K., Greatrex, R., Hampton, W., Herdianita, N., Holland, G., Lynne, B., Martin, R., Newton, Z., Pastars, D., Sannazarro, K., Treece, C., 2004. Silica phases in sinters and residues from geothermal fields of New Zealand. Earth-Sci. Rev. 66, 1–61. https://doi.org/10.1016/j.earscirev.2003.10.001.

Sagara, M., Ueyama, M., Higashi-Mukojima, N., Omura, T., Tomio, Y., Amaya, H., 2018. Nickel-based alloy, UNS N06845, with superior localized corrosion resistance for sour environment. In: Proceedings of the Corrosion 2018. Presented at the NACE Conference & Expo 2018, Phoenix, Az, USA, p. 13.

Teysseyre, S., Was, G.S., 2006. Stress corrosion cracking of austenitic alloys in supercritical water. Corrosion 62, 1100–1116. https://doi.org/10.5006/1.3278244.

Thorhallsson, A.I., Csáki, I., Geambazu, L.E., Magnus, F., Karlsdottir, S.N., 2021. Effect of alloying ratios and Cu-addition on corrosion behaviour of CoCrFeNiMo high-entropy alloys in superheated steam containing CO2, H2S and HCl. Corros. Sci. 178, 109083 https://doi.org/10.1016/j.corsci.2020.109083.

Thorhallsson, A.I., Karlsdottir, S.N., 2021. Corrosion behaviour of titanium alloy and carbon steel in a high-temperature, single and mixed-phase, simulated geothermal environment containing H2S, CO2 and HCl. Corros. Mater. Degrad. 2, 190–209. https://doi.org/10.3390/cmd2020011.

Thorhallsson, A.I., Stefansson, A., Kovalov, D., Karlsdottir, S.N., 2020a. Corrosion testing of materials in simulated superheated geothermal environment. Corros. Sci. 168, 108584 https://doi.org/10.1016/j.corsci.2020.108584.

Thorhallsson, A.I., Stefansson, A., Kovalov, D., Karlsdottir, S.N., 2020b. Corrigendum to “Corrosion testing of materials in simulated superheated geothermal environment” [Corros. Sci. 168 (2020) 10]. Corros. Sci. 174, 108807 https://doi.org/10.1016/j.corsci.2020.108807.

Toba, K., Ueyama, M., Kawano, K., Sakai, J., 2012. Corrosion of carbon steel and alloys in concentrated ammonium chloride solutions. Corrosion 68, 1049–1056. https://doi.org/10.5006/0587.

van den Heuvel, D.B., Gunnlaugsson, E., Gunnarsson, I., Stawski, T.M., Peacock, C.L., Benning, L.G., 2018. Understanding amorphous silica scaling under well-constrained conditions inside geothermal pipelines. Geothermics 76, 231–241. https://doi.org/10.1016/j.geothermics.2018.07.006.

References

[1] M.R. Karlsdottir, J. Heinonen, H. Palsson, O.P. Palsson, Life cycle assessment of a geothermal combined heat and power plant based on high temperature utilization, GEOTHERMICS. 84 (2020). https://doi.org/10.1016/j.geothermics.2019.101727.

[2] M.R. Karlsdottir, J. Heinonen, H. Palsson, O.P. Palsson, High-Temperature Geothermal Utilization in the Context of European Energy Policy-Implications and Limitations, ENERGIES. 13 (2020). https://doi.org/10.3390/en13123187.

[3] R. Corsi, Scaling and corrosion in geothermal equipment: Problems and preventive measures, GEOTHERMICS. 15 (1986) 839–856.

[4] I. Gunnarsson, S. Arnorsson, Impact of silica scaling on the efficiency of heat extraction from high-temperature geothermal fluids, GEOTHERMICS. 34 (2005) 320–329. https://doi.org/10.1016/j.geothermics.2005.02.002.

[5] S. Arnórsson, Geothermal systems in Iceland: Structure and conceptual models—I. High-temperature areas, Geothermics. 24 (1995) 561–602. https://doi.org/10.1016/0375-6505(95)00025-9.

[6] G.O. Fridleifsson, W.A. Elders, A. Albertsson, The concept of the Iceland deep drilling project, GEOTHERMICS. 49 (2014) 2–8. https://doi.org/10.1016/j.geothermics.2013.03.004.

[7] G.O. Fridleifsson, W.A. Elders, R.A. Zierenberg, A.P.G. Fowler, T.B. Weisenberger, K.G. Mesfin, O. Sigurdsson, S. Nielsson, G. Einarsson, F. Oskarsson, E.A. Gudnason, H. Tulinius, K. Hokstad, G. Benoit, F. Nono, D. Loggia, F. Parat, S.B. Cichy, D. Escobedo, D. Mainprice, The Iceland Deep Drilling Project at Reykjanes: Drilling into the root zone of a black smoker analog, J. Volcanol. Geotherm. Res. 391 (2020). https://doi.org/10.1016/j.jvolgeores.2018.08.013.

[8] W.A. Elders, G.O. Fridleifsson, B. Palsson, Iceland Deep Drilling Project: The first well, IDDP-1, drilled into magma Preface, GEOTHERMICS. 49 (2014) 1. https://doi.org/10.1016/j.geothermics.2013.08.012.

[9] G.O. Fridleifsson, W.A. Elders, R.A. Zierenberg, A. Stefansson, A.P.G. Fowler, T.B. Weisenberger, B.S. Hardarson, K.G. Mesfin, The Iceland Deep Drilling Project 4.5km deep well, IDDP-2, in the seawater-recharged Reykjanes geothermal field in SW Iceland has successfully reached its supercritical target, Sci. Drill. 23 (2017) 1–12. https://doi.org/10.5194/sd-23-1-2017.

[10] S.N. Karlsdottir, K.R. Ragnarsdottir, I.O. Thorbjornsson, A. Einarsson, Corrosion testing in superheated geothermal steam in Iceland, Geothermics. 53 (2015) 281–290. https://doi.org/10.1016/j.geothermics.2014.06.007.

[11] W.A. Elders, G.O. Fridleifsson, A. Albertsson, Drilling into magma and the implications of the Iceland Deep Drilling Project (IDDP) for high-temperature geothermal systems worldwide, GEOTHERMICS. 49 (2014) 111–118. https://doi.org/10.1016/j.geothermics.2013.05.001.

[12] B. Palsson, S. Holmgeirsson, A. Gudmundsson, H.A. Boasson, K. Ingason, H. Sverrisson, S. Thorhallsson, Drilling of the well IDDP-1, GEOTHERMICS. 49 (2014) 23–30. https://doi.org/10.1016/j.geothermics.2013.08.010.

[13] T. Hauksson, S. Markusson, K. Einarsson, S.N. Karlsdóttir, Á. Einarsson, A. Möller, Þ. Sigmarsson, Pilot testing of handling the fluids from the IDDP-1 exploratory geothermal well, Krafla, N.E. Iceland, Geothermics. 49 (2014) 76–82. https://doi.org/10.1016/j.geothermics.2013.07.003.

[14] D. B. van den Heuvel, E. Gunnlagsson, L.G. Benning, Passivation of metal surfaces against corrosion by silica scaling, in: 41st Workshop Geotherm. Reserv. Eng., Stanford, California, 2016.

[15] T. Jónsson, Corrosion Testing in a Simulated High Temperature Geothermal Environment, M.Sc. Thesis, University of Iceland, 2015.

[16] S.N. Karlsdottir, I.O. Thorbjornsson, K.R. Ragnarsdottir, A. Einarsson, Corrosion Testing of Heat Exchanger Tubes in Steam from the IDDP-1 Exploratory Geothermal Well in Krafla, Iceland, in: Corros. 2014, NACE International, San Antonio, Texas, USA, 2014: p. Paper no. NACE-2014-4152.

[17] I.O. Thorbjornsson, B.C. Krogh, G.S. Kaldal, G. Rørvik, S.S. Jonsson, F. Oskarsson, O. Sigurdsson, H. Husby, A. Ragnarsson, I.-I. Geosurvey, Corrosion Testing in Direct Geothermal Steam of Cladded and Standalone Materials at 210°C and 450°C, in: World Geotherm. Congr. 2020+1, Reykjavik, Iceland, 2021.

[18] I.O. Thorbjornsson, G.S. Kaldal, B.C. Krogh, B. Palsson, S.H. Markusson, P. Sigurdsson, A. Einarsson, B.S. Gunnarsson, S.S. Jonsson, Materials investigation of the high temperature IDDP-1 wellhead, GEOTHERMICS. 87 (2020). https://doi.org/10.1016/j.geothermics.2020.101866.

[19] N. Yanagisawa, Y. Masuda, H. Asanuma, K. Osato, K. Sakura, Estimation of casing material corrosion rates for supercritical geothermal development, GEOTHERMICS. 96 (2021). https://doi.org/10.1016/j.geothermics.2021.102149.

[20] Y. Kurata, N. Sanada, H. Nanjo, J. Ikeuchi, Casing pipe materials for deep geothermal wells, Geotherm. Resour. Counc. Trans. 19 (1995) 105–109.

[21] J. Nogara, S.J. Zarrouk, Corrosion in geothermal environment Part 2: Metals and alloys, Renew. Sustain. Energy Rev. 82 (2018) 1347–1363. https://doi.org/10.1016/j.rser.2017.06.091.

[22] J. Nogara, S.J. Zarrouk, Corrosion in geothermal environment: Part 1: Fluids and their impact, Renew. Sustain. ENERGY Rev. 82 (2018) 1333–1346. https://doi.org/10.1016/j.rser.2017.06.098.

[23] T. Kaya, P. Hoshan, Corrosion and Material Selection for Geothermal Systems, in: World Geotherm. Congr. 2005, Antalya, Turkey, 2005.

[24] R. Rihan, B. Al-Wakaa, N. Tanoli, H. Shalaby, The susceptibility of P110 downhole tubular steel to sulfide stress cracking in H2S and NaCl, J. Pet. Sci. Eng. 174 (2019) 1034–1041. https://doi.org/10.1016/j.petrol.2018.10.102.

[25] M. Monnot, R.P. Nogueira, V. Roche, G. Berthomé, E. Chauveau, R. Estevez, M. Mantel, Sulfide stress corrosion study of a super martensitic stainless steel in H2S sour environments: Metallic sulfides formation and hydrogen embrittlement, Appl. Surf. Sci. 394 (2017) 132–141. https://doi.org/10.1016/j.apsusc.2016.10.072.

[26] D. Jingen, Y. Wei, L. Xiaorong, D. Xiaoqin, Influence of H2S Content on CO2 Corrosion Behaviors of N80 Tubing Steel, Pet. Sci. Technol. 29 (2011) 1387–1396. https://doi.org/10.1080/10916466.2010.545784.

[27] J. Banaś, U. Lelek-Borkowska, B. Mazurkiewicz, W. Solarski, Effect of CO2 and H2S on the composition and stability of passive film on iron alloys in geothermal water, Electrochimica Acta. 52 (2007) 5704–5714. https://doi.org/10.1016/j.electacta.2007.01.086.

[28] Y. Gui, Z. Liang, Q. Zhao, Corrosion and Carburization Behavior of Heat-Resistant Steels in a High-Temperature Supercritical Carbon Dioxide Environment, Oxid. Met. 92 (2019) 123–136. https://doi.org/10.1007/s11085-019-09917-x.

[29] L. Krumm, M.C. Galetz, Chlorine Attack of Carbon Steel Between 350 and 500 degrees C and Its Importance Regarding Corrosion in Waste Incineration, Oxid. Met. 87 (2017) 757–766. https://doi.org/10.1007/s11085-017-9749-x.

[30] ASTM G1-03(2017)e1 Standard Practice for Preparing, Cleaning, and Evaluating Corrosion Test Specimens, ASTM International, 2017. http://www.astm.org/cgi-bin/resolver.cgi?G1-90(1999)e1.

[31] D.A. Jones, Effects of Metallurgical Structure on Corrosion - 10.1 Hydrogen Damage, in: Princ. Prev. Corros., 2nd ed., Prentice Hall, United States of America, 1996: pp. 334–343.

[32] E. Ramirez, J.G. Gonzalez-Rodriguez, A. Torres-Islas, S. Serna, B. Campillo, G. Dominguez-Patino, J.A. Juarez-Islas, Effect of microstructure on the sulphide stress cracking susceptibility of a high strength pipeline steel, Corros. Sci. 50 (2008) 3534–3541. https://doi.org/10.1016/j.corsci.2008.09.014.

[33] D.A. Jones, Corrosive-Related Damage by Hydrogen, Erosion, and Wear, in: Princ. Prev. Corros., 2nd ed., Prentice Hall, United States of America, 1996: pp. 334–341.

[34] NACE International, NACE MR0175/ISO 15156, NACE, Houston, Tex., 2009.

[35] M. Iannuzzi, 15 - Environmentally assisted cracking (EAC) in oil and gas production, in: V.S. Raja, T. Shoji (Eds.), Stress Corros. Crack., Woodhead Publishing, 2011: pp. 570–607. https://doi.org/10.1533/9780857093769.4.570.

[36] J. Davidson, Hydrogen-induced cracking of low carbon - Low alloy steel weldments, Mater. FORUM. 19 (1995) 35–51.

[37] K.-S. Kim, J.-H. Kang, S.-J. Kim, Effect of Grain Boundary Carbide on Hydrogen Embrittlement in Stable Austenitic Stainless Steels, ISIJ Int. 59 (2019) 1136–1144. https://doi.org/10.2355/isijinternational.ISIJINT-2018-639.

[38] K.-S. Kim, J.-H. Kang, S.-J. Kim, Nitrogen effect on hydrogen diffusivity and hydrogen embrittlement behavior in austenitic stainless steels, Scr. Mater. 184 (2020) 70–73. https://doi.org/10.1016/j.scriptamat.2020.03.038.

[39] M.L. Martin, M. Dadfarnia, S. Orwig, D. Moore, P. Sofronis, A microstructure-based mechanism of cracking in high temperature hydrogen attack, Acta Mater. 140 (2017) 300–304. https://doi.org/10.1016/j.actamat.2017.08.051.

[40] P. Rhodes, Environment-assisted cracking of corrosion-resistant alloys in oil and gas production environments: A review, CORROSION. 57 (2001) 923–966. https://doi.org/10.5006/1.3290320.

[41] A. Traidia, E. Chatzidouros, M. Jouiad, Review of hydrogen-assisted cracking models for application to service lifetime prediction and challenges in the oil and gas industry, Corros. Rev. 36 (2018) 323–347. https://doi.org/10.1515/corrrev-2017-0079.

[42] M.H. Bartz, C.E. Rawlins, Effects of Hydrogen Generated by Corrosion of Steel, in: Annu. Meet. NACE, NACE International, St. Lois, 1948.

[43] S. Gao, B. Brown, D. Young, M. Singer, Formation of iron oxide and iron sulfide at high temperature and their effects on corrosion, Corros. Sci. 135 (2018) 167–176. https://doi.org/10.1016/j.corsci.2018.02.045.

[44] F. Pessu, R. Barker, F. Chang, T. Chen, A. Neville, Iron sulphide formation and interaction with corrosion inhibitor in H2S-containing environments, J. Pet. Sci. Eng. 207 (2021). https://doi.org/10.1016/j.petrol.2021.109152.

[45] S. Soylemezoglu, R. Harper, Oxygen ingress into geothermal steam and its effect on corrosion of low carbon steel at Broadlands, New Zealand, Geothermics. 11 (1982) 31–42. https://doi.org/10.1016/0375-6505(82)90005-0.

[46] E. Dayalan, G. Vani, J.R. Shadley, S.A. Shirazi, E.F. Rybicki, Modelling CO2 Corrosion of Carbon Steel in Pipe Flow, in: NACE Int. Annu. Conf. Corros. Show, NACE International, Orlando, FL, USA, 1995: p. Paper #118.

[47] A. Ikeda, M. Ueda, S. Mukai, Incluence of Environmental Factors on Corrosion in CO2 Source Well, in: Corros. Symp. Corros. CO2 Oil Gas Ind., NACE International, New Orleans, LA, USA, 1984.

[48] M.A. Islam, Z.N. Farhat, Characterization of the Corrosion Layer on Pipeline Steel in Sweet Environment, J. Mater. Eng. Perform. 24 (2015) 3142–3158. https://doi.org/10.1007/s11665-015-1564-4.

[49] L.G. Gray, B.G. Anderson, M.J. Danysh, P.R. Tremaine, Mechanisms of carbon steel corrosion in brines containing dissolved carbon dioxide at pH 4, Corros. Pap. (1989) 1–18.

[50] S. Nesic, Key issues related to modelling of internal corrosion of oil and gas pipelines - A review, Corros. Sci. 49 (2007) 4308–4338. https://doi.org/10.1016/j.corsci.2007.06.006.

[51] D.A. Jones, Environmentally Induced Cracking, in: Princ. Prev. Corros., 2nd ed., Prentice Hall, United States of America, 1996: pp. 236–244.

[52] S. Wu, H. Chen, H.L. Ramandi, P.C. Hagan, A. Crosky, S. Saydam, Effects of environmental factors on stress corrosion cracking of cold-drawn high-carbon steel wires, Corros. Sci. 132 (2018) 234–243. https://doi.org/10.1016/j.corsci.2017.12.014.

[53] W. Qi, Q. Gao, Y. Zhao, T. Zhang, F. Wang, Insight into the stress corrosion cracking of HP-13Cr stainless steel in the aggressive geothermal environment, Corros. Sci. 190 (2021). https://doi.org/10.1016/j.corsci.2021.109699.

[54] L. Wu, Y. Takeda, H. Morita, T. Shoji, A Comparison of Stress Corrosion Cracking Susceptibility of Steam Turbine Blade Materials for Geothermal Plants, CORROSION. 73 (2017) 125–137. https://doi.org/10.5006/2058.

[55] S.N. Karlsdottir, S.M. Hjaltason, K.R. Ragnarsdottir, Corrosion behavior of materials in hydrogen sulfide abatement system at Hellisheioi geothermal power plant, GEOTHERMICS. 70 (2017) 222–229. https://doi.org/10.1016/j.geothermics.2017.06.010.

[56] R. Bassler, A. Keserovi, J. Sobetzki, H.S. Klapper, MATERIALS EVALUATION FOR GEOTHERMAL APPLICATIONS, J. Teknol. 75 (2015) 7–14.

[57] M. Cabrini, S. Lorenzi, T. Pastore, M. Favilla, R. Perini, B. Tarquini, Materials selection for dew-point corrosion in geothermal fluids containing acid chloride, GEOTHERMICS. 69 (2017) 139–144. https://doi.org/10.1016/j.geothermics.2017.05.010.

[58] W. Faes, S. Lecompte, J. Van Bael, R. Salenbien, R. Baessler, I. Bellemans, P. Cools, N. De Geyter, R. Morent, K. Verbeken, M. De Paepe, Corrosion behaviour of different steel types in artificial geothermal fluids, GEOTHERMICS. 82 (2019) 182–189. https://doi.org/10.1016/j.geothermics.2019.05.018.

[59] U. Ince, M. Toksoy, M. Guden, Testing corrosion rates on steel piping in geothermal district heating, Mater. Perform. 47 (2008) 56–59.

[60] W. Zhang, B. Brown, D. Young, G. Bota, S. Nesic, M. Singer, Pitting mechanism of mild steel in marginally sour environments—Part I: A parametric study based on formation of protective layers, Corros. Sci. 183 (2021) 109305. https://doi.org/10.1016/j.corsci.2021.109305.

[61] W. Zhang, B. Brown, D. Young, M. Singer, Pitting mechanism of mild steel in marginally sour environments – Part II: Pit initiation based on the oxidation of the chemisorbed iron sulfide layers, Corros. Sci. 184 (2021) 109337. https://doi.org/10.1016/j.corsci.2021.109337.

[62] D.A. Jones, Effects of Metallurgical Structure on Corrosion - 9.5 De-alloying, in: Princ. Prev. Corros., 2nd ed., Prentice Hall, United States of America, 1996: pp. 323–331.

[63] D.A. Jones, Effects of Metallurgical Structure on Corrosion - 9.1 Intergranular Corrosion of Austenitic Steels, in: Princ. Prev. Corros., 2nd ed., Prentice Hall, United States of America, 1996: pp. 292–304.

[64] E. Heitz, Mechanistically based prevention strategies of flow-induced corrosion, ELECTROCHIMICA ACTA. 41 (1996) 503–509. https://doi.org/10.1016/0013-4686(95)00336-3.

[65] D.A. Jones, Corrosion-Related Damage by Hydrogen, Erosion and Wear - 10.2 Erosion-Corrosion, in: Princ. Prev. Corros., 2nd ed., Prentice Hall, United States of America, 1996: pp. 343–347.

[66] S.N. Karlsdottir, K.R. Ragnarsdottir, A. Moller, I.O. Thorbjornsson, A. Einarsson, On-site erosion-corrosion testing in superheated geothermal steam, GEOTHERMICS. 51 (2014) 170–181. https://doi.org/10.1016/j.geothermics.2014.01.007.

[67] F. Brownlie, T. Hodgkiess, A. Pearson, A.M. Galloway, A study on the erosion-corrosion behaviour of engineering materials used in the geothermal industry, WEAR. 477 (2021). https://doi.org/10.1016/j.wear.2021.203821.

[68] D.A. Jones, Galvanic and Concentrated Cell Corrosion, in: Princ. Prev. Corros., 2nd ed., Prentice Hall, United States of America, 1996: pp. 168–199.

[69] S.N. Esmaeely, G. Bota, B. Brown, S. Nesic, Influence of Pyrrhotite on the Corrosion of Mild Steel, CORROSION. 74 (2018) 37–49. https://doi.org/10.5006/2505.

[70] S.N. Esmaeely, S. Nesic, Reduction Reactions on Iron Sulfides in Aqueous Acidic Solutions, J. Electrochem. Soc. 164 (2017) C664–C670. https://doi.org/10.1149/2.1381712jes.

[71] S.N. Esmaeely, S. Nesic, Localized Corrosion of Mild Steel in H2S Containing Aqueous Environments-Case Studies and Common Mechanisms, CORROSION. 75 (2019) 938–945. https://doi.org/10.5006/3164.

[72] H.H. Strehblow, P. Marcus, Fundamentals of Corrosion, in: Corros. Mech. Theory Pract., 3rd ed., CRC Press, 2017: pp. 3–12.

[73] Y. Kawahara, High temperature corrosion mechanisms and effect of alloying elements for materials used in waste incineration environment, Corros. Sci. 44 (2002) 223–245. https://doi.org/10.1016/S0010-938X(01)00058-0.

[74] M. Schütze, High-Temperature Corrosion, in: Corros. Mech. Theory Pract., 3rd ed., CRC Press, 2012: p. 573.

[75] M. Schütze, High-Temperature Corrosion, in: Corros. Mech. Theory Pract., 3rd ed., CRC Press, 2017: pp. 573–584.

[76] E. Barbier, Geothermal energy technology and current status: an overview, Renew. Sustain. ENERGY Rev. 6 (2002) 3–65. https://doi.org/10.1016/S1364-0321(02)00002-3.

[77] K.A. Licthi, S. Soylemezoglu, K.D. Cuncliffe, Geotherrmal corrosion and corrosion products., in: 1981: pp. 103–108.

[78] C. Miranda-Herrera, I. Sauceda, J. Gonzalez-Sanchez, N. Acuna, Corrosion degradation of pipeline carbon steels subjected to geothermal plant conditions, ANTI-Corros. METHODS Mater. 57 (2010) 167–172. https://doi.org/10.1108/00035591011058165.

[79] M. Finster, C. Clark, J. Schroeder, L. Martino, Geothermal produced fluids: Characteristics, treatment technologies, and management options, Renew. Sustain. ENERGY Rev. 50 (2015) 952–966. https://doi.org/10.1016/j.rser.2015.05.059.

[80] J.A. Acuna, B. Arcedera, Two-Phase Flow Behavior and Spinner Data Analysis in Geothermal Wells, in: Thirtieth Workshop Geotherm. Reserv. Eng., Stanford, California, 2005.

[81] M. Kruszewski, V. Wittig, Review of failure modes in supercritical geothermal drilling projects, Geotherm. ENERGY. 6 (2018). https://doi.org/10.1186/s40517-018-0113-4.

[82] A. Hansell, C. Oppenheimer, Health hazards from volcanic gases: A systematic literature review, Arch. Environ. Health. 59 (2004) 628–639. https://doi.org/10.1080/00039890409602947.

[83] S. Arnorsson, J.Ö. Bjarnason, N. Giroud, A. Stefansson, Sampling and analysis of geothermal fluids, in: Geofluids, Wiley, 2006: pp. 203–216. https://onlinelibrary.wiley.com/doi/full/10.1111/j.1468-8123.2006.00147.x.

[84] S. Arnorsson, Isotopic and chemical techniques in geothermal exploration, development and use: sampling methods, data handling, interpretation, Int. At. Energy Agency. (2000) 108–113.

[85] Procedures for the Measurement of Carryover of Boiler Water into Steam, (2008). http://www.iapws.org/techguide/Carryover.pdf (accessed November 28, 2021).

[86] G. Petzow, Metallographic Etching, in: Metallogr. Etch., American Society for Metals, Ohio, USA, 1978: p. 87.

[87] G. Petzow, Metallographic Etching, in: Metallogr. Etch., American Society for Metals, Ohio, USA, 1978: p. 64.

[88] G.F. Vander Voort, J.W. Bowman, R.B. Frank, Microstructural characterization of custom age 625 plus alloy, in: Miner. Met. Mater. Soc., 1994: pp. 489–498. https://www.researchgate.net/publication/269258305_Microstructural_Characterization_of_Custom_Age_625_Plus_Alloy.

[89] H. Jia, H. Qian, W. Qu, L. Zheng, W. Feng, W. Ren, Fluoride Occurrence and Human Health Risk in Drinking Water Wells from Southern Edge of Chinese Loess Plateau, Int. J. Environ. Res. Public. Health. 16 (2019). https://doi.org/10.3390/ijerph16101683.

[90] M. Meldrum, Toxicology of hydrogen fluoride in relation to major accident hazards, Regul. Toxicol. Pharmacol. 30 (1999) 110–116. https://doi.org/10.1006/rtph.1999.1342.

[91] REVIEW OF LOW-TEMPERATURE OXIDATION OF CARBON STEELS AND LOW-ALLOY STEELS FOR USE AS HIGH-LEVEL RADIOACTIVE WASTE PACKAGE MATERIALS, (2007). https://www.nrc.gov/docs/ML0402/ML040200112.pdf (accessed November 28, 2021).

Conference papers

Andri I. Thorhallsson, S.N. Karlsdottir, A. Stefansson, Corrosion Testing of UNS N06625 in a Simulated High Temperature Geothermal Environment, PROCEEDINGS in CORROSION 2018 Conference and Expo, April 15-19, Phoenix, Arizona, USA, paper no. 11058

Andri I. Thorhallsson, S.N. Karlsdottir, A. Stefansson, Corrosion Testing of UNS S31603 in Simulated HT Geothermal Environment at Boiling, Superheated and Condensation Conditions, PROCEEDINGS in CORROSION 2019 Conference and Expo, March 24-28, 2019, Nashville, Tennessee, USA, paper no. 13195.

Andri Isak Thorhallsson, Ioana Csaki, Sigrun Nanna Karlsdottir, Laura Elena Geambazu, $Co_{20}Cr_{20}Fe_{20}Ni_{20}Mo_{20}$ high entropy alloys behavior in superheated geothermal steam, PROCEEDINGS IN WGC 2020+1, 2021.

Andri I. Thorhallsson, Sigrun Nanna Karlsdottir, William MacDonald, James S. Grauman, Titanium Alloy Casing for High-Temperature Geothermal, PROCEEDINGS IN WGC 2020+1, 2021.